ALMA Mater Studiorum
Università degli studi di Bologna

SCUOLA DI SCIENZE
Corso di Laurea Magistrale in Astrofisica e Cosmologia
Dipartimento di Fisica e Astronomia

High-energy view of radio galaxies: prospects for the new generation of Cherenkov telescopes

Elaborato Finale

Candidato:
Roberto Angioni

Relatore:
Prof. Cristian Vignali

Co-Relatrici:
Dott.ssa Paola Grandi
Dott.ssa Eleonora Torresi

Sessione I
Anno Accademico 2014/2015

This thesis work was carried out in collaboration with the high-energy astrophysics group of the INAF-IASF institute in Bologna.

Contents

Sommario

I *Nuclei Galattici Attivi* (AGN, *Active Galactic Nuclei*) sono fra le sorgenti di radiazione più potenti nell'universo, e la loro emissione spazia su tutto lo spettro elettromagnetico, dalla banda radio alla banda TeV. Il modello più accreditato per spiegare questa emissione, affermatosi negli ultimi decenni, ipotizza che questa sia prodotta dall'accrescimento di materia su un buco nero supermassiccio al centro della galassia che ospita l'AGN.

Una frazione degli AGN (10-20%) presenta una forte emissione in banda radio, e viene quindi denominata *radio-loud* (RL). Questa emissione è dovuta principalmente alla presenza di getti di particelle relativistiche prodotti nelle regioni centrali dell'AGN. Il meccanismo attraverso cui questi getti vengono prodotti, e quindi le condizioni e i parametri fisici per i quali un AGN diventa *radio-loud*, costituiscono uno degli argomenti più studiati e dibattuti nell'astronomia extragalattica, e sono fra le problematiche scientifiche principali trattate nel contesto di ricerca in cui è stato svolto questo lavoro di tesi.

In molti AGN radio-loud il getto stesso si muove con velocità relativistica. Per questo motivo, se l'asse del getto è orientato in modo da allinearsi con la linea di vista dell'osservatore la sua radiazione viene fortemente amplificata da effetti relativistici (*Doppler boosting*), tanto da "sommergere" le altre componenti che contribuiscono alla radiazione totale emessa dalla sorgente. In questo caso la sorgente viene detta *blazar*. Grazie a questo effetto, i blazar costituiscono la grande maggioranza di tutte le sorgenti extragalattiche osservate in banda γ.

Secondo il modello unificato degli AGN, le radio galassie e gli *Steep Spectrum Radio Quasars* (SSRQ) costituiscono la cosiddetta *parent population* dei blazar, ossia la loro controparte con un getto non allineato. Per questo ci si riferisce collettivamente a queste sorgenti, in particolare in banda γ, come *Misaligned AGN* (MAGN). Dato che il getto non è allineato con la nostra linea di vista l'emissione è meno soggetta a Doppler boosting, per cui, soprattutto in banda γ, è più debole rispetto a quella dei blazar. Per questo motivo, la frazione di MAGN nei cataloghi in banda γ è molto bassa (1-2%).

Questo lavoro di tesi si è incentrato sull'analisi delle quattro fra le sorgenti osservate da *Fermi*-LAT (banda 0.1-100 GeV) che sono state osservate anche alle

altissime energie (*Very High Energies* o VHE, $E > 100$ GeV) grazie ai telescopi Cherenkov: NGC 1275, Centaurus A, M87 e IC 310. Questo campione è da confrontarsi, per esempio, con i 58 blazar osservati in banda TeV. La grande differenza fra questi numeri è attribuita alla differenza di orientamento del getto.

Lo studio dei MAGN in banda TeV è di particolare interesse, in quanto l'eccellente risoluzione temporale disponibile in questa banda permette di rivelare variabilità di flusso molto rapida, anche dell'ordine dei minuti. Per rispettare il principio di causalità all'interno della regione di emissione, questa variabilità permette di porre un limite superiore alle dimensioni di questa regione, arrivando a scale inaccessibili in tutte le altre bande energetiche. Per via della ridotta risoluzione spaziale dei telescopi Cherenkov, non è possibile determinare la posizione della regione di emissione all'interno della sorgente attraverso *imaging* diretto. Questa può tuttavia essere stimata correlando la variabilità osservata con quella in bande energetiche in cui si dispone di migliore risoluzione, come per esempio la banda radio.

Un'altra motivazione per lo studio dell'emissione γ dei MAGN è quella di confrontarla con quella dei blazar, alla luce del modello unificato per gli AGN radio-loud, nonché per testare i modelli teorici dei processi fisici responsabili per l'accelerazione delle particelle nei getti fino alle altissime energie. Inoltre, questi studi ci permettono di avere una visione dei getti negli AGN radio-loud che non soffra del *bias* dovuto al Doppler boosting.

Uno dei punti di maggior interesse per i MAGN, infine, è dato dal fatto che avendo dei getti non allineati con la nostra linea di vista, queste sorgenti ci permettono di osservare sia il getto sia i processi di accrescimento, e quindi di cercare una connessione fra i due, studiando in questo modo l'origine del comportamento radio-loud negli AGN.

Lo scopo principale di questo lavoro di tesi è di valutare l'impatto del *Cherenkov Telescope Array* (CTA), lo strumento di nuova generazione per le altissime energie, nello studio dei MAGN in banda TeV, partendo dai dati attuali in banda γ. A questo fine, in una prima fase abbiamo analizzato in dettaglio l'emissione ad alta energia delle quattro sorgenti osservate, ad oggi, alle altissime energie.

Tramite l'analisi di sei anni di dati dallo strumento *Fermi*-LAT, abbiamo studiato la loro forma spettrale e variabilità. Gli spettri ottenuti sono in accordo con quelli pubblicati in letteratura, con un rapporto segnale/rumore migliorato grazie al maggiore tempo di integrazione. Gli spettri sono ben rappresentati da una forma a legge di potenza, tranne che per NGC 1275, per cui la rappresentazione migliore risulta essere una Logparabola.

Abbiamo rilevato una variabilità significativa per NGC 1275 su tempi scala pari a una settimana. Tramite considerazioni sulla causalità, questo implica che la regione di emissione deve essere $R < 0.012$ pc. Assumendo che questa scala

indichi la distanza dal buco nero supermassiccio, la regione di emissione risulta compresa nella scala che in oggetti *radio-quiet* corrisponde alla Broad Line Region (BLR).

Ripetendo l'analisi su tempi scala di tre settimane abbiamo rilevato una significativa variabilità spettrale, che mostra una anti-correlazione fra indice spettrale e flusso. Questo comportamento è comune nei blazar. Solitamente viene attribuito all'iniziezione di nuove particelle energetiche nel getto durante uno stato alto, che comporta un appiattimento della distribuzione di energia degli elettroni e quindi anche dello spettro osservato.

Non si è osservata variabilità statisticamente significativa per Cen A, M87 e IC 310. Poiché queste ultime due sorgenti sono variabili in banda TeV, non è chiaro se l'assenza di variabilità nei dati *Fermi* sia un fatto fisico oppure sia dovuta alla bassa statistica dei dati, che non permette un campionamento abbastanza fitto.

Successivamente, abbiamo raccolto dati in banda TeV dalla letteratura, e costruito uno spettro dal MeV al TeV per queste stesse sorgenti. La connessione fra alte energie e altissime energie è complessa, in quanto generalmente i dati non sono contemporanei, il che è rilevante dato il loro comportamento variabile. Inoltre, è possibile che i processi di emissione che producono la radiazione osservata nelle due bande siano diversi, o che ci siano più regioni di emissione con spettri differenti, come è stato osservato nel caso di Centaurus A. La sorgente per cui abbiamo lo spettro MeV-TeV più affidabile è NGC 1275, poiché vi sono dati contemporanei da *Fermi* e dal telescopio Cherenkov *MAGIC*. Lo spettro totale è ben rappresentato da una legge di potenza con indice spettrale $\Gamma = 2.05^{+0.08}_{-0.08}$ e un *cutoff* esponenziale a $E_{cut} = 110^{+70}_{-40}$ GeV.

Per identificare i migliori candidati MAGN per osservazioni TeV con il CTA, abbiamo preso in considerazione i MAGN inclusi nel più recente catalogo di AGN osservati da *Fermi*, il 3LAC. Questi 23 oggetti, con l'aggiunta di 3C 120 (una nota radio galassia con emissione γ), costituiscono il nostro campione di candidati.

Per stimarne la possibilità di osservazione, abbiamo stimato il flusso integrato che sarebbe misurato dal CTA per i nostri MAGN candidati, tramite il pacchetto software *ctools*. Abbiamo simulato 50 ore di osservazione con il CTA per le nostre sorgenti, usando come modello un'estrapolazione dei loro parametri spettrali nella banda di *Fermi*. Abbiamo quindi analizzato il file di dati risultante con una tecnica standard di massimizzazione della *likelihood*, e calcolato il flusso integrato nella banda energetica del CTA usando i parametri spettrali risultanti, coi relativi errori. Questa analisi prevede l'osservazione con il CTA di tutte le sorgenti di tipo FR I locali ($z < 0.1$), inclusi 9 nuovi MAGN con $TS > 25$ (Test Statistic), corrispondente a $\sigma > 5$. I nostri risultati indicano chiaramente che i parametri fondamentali che identificano un buon candidato per l'osservazione in banda TeV sono uno spettro piatto ($\Gamma < 2.2$) e basso redshift.

Poiché l'assunzione che lo spettro osservato dal LAT possa essere estrapolato fino a 100 TeV è molto ottimistica, abbiamo ipotizzato uno scenario più realistico assumendo un cutoff nello spettro a 100 GeV, simile a quello osservato nel caso di NGC 1275. Ripetendo l'analisi sotto questa ipotesi, abbiamo una sorgente osservata con TS>25 (PKS 0625-35) e due candidati al limite della significatività, con TS∼11 (Centaurus B) e TS∼9 (NGC 6251). Inoltre, va considerato che se queste sorgenti fossero variabili alle altissime energie, come è stato osservato per M87 e IC 310, altre potrebbero essere osservate in uno stato alto, come per esempio 3C 78.

Come test aggiuntivo, abbiamo cercato di determinare il miglioramento nella qualità dei dati forniti dal CTA per i quattro MAGN già osservati in banda TeV, ripetendo la stessa analisi descritta precedentemente per questi oggetti. I risultati indicano che il miglioramento nella qualità dei dati sarà molto significativo, con un TS migliore di un fattore da ∼10 a ∼200.

Infine, abbiamo studiato le potenzialità del CTA nello studio spettrale di MAGN, estrapolando lo spettro LAT ad altissime energie applicando un *cutoff* a diverse energie, e confrontando lo spettro risultante con le curve di sensibilità differenziale del CTA per diversi tempi osservativi. A differenza dell'analisi precedente, in questo caso lo scopo era capire per quali sorgenti sarà possibile ottenere uno spettro con il CTA, oltre a rilevarle integrando su tutta la banda energetica. La nostra analisi mostra che, sotto queste assunzioni, con 250 ore di integrazione sarà possibile ottenere uno spettro di buona qualità per PKS 0625-35 anche se il suo spettro ha un *cutoff* a 100 GeV, e di altre quattro sorgenti locali a spettro piatto, se la loro legge di potenza si estende fino a ∼ 500 GeV.

Abbiamo confrontato i nostri risultati con le prospettive attuali per una *survey* extragalattica con il CTA, che prevedono una *survey blind-sky*, ossia non puntata, di circa un quarto del cielo. Il tempo osservativo per campo di vista stimato è significativamente minore di quelli considerati nel nostro studio, per cui questa strategia non sarebbe la più adatta per rilevare nuovi MAGN in banda TeV. La migliore strategia osservativa per rivelare queste sorgenti, spesso deboli, consisterebbe in osservazioni puntate dei candidati più promettenti (e.g. PKS 0625-35, Cen B, NGC 6251, 3C 78) con lunghi tempi di integrazione.

Questo lavoro è stato il primo studio sistematico dei MAGN come classe di sorgenti nella banda TeV, e del loro potenziale scientifico con il CTA. Grazie a questi risultati, abbiamo ora una comprensione migliore delle potenzialità degli studi di MAGN con il CTA, e di quale sarebbe la strategia osservativa migliore per osservarli.

Abstract

Active Galactic Nuclei (AGN) are among the most powerful sources of radiation in the universe. In the last decades a general consensus has been reached over a unification scenario which attempts to explain the variety of observed AGN classes under a single paradigm where the observed radiation is produced by accretion onto a supermassive black hole (SMBH) at the center of the AGN-hosting galaxy.

A fraction (10-20%) of AGN emit very strongly at radio wavelengths, and are thus called radio loud (RL) AGN. Their powerful radio emission is associated with the presence of highly collimated jets of relativistic particles. The triggering and launching mechanism of these jets, and therefore the physical parameters and conditions under which an AGN becomes radio loud, constitute one of the most debated and studied topics in this field, and one of the main scientific goals of the research context in which this thesis work is taking place.

The relativistic particles in the jets produce both synchrotron radiation (at wavelengths from radio to optical-UV) by interacting with a magnetic field, and high-energy radiation (from hard X-rays up to TeV γ-rays). The high-energy emission mechanism is not well understood. The simplest and most successful model adopted to explain it involves Inverse Compton (IC) upscattering of low-energy photons by the relativistic particles in the jet. Other models have also been proposed, e.g. the hadronic models, which consider the contribution to high-energy radiation from protons and secondary particles resulting from their interactions (with themselves or with photons).

Since the jet moves with bulk relativistic speed, if its axis is oriented at small angles with respect to the observer's line of sight this radiation is strongly Doppler-boosted, such as to swamp all the other contributions to the source's broad-band emission. In this case the source is called a *blazar*, and its Spectral Energy Distribution (SED) has indeed a double-peaked shape (synchrotron peak and IC peak). Thanks to the strong Doppler boosting, blazars constitute the vast majority of all observed sources in the γ-ray band.

According to the unified scenario of AGN, radio galaxies and Steep Spectrum Radio Quasars (SSRQs) constitute the misaligned parent population of blazars, and are collectively called Misaligned AGN (MAGN). Since their jet is not aligned

with the observer's line of sight, their radiation is less Doppler-boosted. Nevertheless they have been established as a class of high-energy emitters, and mainly thanks to the *Fermi*-LAT instrument today the catalog of γ-ray MAGN counts 24 sources. Most of these sources are local ($z < 0.1$) faint radio galaxies .

Four of these sources (NGC 1275, Centaurus A, M87, and IC 310) have also been detected in the very high-energy (VHE, E>100 GeV) range by current *Imaging Atmospheric Cherenkov Telescopes*. This small number is to be compared with the 58 VHE detected blazars. This disproportion is again attributed to the differences in orientation. It is expected that the new generation *Cherenkov Telescope Array* (CTA), currently in a design phase, will be able to detect many more AGN in the 10 GeV-100 TeV energy range, and to provide better quality data for those already detected. This will be achieved thanks to its order-of-magnitude improved flux sensitivity, its wide energy range, and its sub-minute temporal resolution.

TeV observations of MAGN are of particular interest, because the excellent temporal resolution available in this band allows us to detect fast variability, down to the order of minutes. Through causality arguments, this variability implies an upper limit on the size of the emission region, probing scales inaccessible in any other energy band. The location of the emission region cannot be determined by direct imaging due to the poor spatial resolution of the IACT instruments, but it can be estimated by correlating the observed variability with that in energy bands which benefit from better resolution, e.g. radio wavelengths. Another reason to study γ-ray emission from MAGN is to compare their high-energy properties with the ones of blazars in the framework of the radio-loud unified schemes, and to constrain the theoretical models which try to reproduce the physical processes capable of accelerating particles up to such high energies. Moreover, these studies provide us with a high-energy view of AGN jets which is not biased by Doppler boosting. Lastly, since these sources are misaligned, we are able to observe both the jet and the accretion process, and so attempt to establish a connection between the two, therefore investigating the origin of AGN radio loudness.

The main goal of this thesis work is to evaluate the impact of the CTA on TeV studies of radio galaxies, based on available γ-ray data. To achieve this, we first performed a detailed high-energy analysis of the four sources already detected at VHE. Using six years of *Fermi*-LAT data, we investigated their spectral shape and time variability. Our spectra are consistent with those reported in the literature, although they show significantly better signat-to-noise ratio due to the longer integration time with respect to e.g. the 3LAC catalog. Moreover, we have performed a dedicated analysis for each source, rather than an automatic catalog analysis.

Additionally, we detected statistically significant variability on weekly time

scales for NGC 1275, which allowed us to put an upper limit on the size of the γ-ray emission region, through causality arguments. We found that the dissipation region for the high-energy photons is constrained to be inside the BLR. We also found significant spectral variability for the same source, on time scales of 3 weeks, with a significant anti-correlation between flux and spectral index. This behavior is common among blazars, and is explained as due to the injection of fresh energetic particles in the jet during a flare, which causes a hardening of the particle energy distribution and, therefore, a flatter observed spectrum.

Then, in order to constrain the overall shape of the high-energy peak of the SED, we have collected VHE data from literature to investigate whether the TeV spectrum connects smoothly with the LAT data or not. The spectral shapes observed are varied. Additionally, it must be noted that GeV and TeV data are usually not simultaneous, which is relevant since these sources are variable. The most reliable MeV-TeV spectrum is the one of NGC 1275, which is best fitted with a power-law with an exponential cutoff.

We assumed as MAGN TeV candidates those included in the latest *Fermi*-LAT AGN catalog (3LAC), obtaining a sample of 24 sources. We produced simulated CTA observations for these objects using the software package *ctools*. First we assumed a simple extrapolation of the LAT spectrum into the TeV band, and calculated the resulting integrated flux and signal-to-noise ratio to determine which sources would be detected. In this case, we predict 9 new MAGN detections with $TS > 25$. Then, to test a more realistic scenario, we have assumed a steep exponential cutoff at 100 GeV, resembling our most reliable HE-VHE spectrum, i.e. the one of NGC 1275. In this case we predict one robust detection, and two borderline but still significant detections. In any case, the most promising TeV MAGN candidates are local ($z < 0.1$) flat spectrum ($\Gamma < 2.2$) sources.

We have also investigated to which extent the CTA will provide better data for the four TeV detected radio galaxies. Using the same methods described above, but assuming their observed VHE spectral properties instead of the *Fermi* ones, we have compared the resulting CTA signal-to-noise ratio with the current one. We found that the TS of the CTA data is a factor ranging from ~ 11 to ~ 240 times better than the one provided by current TeV data. Moreover, we have simulated a CTA spectrum for one of the sources, NGC 1275, in order to test the performance of the CTA for spectral analysis. Again, the SNR of the spectrum is greatly improved with respect to current data.

Finally, we have attempted to predict whether the CTA will allow us to obtain TeV spectra of our candidate TeV MAGN, by extrapolating their LAT spectra into the CTA energy range using different spectral shapes, and comparing the resulting spectra with preliminary CTA differential sensitivity curves, for different observing times. We found that the most promising candidates are, again, local

and flat-spectrum sources. It will be possible to obtain a spectrum with the CTA for these sources with long (~ 250 hours) targeted observations. Comparing our results with current plans for an extragalactic blind-sky survey with the CTA, we find that this observing strategy does not appear to be ideal in order to detect and study more MAGN in the TeV band. This would require long targeted observations of the most promising TeV candidates.

This thesis is organized as follows. In Chapter 1 we give a general overview on AGN classification and unified models, the most important radiative processes which occur in AGN jets, and the detailed properties of the main subject of this work, i.e. radio galaxies. In Chapter 2 we present the main properties of the instruments and facilities which produced the data used in this work, i.e. the *Fermi* space telescope and the Cherenkov telescopes for VHE observations, including the next generation *Cherenkov Telescope Array*. Chapter 3 reports the multi-wavelength observational properties of our sample of TeV detected radio galaxies. In Chapter 4 we report the methods adopted for the analysis of *Fermi*-LAT data on these four MAGN, and present the spectral and timing results, including the analysis of their MeV-TeV spectra. In Chapter 5 we give an overview of the 3LAC MAGN sample, then we report the methods and results of our predictive analysis for our candidate sources and for the current TeV radio galaxies, in terms of integrated flux detections and spectral analysis. In Chapter 6 we discuss our results, both for the *Fermi* data analysis and for the CTA predictions. Finally, in the Conclusions we summarize the main results of this study and the future prospects for this line of work.

Chapter 1

Active Galactic Nuclei

Active Galactic Nuclei (AGN) are among the most powerful sources of radiation in the universe. This radiation spans the entire electromagnetic spectrum, from radio wavelengths to VHE γ-rays, with bolometric luminosities from 10^{42} erg/s up to 10^{49} erg/s. This exceptionally high luminosity, together with the compactness of the emission and its peculiar spectral properties like the presence of strong broad emission lines and the bright and blue continua, is what set apart AGN as a new class of astronomical objects in the first studies. AGN were studied systematically for the first time by Seyfert in 1943 [149], and since then have become one of the main fields of research in astronomy.

AGN are hosted in a compact region in the nuclei of a small ($\sim$1%) fraction of galaxies. Their extremely energetic output is believed to be fueled by accretion of large amounts of material onto a supermassive black hole (SMBH)[1] at the center of the AGN. This scenario was quickly accepted as the only plausible model which was capable of resulting in such extreme observed properties. This is due to the high efficiency of the accretion process in converting gravitational energy into radiation, capable of accounting for the large observed luminosities, and to the unique physical conditions of black holes, which account for the extremely large masses inferred to be confined in very compact volumes.

It is now commonly accepted that almost every massive enough galaxy has a SMBH at its center, that strongly interacts with the surrounding environment, as demonstrated by dynamical arguments as e.g. the so called "M-σ" relation, which links the velocity dispersion of an elliptical galaxy (or the bulge of a spiral galaxy) to the mass of its central object [113][65][116]. If the SMBH is fueled with infalling gas it becomes active, giving rise to an AGN.

---

[1]SMBHs have masses of the order of 10^6-10^{10} M$_\odot$, as opposed to stellar-mass BHs with masses of the order of 1-10^2 M$_\odot$. The existence of Intermediate Mass Black Holes (IMBH) with $10^2 M_\odot < M_{BH} < 10^6 M_\odot$ is expected, but conclusive evidence for it is still lacking.

1.1   The AGN *Spectral Energy Distribution*

In general, AGN are powerful sources of radiation over the whole range of the electromagnetic spectrum. This emission is characterized by a *Spectral Energy Distribution* (SED) which presents some typical recognizable features along the various energy bands, from radio to γ-rays (see Fig. 1.1).

- **Radio**: this emission is of non-thermal origin, being mostly synchrotron radiation produced by relativistic particles spiraling in a magnetic field. The spectral shape of this emission is a power-law $F_\nu \propto \nu^{-\alpha}$ with a typical spectral index of $\alpha \sim 0.7 - 0.8$. Radio-loud AGN are the most prominent emitters at these wavelengths, thanks to their powerful jets of relativistic particles (see Section 1.2.1). In this sources the non-thermal synchrotron component is believed to contribute to all the low-energy emission from radio to optical-UV (and sometimes even X-rays).

- **Infrared**: this emission in radio-quiet AGN is dominated by the thermal contribution of the dusty obscuring structure believed to be present in most AGN (see Section 1.2.2). This component reprocesses the absorbed radiation coming from the central engine into thermal black-body emission. Another important contribution to the IR emission may come from star formation associated with the AGN hosting galaxy, mainly in starbursts[2]. As mentioned above, in radio-loud AGN the IR emission comprises also a contribution from non-thermal synchrotron radiation.

- **Optical-UV**: this portion of the spectrum is where many of the most distinctive AGN features are found. One of these is the so called "Big Blue Bump", which is a strong and broad excess peaking around 4000Å, that extends into the UV and soft X-rays. This component is believed to be associated with the accretion process, and namely with thermal multi-λ black-body emission by a geometrically thin, optically thick accretion disc, which constitutes the "central engine" of the AGN structure. This emission results from viscous heating of the material spiraling towards the SMBH, which reaches temperatures of about $T \sim 10^4 - 10^5$ K.

- **X-rays**: generally, X-ray emission is one of the most common AGN selection criteria. The main contribution to the hard X-ray ($E > 2$ keV) emission is believed to come from Inverse Compton (IC) upscattering of the optical-UV disc photons by highly energetic thermal electrons (a process called

---

[2]A starburst galaxy is a galaxy characterized by a star formation rate (SFR) much higher than usual (a consensus has yet to be reached over a quantitative definition). The excess IR emission in these galaxies is due to their population of hot, newly formed stars, whose radiation is absorbed and re-emitted by the surrounding dust.

Comptonization) residing in a so called *corona* above the disc, with a typical temperature of $T \sim 10^8 - 10^9$ K [85]. The resulting X-ray spectrum has the shape of a power-law with an exponential cutoff [3]

$$F(E) \propto E^{-\Gamma(k_B T, \tau)} e^{-[E/E_c(k_B T, \tau)]}$$

Typical spectral values are $\Gamma \sim 2$ and $E_c \sim 100$ KeV. Hard X-ray photons are emitted isotropically, so that part of them are absorbed and part reflected by the cold component, giving rise to the spectral feature known as *Compton hump*, a broad component peaking around 30 keV, and to the characteristic Fe Kα 6.4 keV fluorescence line. Another component seen in X-ray spectra of AGN is the so called *soft excess*, that is an excess emission below 2 keV superimposed on the power-law, whose origin is still debated [144][77][169]. This feature was first believed to be the high-energy tail of the Big Blue Bump associated with the accretion disc, but this hypothesis was ruled out because the inferred temperature remained nearly constant for a range of SMBH masses and AGN luminosities. Current hypotheses involve additional Comptonization or reflection components with complex ionization. Additionally, in Type 1 AGN (see Section 1.2.2) an absorption component is present in the soft region of the spectrum, associated with a so called *warm absorber*, believed to be ionized gas positioned along our line of sight (LoS) to the central engine. This gas displays a wide range of ionization degrees and column densities, is often modeled in multiple phases, and its absorption features are almost always blueshifted, implying an outflow origin [166].

- γ**-rays**: AGN dominate the sky at these energies, the main contributors being blazar sources, thanks to their relativistically boosted radiation (see Sections 1.2.1, 1.2.2, 1.3.4). The rest of the GeV extragalactic sources are other classes of radio-loud AGN, like radio-galaxies (see Section 1.4), starburst galaxies, or unidentified sources. The main emission mechanism at these energies is believed to be Inverse Compton scattering up to GeV and TeV energies of low-energy seed photons by a population of relativistic non-thermal electrons, the same electrons which produce the low energy synchrotron emission (see Section 1.3.2). The SED of blazars is in fact completely dominated by these two non-thermal components (the synchrotron branch at low energy and the IC branch at high energy) which, thanks to relativistic boosting, can sometimes swamp all other spectral features (see Section 1.3.4).

---

[3]Γ is the spectral index, k_B is the Boltzmann constant, T is the electron temperature, τ is the optical depth, and E_c is the cutoff energy.
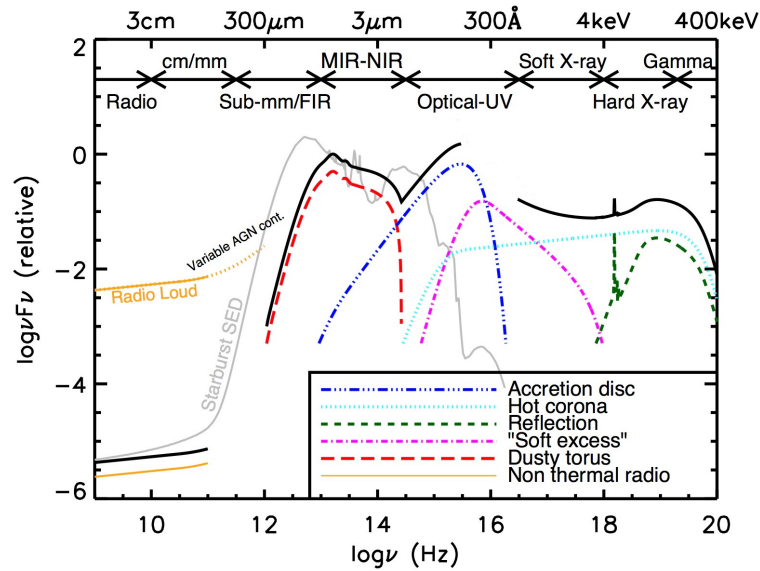
Figure 1.1: Representation of a typical AGN spectral energy distribution, from radio to γ-rays. Credit: Chris Harrison (URL:http://astro.dur.ac.uk/ cpnc25/research.html).

1.2 AGN classification and unification

The great number of observed AGN variants has created the need for classification, which was originally based on the observed properties of these objects. Building on this classification, in the last three decades the so called *unified models* have been developed in the attempt to understand the physical structure of AGN and their diverse manifestations. For a detailed review on these topics see Antonucci 1993 [25], Urry & Padovani 1995 [168], Tadhunter 2008 [158].

1.2.1 Classification: the AGN "zoo"

The main AGN observed "flavors" are:

- Seyfert galaxies (Sy): typically hosted at the center of spiral galaxies, these are relatively low-luminosity AGN, and are usually weak radio emitters. They are the most common class of AGN observed in the local universe, and owe their name to Carl Seyfert, who first studied them in his aforementioned work of 1943 [149].

- QSOs: Quasi-stellar objects (QSOs) can be considered the high-luminosity counterpart of Seyferts, with similar optical spectra. Quantitatively, Seyferts

with absolute magnitudes brighter that $M_B < 23$ are considered QSOs [147]. These sources are star-like (i.e. optically point-like) and usually high-z sources which dominate the radiative output of their host galaxy, making it difficult to determine its morphology.

- Quasars: Quasi-stellar radio sources, or Quasars, are the radio-loud counterpart of QSOs (see below). They are powerful radio emitters, and were first discovered in the early radio surveys (e.g. 3C, PKS). Their nature was not understood until it was realized that the broad emission lines observed in their optical spectrum were ordinary Balmer lines with a large redshift. Based on their radio spectral index, they are divided into Flat-Spectrum Radio Quasars (FSRQs, $\alpha \leq 0.5$) and Steep-Spectrum Radio Quasars (SSRQs, $\alpha \geq 0.5$). The distinction between quasars and QSOs is mainly historical, but today the term "quasar" is often used to refer to either class of sources.

- Radio galaxies (RGs): this class of AGN is characterized by a typical radio morphology made of different components. They usually have a bright and compact *core*, and collimated *jets* extending from the core up to kpc and sometimes Mpc scales, which end in diffuse structures called *lobes*, sometimes forming *hot spots*, i.e. bright compact regions at the lobes' outskirts (figure). For more details on radio galaxies see Section 1.4.

- Blazars: with this term we indicate sources having a star-like optical appearance, high luminosity and radio power, just like quasars, but which also display strong and rapid flux and polarization variability. Within this class of objects we can find FSRQs[4] (mentioned above), and BL Lacs, which are characterized by a featureless optical continuum. BL Lacs are named after the prototype object BL Lacertae, which was at first believed to be a variable star, but was later associated with a radio source [146]. With the discovery and study of various objects with similar features, BL Lacs were established as a class of AGN during the 1970s [157][155].

An important distinction between these AGN classes is the one between *radio-loud* (RL) and *radio-quiet* (RQ) AGN. About 10-20 % of AGN are radio-loud [168]. This definition is traditionally based on the ratio between radio power at 5 GHz F_{5GHz} and optical flux in the B band F_B, which is sometimes referred to as the *radio-loudness parameter R*. Namely, a source is considered radio-loud when [98]

$$R = \frac{F_{5GHz}}{F_B} \geq 10$$

---

[4]FSRQs can be further divided into Optically Violent Variables (OVVs) and Highly Polarized Quasars (HPQ).

A more recent definition of the radio-loudness parameter considers the X-ray 2-
10 keV (unabsorbed) luminosity of the source instead of the optical flux, thus
including the AGN with a heavily obscured optical flux ($A_v \geq 50 mag$)[164].

$$log(R_x) = log \left[\frac{\nu L_{\nu,5GHz}}{L_x} \right] \geq -4.5$$

As for radio morphology, radio-loudness is associated with the presence of highly
collimated jets of relativistic particles. The triggering and launching mechanism
of these jets, and therefore the physical parameters and conditions under which
an AGN becomes radio-loud, constitute one of the most debated and studied
topics in this field.
RL AGN are hosted exclusively in elliptical galaxies, while RQ AGN can lie both
in elliptical and spiral galaxies.

AGN can be further divided, on the basis of their optical spectrum, in *Type
1* AGN, with a bright and blue continuum, together with narrow forbidden lines
and broad (FWHM$\sim 10^3$-10^4 km s^{-1}) permitted lines; and *Type 2* AGN, which
have a weaker continuum and narrow forbidden *and* permitted lines (FWHM$\sim 10^2$
km s^{-1}), i.e. they lack broad lines.
As for the physical conditions of the line-emitting gas, the broad lines can be as-
sociated with dense gas clouds ($n_e \sim 10^9$ cm^{-3}) photoionized by a central source
which dominates the local gravitational field. These clouds orbit around this cen-
tral object, forming the so-called *Broad Line Region* or BLR, moving with high
velocities that produce the observed line width by Doppler broadening. Through
simple keplerian dynamical arguments, this velocities imply that the BLR clouds
must reside relatively close to the central photoionizing source, at scales of the
order of $R_{BLR} \sim 10^{16}$-10^{17} cm.
The narrow lines, on the other hand, are consistent with being emitted by low-
density gas clouds ($n_e \sim 10^3$-10^4 cm^{-3}), forming the so-called *Narrow Line Region*
or NLR. The narrow line width implies much smaller orbital velocities, and there-
fore a much larger scale for these clouds with respect to the BLR ones, of the
order of $R_{NLR} \sim 10^{18}$-10^{20} cm. Based on this commonly accepted interpretation,
in Type 1 AGN we are able to see both the BLR and the NLR, while in Type 2
AGN we only see the NLR. A possible explanation for these differences is that
in Type 2 AGN the central engine and the BLR are obscured by an intervening
absorber made of dust and gas.

The observed AGN classes fall in a combination of these classifications, with
luminosity as a third parameter. For example, a radio galaxy displaying broad
lines in its optical spectrum is a Type 1 RL AGN, and is called Broad-Line
Radio Galaxy (BLRG), while its Type 2 counterpart is called Narrow-Line Radio
Galaxy (NLRG). These two classes are the radio-loud counterparts of Type 1

and 2 Seyferts (Sy1 and Sy2), respectively, which in turn are themselves the low-luminosity counterpart of radio-quiet QSOs.

1.2.2 Unification: the orientation based unified models

Over the last three decades, parallel to the advance of observational studies on AGN, the so called *unified models* have been developed on the theoretical side. The basic idea behind these models is that all AGN have similar intrinsic properties and therefore belong to the same parent population, and their different observed manifestation can be ascribed to differences in orientation.

This approach is motivated by the ample observational evidence that points towards an *anisotropic* emission structure for AGN. In RQ AGN the anisotropy is explained with the presence of the dusty obscurer mentioned above, which is assumed to have a toroidal shape, and therefore is capable of obscuring our view towards the central engine and the BLR, but not the NLR, if viewed edge-on. This scenario is associated with Type 2 AGN, while in Type 1 AGN we view the obscuring torus face-on [140][27][28][159][105][61].
In RL AGN there is an additional cause for anisotropy, with the presence of relativistic jets. Radiation produced in these jets can be strongly Doppler-boosted if they are oriented at small angles with our line of sight (LoS), so that it is able to "swamp" all the other contributions to the source's emission, namely the host galaxy and the central engine. This would explain the observed properties of blazars by characterizing these sources as the aligned counterpart of a misaligned parent population, which would be constituted by radio galaxies. In particular, FSRQs and BL Lac would be the aligned counterpart of FR II and FR I radio galaxies (see below for this classification) [43][127][103][69].

These orientation-based unified models have been very successful in explaining many of the observed properties of the various AGN classes,in particular the Type 1-Type 2 dichotomy, but it is important to stress that they are a generalization and simplification of a very complex and diverse phenomenon, which they surely cannot explain in all its manifestations. One of the main unresolved issues in this scenario is for example the RL-RQ dichotomy, which is difficult to explain in terms of pure orientation effects, but is more likely related to an intrinsic difference between these sources. A visual summary of the concepts described above is given in Fig. 1.2: the observed AGN type depends on the viewing angle, the presence or absence of a jet, and the power of the central engine.
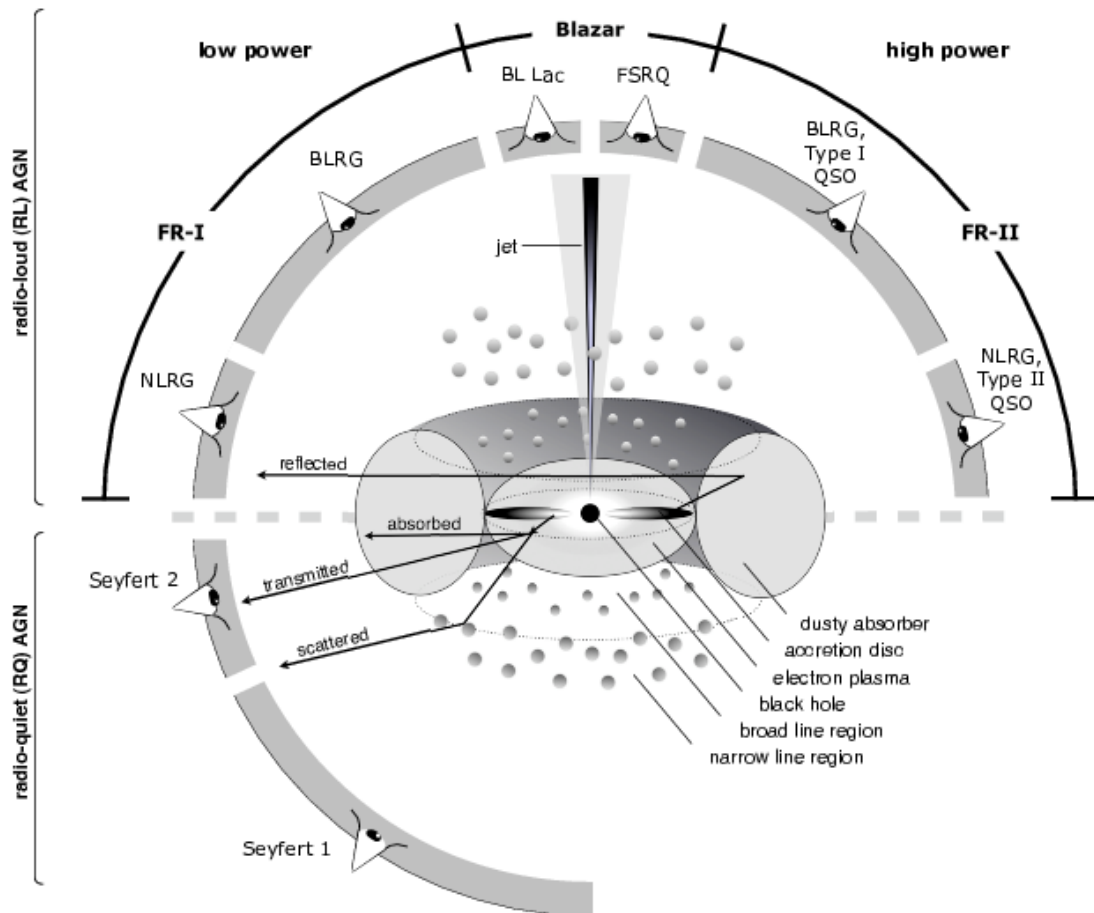
Figure 1.2: Schematic representation of the orientation based unified model (image from [37], page 132).

1.3 Radiative processes is radio-loud AGN

In this section we give a brief overview of the main physical processes responsible for the emission observed in radio-loud AGN, concentrating on the non-thermal ones. For a detailed discussion see Rybicki & Lightman 1986 [141], or the recent review by Ghisellini 2013 [73].

1.3.1 Synchrotron emission

The synchrotron emission process accounts for the low-energy component in the SED of radio-loud AGN, which for this reason is often referred to as the synchrotron component (or peak).

The synchrotron process occurs when a charged relativistic particle is accelerated in a magnetic field. When a particle with charge e and Lorentz factor

$$\gamma = \frac{1}{\sqrt{1 - v^2/c^2}} \tag{1.1}$$

travels through a uniform and static magnetic field B, it will experience a Lorentz force perpendicular to its direction, and therefore will travel with constant velocity in the direction of the field but with a circular motion in the perpendicular plane, i.e. will spiral around the direction of the field, with a frequency

$$\nu = \frac{eB}{2\pi\gamma mc} \tag{1.2}$$

When a charged particle accelerates it radiates energy, and in this case the radiated luminosity is given by [141]

$$L_{syn} = \frac{4e^4 B^2 E^2}{9m^4 c^7} \propto B^2 E^2 \tag{1.3}$$

where E is the energy of the particle. An artistic representation of the synchrotron process is given in Fig. 1.3.

In radio-loud AGN, synchrotron emission is produced by an ensemble of relativistic electrons. The total emission can be calculated by integrating over the energy distribution of the electrons. Assuming that this distribution is a power-law of the form $N(E) = N_0 E^{-\delta}$ [5], the resulting emission spectrum is also a power-law, with a flux density $S_{syn}(\nu) \propto \nu^{-\alpha}$, where the spectral index is $\alpha = (\delta - 1)/2$, and has typical values of $0.5 < \alpha < 1$. This spectral form is valid if the electrons are optically thin with respect to their emitted photons. This is only true above

---

[5]This is supported by observations of the energy spectrum of cosmic rays, which are believed to be accelerated through similar processes.
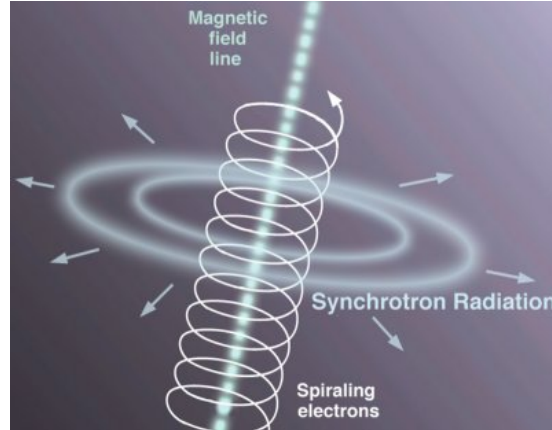
Figure 1.3: Artistic representation of the synchrotron emission process. Image: Jon Lomberg/Gemini Observatory.

a critical frequency ν_{max}. Below this frequency a significant fraction of the synchrotron photons is absorbed by interactions with the same emitting electrons (a process called *Synchrotron Self-Absorption*, or SSA). The overall spectrum is therefore given by

$$S_{sync}(\nu) \propto \begin{cases} \nu^{5/2} \text{ for } \nu < \nu_{max} \\ \nu^{-\alpha} \text{ for } \nu > \nu_{max} \end{cases} \tag{1.4}$$

Moreover, at still higher frequencies the most energetic electrons lose energy more rapidly, therefore there is a cutoff due to this radiative losses. Fig. 1.4 shows a typical synchrotron spectrum.

1.3.2 Inverse Compton emission

The Inverse Compton (IC) process takes place when a low-energy photon interacts with an ultra-relativistic particle, and is upscattered to higher energies. This process is the most popular and simple assumption which is made to explain high-energy emission from radio-loud AGN, although it has become clear that it cannot be the only relevant emission process at these energies.

The frequency of the observed photon after the scattering is related to its original frequency by a factor $\nu' \sim \gamma^2 \nu$, so the photon's energy gain is $E' \sim \gamma^2 E$, where γ is the electron Lorentz factor. For interactions with ultra-relativistic electrons, this factor can be large enough to upscatter a photon from the radio-IR band up to the X-ray and γ-ray band.

The luminosity produced at high energy via the IC process depends on the electron Lorentz factor, on the density of seed photons, and on the photon-electron
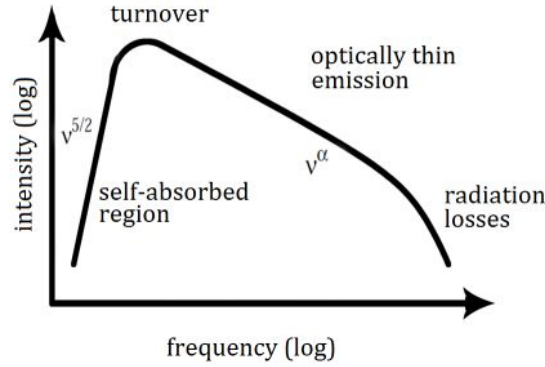
Figure 1.4: Schematic representation of a typical synchrotron spectrum. The spectral index α is assumed to be negative in the figure. Credit: Special Astrophysical Observatory of the Russian Academy of Sciences (URL: http://www.sao.ru/hq/giag/gps-en.html).

cross section, therefore it is given by

$$L_{IC} = \frac{4}{3}\frac{v_e^2}{c}\sigma_T\gamma^2 U_{ph} \propto \gamma^2 U_{ph} \tag{1.5}$$

where U_{ph} is the energy density of the seed photon field and σ_T is the Thomson cross section. This expression is valid for photon energies $h\nu \ll m_e c^2$, and represents the so called Thomson scattering regime. For higher seed photon energies we enter the Klein-Nishina regime, where the cross section is reduced as the photon energy increases, thus decreasing the luminosity. The IC spectrum then cuts off quite sharply at high energies. Eventually, for very high seed photon energies the luminosity becomes negative and the photon loses energy to the electron, going back to the direct Compton scattering.

In radio-loud AGN, the seed photons for the IC process may come from two main sources. If these photons are the synchrotron photons emitted by the same relativistic particles responsible for the IC scattering, the process is called *Synchrotron Self Compton* (SSC). If, on the other hand, the low-energy seed photons come from an external source, like for example the AGN accretion disc or the CMB, the line-emitting regions or the torus, then the process is called *External Compton* (EC).

In the case of SSC, it can be shown that the ratio of the IC luminosity to the synchrotron luminosity is simply given by the ratio of the energy densities of the seed photon field and of the magnetic field

$$\frac{L_{IC}}{L_{syn}} = \frac{U_{ph}}{U_B} \tag{1.6}$$

The peak frequencies of the two components of the SED (synchrotron and SSC), are related by the simple IC relation mentioned before, i.e. $\nu_{IC} \sim \gamma_{max}^2 \nu_{syn}$, where γ_{max} is the maximum Lorentz factor in the electron distribution.

1.3.3 Hadronic models

The emission processes discussed above have been used to explain the total non-thermal emission of radio-loud AGN, from radio to TeV energies. This radiation is therefore attributed to a population of relativistic electrons accelerated by the central engine of the AGN, and for this reason these models are called *leptonic* emission models. Although they have proven to be generally successful in explaining the SED of radio-loud AGN, there are now several cases of TeV detected AGN (mostly high-energy peaked BL Lacs, HBLs), in which they cannot account for the observed VHE radiation, without an unrealistic fine tuning of the model parameters (see e.g. Cerruti et al. 2015 [49] and references therein).

For this reason, *hadronic* or *lepto-hadronic* models have been developed. In these models, a leptonic population is associated with the low-energy component of the SED, and to the MeV-GeV γ-ray portion of the high-energy component, via SSC processes. An ultra-relativistic hadronic (i.e. proton) component is also considered, which can interact with low-energy photons forming pions (both neutral and charged), or $e^+ e^-$ pairs. This particles can interact again with the low-energy photon field, giving rise to electromagnetic cascades. The resulting emission is then a combination of synchrotron emission from protons and from $e^+ e^-$ pairs produced either by $p\gamma$ interactions, $\gamma\gamma$ interactions or pion decay. These models have been proven to give an acceptable reproduction of the SED of blazars, particularly at high and very high energies [49].

The presence of ultra-relativistic protons in AGN jets also implies the need for very high jet powers, often exceeding the amount of energy produced in the accretion process [75]. This would favor models in which the jet power is provided not only by accretion, but also by the extraction of rotational energy from a highly spinning SMBH. This is possible if a large magnetic flux is accumulated in the vicinity of the SMBH, as predicted by the so called Magnetically Arrested Disk (MAD) models [163] [172].

An interesting byproduct of considering an hadronic component in radio-loud AGN is the possibility to identify them as the sources of the Ultra-High-Energy Cosmic Rays (UHECRs) observed on Earth, which reach energies up to 10^{20} eV [99], and cannot be produced by galactic sources. Providing evidence for the presence of protons accelerated at extreme energies would then constitute a plausible solution to this problem.

Additionally, hadronic processes could also provide plausible sources for the PeV neutrinos recently observed by the IceCube instrument [1]. The association

of these neutrinos with HBL blazars has recently been investigated by Padovani & Resconi 2014 [132]. Conversely, association of the observed neutrinos with an AGN would provide definitive evidence for hadronic processes in these sources.

1.3.4 Relativistic effects

In radio-loud AGN the observed non-thermal emission is coming from a population of particles residing in the jet, which moves with bulk relativistic speed. This implies two different effects. The emitted radiation is beamed in the direction of motion, with an angle given by $\theta_A \sim 1/\Gamma_{jet}$. Moreover, the more the jet is aligned with the observer's line of sight (l.o.s), the more the emitted radiation is boosted by relativistic Doppler effect.

To see this, we consider the specific intensity emitted by a single component moving with the jet's bulk velocity, i.e. the emitted flux per unit frequency and solid angle. In the observer's reference frame, this would be

$$I(\nu) = \frac{h\nu \; dN}{dt \; d\nu \; d\Omega \; dA} \tag{1.7}$$

Considering the relativistic transformation of frequencies, time, and solid angle, between the observer's frame and the jet rest frame, i.e.

$$\begin{aligned}
\nu &= \delta \; \nu' \\
d\nu &= \delta \; d\nu' \\
dt &= dt'/\delta \\
d\Omega &= d\Omega'/\delta^2
\end{aligned} \tag{1.8}$$

we obtain the result

$$I(\nu) = \delta^3 I'(\nu') \tag{1.9}$$

where $\delta = [\Gamma(1 - \beta cos\theta)]^{-1}$ is the Doppler factor. Integrating over frequencies we obtain the flux transformation

$$F = \delta^4 F' \tag{1.10}$$

This orientation-dependent effect is the reason for the differences in the observed emission coming from blazars and radio galaxies, as mentioned above.

1.3.5 Extragalactic Background Light absorption of TeV photons

When studying high-energy γ-ray emission from relatively far (e.g. z>0.1) sources, one has to consider the overall opacity of the universe to this radiation, since the

photons have to travel a long way before reaching the observer, and therefore may undergo absorption processes. The most relevant is absorption via pair-creation with background photons in the optical/IR band. This background is usually referred to as Extragalactic Background Light (EBL), which is a diffuse background produced by the sum of the light from stars, galaxies and AGN over cosmic time. Fig. 1.5 reports the EBL SED in the model by Dominguez et al. 2011 [57].
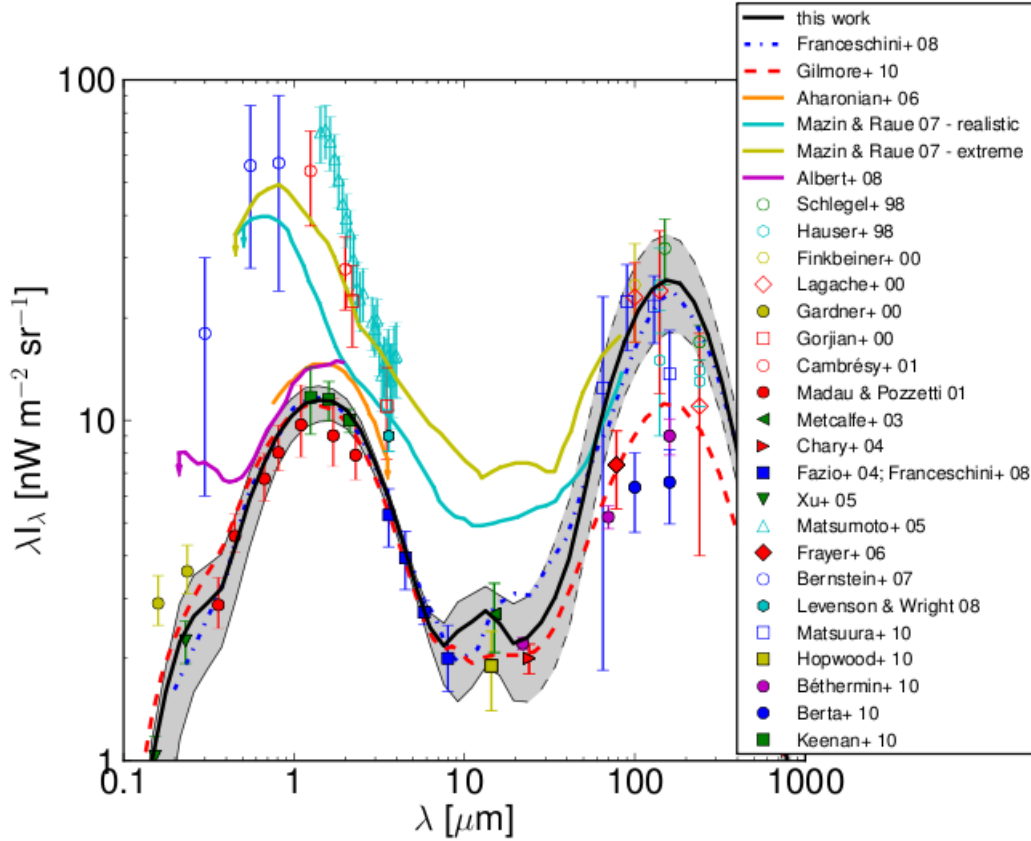

Figure 1.5: Figure 13 from Dominguez et al. 2011 [57]. Spectral Energy Distribution of the EBL. The black solid line represents the model from Dominguez et al. 2011.

The cross section for this process is a strong positive function of the γ-ray photon energy. For a γ-ray photon of energy E, it reaches a maximum at

$$\epsilon \sim \frac{520 \text{ GeV}}{E \text{ (GeV)}} \text{ eV} \tag{1.11}$$

For example, a photon with $E = 1$ TeV will interact most strongly with an EBL photon of energy $\epsilon \sim 0.5$ eV, which corresponds to the near-IR band ($\sim 2.5 \mu m$).

Since EBL absorption becomes more severe as the photon energy increases, it has the effect of softening the TeV spectrum of the source. This dependence is illustrated in Fig. 1.6, which shows the EBL optical depth τ as a function of the γ-ray photon energy, for different values of the redshift.
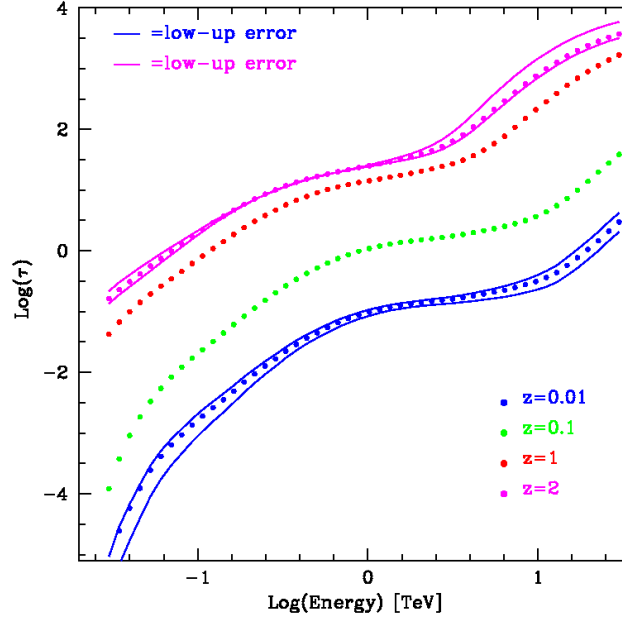

Figure 1.6: Log-Log plot of the EBL optical depth versus the γ-ray photon energy. The colored dotted curves correspond to a different redshift: 0.01 (blue), 0.1 (green), 1 (red), 2 (magenta). The colored solid lines represent the uncertainties on τ at the corresponding redshift. Credit: MSc thesis by Alessandra Marandola, Università di Bologna, 2013.

Measuring the SED of the EBL is quite difficult, due to contamination from single sources, therefore the exact spectral shape is still controversial, with a variety of models proposed (see Fig. 1.5). Once a model is assumed, it is possible to calculate the attenuation of γ-ray photons from EBL absorption as an optical depth $\tau(E, z)$. The observed flux will therefore be related to the intrinsic emission by

$$F(E, z) = F_0(E)e^{-\tau(E,z)} \tag{1.12}$$

Knowing the source redshift, and assuming an EBL model, it is possible to calculate the correction to the observed TeV data in order to reconstruct the intrinsic spectral shape, or to absorb a simulated spectrum.

1.4   Radio galaxies

We now turn to describe in more detail the properties of the main subject of this work, i.e. radio galaxies.

1.4.1   Radio morphology: FR I & FR II

The main morphological components of a radio galaxy are:

- **Core**: bright compact central component, spatially coincident with the center of the source's optical counterpart. It is very difficult to resolve even with VLBI mas ($\sim$sub-pc) resolution, and is characterized by a flat radio synchrotron spectrum ($\alpha \sim 0$). It is assumed that this spectral shape is the sum of different emission components affected by Synchrotron Self Absorption (see e.g. Marscher 1988 [112]). The core is believed to be associated not with the SMBH itself but rather with the innermost base of the relativistic jets. Its contribution to the total emission is usually relatively small (0.1% to a few %), excluding peculiar classes of core-dominated sources.

- **Jets**: linear highly collimated structures extending from the core up to kpc or even Mpc scales. These are jets of relativistic particles accelerated in the core, which emit non-thermal radiation at different wavelengths. In the radio band this emission is confidently associated with synchrotron radiation, while in the X-rays (when it is observed) it could be produced by Inverse Compton scattering of CMB photons with the relativistic particles in the jet.

  Assumed to be intrinsically symmetric, they are usually one-sided, because of the difference in the velocity component along our LoS between the approaching and the receding jet (or counter-jet), which is given solely by orientation. The observed difference is due to the fact that radiation coming from material which is moving with relativistic speed towards the observer suffers from strong Doppler-boosting, while the opposite is true for material moving away from the observer. On pc scales the jet is often structured in discrete components called "knots" or "blobs", which may exhibit apparent transverse superluminal motion due to relativistic effects, coupled with orientation.

  The jets are the means by which the diffuse extended structures called lobes are fueled with the relativistic particles responsible for their synchrotron emission. The efficiency of this transport is based on the amount of radiative losses suffered by the particles along the jet, i.e. a more luminous jet implies a less efficient transport. The non-thermal jet radiation completely

dominates the total radiative output of blazars, emitting from radio to γ-rays, while in radio galaxies the thermal contribution of the central engine and the host galaxy to the low-energy peak of the SED is not negligible.

- **Lobes**: diffuse extended structures at the end of the jets, characterized by a steep radio spectral index ($\alpha \sim 0.7 - 1.0$), indicating that, contrary to the core, the electron population lacks an efficient supply of new energetic particles [6].

- **Hot-spots**: compact spots of enhanced radio emission, which are also visible in X-rays, where the jet impacts with the ISM at the edges of the diffuse lobes, generating shocks which re-accelerate the transported particles.

Radio galaxies can be divided depending on their total radio power in two classes, which exhibit different morphologies, in terms of the relative contribution of the components described above. Sources with a total radio power at 178 MHz greater than $\sim 10^{25}$ W Hz^{-1} sr^{-1} are called Fanaroff-Riley type II radio galaxies (FR II), or *edge brightened*, because they have bright hot-spots at the edge of the lobes, and a weak emitting and well collimated jet (often one-sided), suggesting an efficient particle transport mechanism with low radiative losses. The jet seems to maintain relativistic speed up to kpc scale.

On the other side of this divide are Fanaroff-Riley type I radio galaxies (FR I), which have weak or absent hot-spots (or *edge darkened*) and brighter jets, sometimes with a non-linear structure, suggesting a more inefficient particle transport mechanism. In this case the jet decelerates to sub-relativistic speed on large scale, although it is not known exactly at what scale this deceleration takes place. Fig. 1.7 shows radio images of two classical FR I and FR II radio galaxies, with the distinctive morphological features described above.

This classification owes its name to Fanaroff and Riley which first studied it in 1974 [64]. Later it was discovered that this divide is quite sharp, and besides radio power it has also a mild dependence on optical luminosity [128][129], with FR I sources being found in optically brighter host galaxies than FR IIs, at the same radio power.

Another important classification of radio galaxies is based on the optical emission lines, and divides these sources into *High Excitation Galaxies* (HEG), and *Low Excitation Galaxies* (LEG). A radio galaxy is classified as LEG if $EW_{[OIII]} < 10\mathring{A}$ and/or [OII]/[OIII] > 1 [93][104]. While FR Is always display LEG spectra, it was found that FR IIs can be both HEGs or LEGs.

---

[6]As a radio-emitting electron population ages, the most energetic particles lose energy more quickly, so the overall spectrum gets more steep with time, if new energetic particles are not injected in the population.
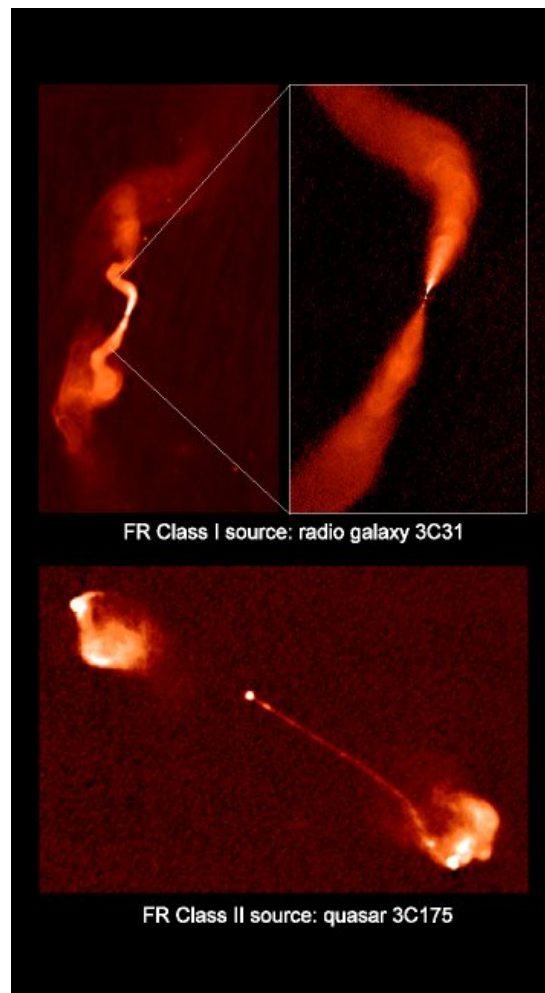
Figure 1.7: Examples of classic FR I (3C 31, top panel, VLA 20 cm map) and FR II (3C 175, bottom panel, VLA 6 cm map) radio galaxies, where we can see the distinctive morphological features described above. Credit: NRAO.

1.4.2 The *Fermi*-LAT view of radio galaxies

As mentioned in Section 1.1, the majority of all observed γ-ray sources are AGN, mainly blazars, whose extreme output at these high energies is due to the non-thermal Doppler-boosted radiation of a jet pointing at small angles with our LoS, which dominates the total radiative output of the source.

In this framework radio galaxies, being Misaligned AGN (MAGN), i.e. whose jets are usually pointing away from our LoS, are not expected to be favored γ-ray sources. Their detection by *Fermi* was nonetheless predicted by Ghisellini et al. 2005 [72] in light of a new emission model for the jet of radio-loud sources (see below), and by Grandi & Palumbo 2007 [84], who discussed the non-thermal contribution of the jet to the X-ray nuclear emission of radio galaxies. Indeed, thanks to *Fermi*-LAT MAGN have been established as γ-ray sources in the last few years, with the detection of 24 objects (see Table 1.1), including the four radio galaxies which constitute the sample studied in this work (see Chapter 3).

Abdo et al. 2010 [5] analyzed 15 months of LAT data on MAGN, and discussed their overall properties as a sample, although this approach suffers from low statistics. All sources are detected with high significance, although the average flux is low, of the order of $F_{>100MeV} \sim 10^{-8}$ photons cm^{-2} s^{-1}. The mean spectral shape is that of a relatively steep power-law, with seven sources displaying spectral indices larger that ~ 2.3. The distribution of luminosities and spectral indexes reproduces the FR I-FR II dichotomy, with FR IIs being more γ-ray luminous. A comparison with the γ-ray properties of blazars shows that FR I and FR II sources have γ-ray properties similar to those of BL Lacs and FSRQs, thus favoring the current orientation-based unified schemes.

It is worth noting that the majority of the sample is made of FR I sources. This statistical feature becomes more evident by looking at the γ-ray-to-radio detection rate, which is much lower in FR II sources than in FR Is [81]. The simplest interpretation of this statistical behavior is to associate the paucity of LAT-detected FR IIs with their larger redshift (on average) with respect to FR Is, but this hypothesis does not seem to be supported by the data. Another interpretation is based on the hypothesis that the main γ-ray emission mechanism is SSC for FR Is and EC for FR IIs. In the latter case the Doppler boosting of the upscattered photons is stronger, and the beaming cone is narrower than in the case of SSC. Therefore, the beaming difference between these two processes could explain the lower γ-ray detection rate of FR IIs, because a narrower beaming cone implies stronger deboosting of radiation for a jet not aligned with the observer's LoS. This hypothesis is supported by studies of the AGN environment of radio galaxies, that show a richer photon field for FR IIs, produced by e.g. an efficient accretion disk, the line-emitting regions or the torus, capable of providing abundant seed photons for the EC process, with FR Is characterized in turn by a poorer environment,

and thus more likely to emit at high energies via SSC [167].

Finally, another hypothesis is that jet activity is more often triggered in FR Is than in FR IIs, thus resulting in a higher detection probability for the former class. Indeed, a variability analysis of 4 years of MAGN LAT data by Grandi et al. 2013 [82] has shown that FR Is and FR IIs have a substantially different temporal behavior. FR Is are detected (i.e. they have TS>10 [7]), on average, $\sim 70\%$ of the total time span covered by the data, while FR IIs have a time detection coverage of only $\sim 30\%$, suggesting that their flux rises above the LAT threshold only during short and intense flares.

One of the appeals of MAGN studies is that their misaligned jet provides us, in principle, with the opportunity to locate the γ-ray emission region. This is one of the main open issues in γ-ray studies of radio galaxies, because this information, and more specifically the distance from the central BH, has a strong impact on the physical models which try to reproduce the observed γ-ray emission. Unfortunately the spatial resolution of the LAT is in most cases insufficient to associate the high-energy emission with e.g. the core rather than with knots in the jet.
Since the IC process requires highly energetic particles, one could naïvely assume that the emission region must be as close as possible to the particle accelerator, i.e. the close surroundings of the SMBH, and therefore locate it in the radio core, which is considered to correspond with the base of the jet. However evidence in support of this assumption is still missing, while on the contrary the detection of γ-ray emission from the extended lobes of Cen A (which is one of the very few cases in which it is possible to resolve different components with the LAT, see Section 3.2) contributes to confuse this picture, since it is difficult to explain the presence of highly energetic particles at such a large distance from the central engine.

The lack of sufficient resolution implies that in most cases the only spatial information that can be obtained is the size of the γ-ray emitting region, which can be constrained from the source's variability timescale Δt using causality arguments, by assuming $R \le c\Delta t\delta/(1 + z)$, where δ is the Doppler factor [8]. For MAGN this approach is hampered by the low photon statistics, i.e. it is difficult to statistically assess a temporal variability with a reasonable binning, because the likelihood method is not likely to converge without a sufficient number of photons per temporal bin. Additionally, contribution from a stationary diffuse component, as seen in Cen A, could dilute the variable emission from the compact source, preventing a statistically valid estimate of a variability timescale. For the few sources bright enough to have good statistics however, like NGC

---

[7]See Section 4.1.2 for the definition of the Test Statistic
[8]See Section 1.3.4 for a definition of the Doppler factor.

1275, variability has been established on timescales down to the order of weeks (see Section 3.1), indicating an extremely compact emitting region.

Another reason to study the high energy emission from MAGN is to test common assumptions on the emission models in the framework of the unified model. For example study of the SED of FR I radio galaxies has provided evidence that a one-zone Synchrotron Self-Compton (SSC) model, which is the most simple and common assumption used to explain the double-peaked SED of relativistic jetted sources, is inadequate as it can only fit the data if one assumes a Lorentz factor for the jet of the order $\Gamma \sim 2 - 3$, which is significantly smaller than those required in BL Lacs ($\Gamma \geq 10$), assumed to be their aligned counterpart [51]. Different models have been put forth to explain this discrepancy, proposing for example a structured jet (Ghisellini et al. 2005 [72]) or a decelerating jet (Georganopoulos et al. 2003 [70]). In particular the former model, called *spine-layer scenario*, assumes that the jet has a transverse velocity structure, with an inner faster "spine" which is predominant when the jet is aligned, accounting for the high Lorentz factors inferred for blazars, and a slower external "layer" which dominates the emission when the jet is misaligned, thus reproducing the observed properties of radio-galaxies. Evidence for transverse structure in the jets of radio galaxies has indeed been found very recently by Nagai et al. 2014 using radio VLBA imaging of NGC 1275, one of the sources in our sample (see Section 3.1) [121]. Motivated by these observations, Tavecchio & Ghisellini 2014 applied their spine-layer model to the overall SED of NGC 1275, finding a satisfactory agreement with the data [161].

1.4.3   Radio galaxies at VHE and the impact of the CTA

As mentioned in Chapter 3, the only non-blazar sources detected in the VHE domain (E>100 GeV) so far are the four radio galaxies which are the subject of this work. Of these sources three are classified as FR Is (NGC 1275, M87 and Cen A), while the fourth, IC 310, is a peculiar source also classified as FR I but believed to be a transitional object with blazar-like properties (see Section 3.4).

The possibility that radio galaxies could constitute a new class of VHE sources was first proposed by Bai & Lee 2001 [32], who investigated the SEDs of Cen A and M87, stating that the peaks in the hard X-rays and far-UV bands observed for this two sources, respectively, were not the IC components of the classical double-peaked SED of jetted AGN, but corresponded to the synchrotron component instead. This in turn implied that the IC peak would lie at very high energies, and thus that Cen A and M87, along with similar nearby sources, might be promising TeV source candidates. Indeed M87 was the first non-blazar source to be detected in the TeV range (Aharonian et al. 2006 [13]), with strong variability on timescales of days, and it has been used as a test source for most of the VHE

emission models.

The mechanism through which this highly variable emission is produced is still debated, and several hypotheses have been put forth.

Neronov & Aharonian 2007 [124] discussed in detail the possibility that the observed γ-rays are produced by synchrotron and IC losses by relativistic electrons accelerated in gaps in the SMBH magnetosphere. In a state of equilibrium, the electric field in the magnetosphere is neutralized by charge redistribution. Because the charge distribution is not static, an inefficiency in charge supply could lead to the formation of gaps in which the electric field is not zero and can thus efficiently accelerate particles up to very high energies. This particles then emit via synchrotron and IC processes, and it is found that this first-generation photons can account for the emission above 10 TeV, while the emission at E≤10 TeV is dominated by secondary photons generated by electromagnetic cascades produced when the primary photons interact with the external radiation field. The authors found that this scenario can explain the observed TeV emission in M87.

Rieger & Aharonian 2008 [138], proposed a model in which VHE photons were produced via IC upscattering by electrons centrifugally accelerated up to VHE in the magnetosphere of a sub-Eddington accreting black hole. This acceleration mechanism is viable only for a low efficiency accretion regime, because a more efficient one would result in severe energy loss of the particles through IC upscattering of the over-abundant seed photon field, before they could be accelerated up to very high energies. The authors applied this model to M87, motivated by the low Eddington ratio inferred for this AGN, and found a satisfactory agreement with the spectral shape, luminosity and variability timescale of the observed TeV emission (another discussion of this model can be found in Levinson & Rieger 2011 [107]). The fact that all four VHE-detected radio galaxies belong to the FR I class, and thus are believed to harbor a SMBH with an inefficient ADAF-like accretion flow (see Ghisellini & Celotti 2001 [71]), lends support to this hypothesis for the production mechanism of TeV photons in these sources.

Tavecchio & Ghisellini 2008 [162] have attempted to interpret the strongly variable TeV emission from M87 in light of their spine-layer model for the jet [72]. They assume that the VHE photons are produced in the layer, while emission from the spine dominates the low energy component of the total SED. This is required to satisfy the radio-loud unified models, according to which FR I sources should appear as spine-dominated BL Lacs if their jet is aligned with the LoS: the authors found that this condition is satisfied only if the above configuration is assumed. They fitted their model to the observed SED, finding a notable disagreement in the slope of the TeV spectrum, i.e. the spine-layer model fails to reproduce the hard spectrum observed for M87 in the 2005 flare. This is due

to the suppression of multi-TeV photons via $\gamma\gamma$-absorption by the low energy photons from the spine, and this discrepancy is difficult to overcome within the model and the observational constraints. The effect could be less prominent assuming a larger emission region, but this solution contradicts the very compact size inferred from the short variability timescale.

Giannios et al. 2010 [76] proposed a jet-in-jet scenario in which the dissipation of magnetic energy in the jet gives rise to mini-jets of particles with relativistic speeds relative to the jet bulk motion in directions. It is found that if the angle between the mini-jet motion and the jet direction is greater than $\pi/2$, then the mini-jet emits outside the main jet emission cone, and thus it is possible for some mini-jets to point towards the observer, in a blazar-like fashion, even in sources in which the main jet is misaligned.

It is clear that with a sample of only four sources,it would be premature to draw statistical conclusions or to generalize the observed behavior to all radio galaxies as a class. The order of magnitude improvement in sensitivity provided by the CTA will allow the detection of more VHE emitting radio galaxies (see Section 5.2.1), as well as better photon statistics for the ones already detected (see Section 5.2.2), with an impact on all the different approaches used to investigate the nature of these sources [152]. Higher statistics will allow us to achieve better timing resolution, and thus more accurate multi-wavelength variability correlation studies, which are a fundamental tool for our understanding of these sources. More detailed temporal analysis is also important to constrain the size of the emission region for variable sources through causality arguments, thus allowing us to establish which morphological component dominates the TeV emission. This is an open issue, since the positional errors for VHE sources include both the core and the extended radio structure. The detection of variability, and thus the inference of a compact scale for the emission region, would exclude the diffuse component as the main source for the observed fluxes. The spectral analysis as well will benefit from the improved statistics, with the possibility of deriving more detailed spectra over an extended energy range. This would allow to test the spectral features predicted by the currently proposed emission models for VHE photons over a wider energy range with respect to current IACT instruments.

Object	1FGL Name	2FGL Name	3FGL Name	RA (J2000)	Dec (J2000)	z	Class
3C 78	J0308.3+0403	...	J0308.6+0408	03 08 26.2	+04 06 39.3	0.029	FR I
IC 310	...	J0316.6+4119	J0316.6+4119	03 16 42.8	+41 19 28.4	0.018	FR I
NGC 1275	J0319.7+4130	J0319.8+4130	J0319.8+4130	03 19 48.1	+41 30 41.9	0.018	FR I
Fornax A	...	J0322.4-3717	J0322.5-3721	03 22 41.5	-37 12 25.7	0.005	FR I
TXS 0331+391	...	...	J0334.2+3915	03 34 18.4	+39 21 25	0.0206	FR I
TXS 0348+013	...	...	J0351.1+0128	03 50 57.4	+01 31 06	1.12	SSRQ
3C 111	J0419.0+3811	...	J0418.5+3813	04 18 21.1	+38 01 35.7	0.049	FR II
3C 120	...	...	...	04 33 11.1	+05 21 15.6	0.033	FR II
Pictor A	...	...	J0519.2-4542	05 19 49.7	-45 46 44	0.035	FR II
PKS 0625-35	J0627.3-3530	J0627.1-3528	J0627.0-3529	06 27 07.0	-35 29 17.1	0.055	FR I
3C 189	...	...	J0758.7+3747	07 58 28.1	37 47 12	0.0428	FR I
4C+39.23B	...	...	J0824.9+3916	08 25 23.7	+39 19 46	1.21	CSS
3C 207	J0840.8+1310	J0840.7+1310	J0840.8+1315	08 40 45.8	+13 10 48.2	0.681	FR II
4C+39.26	...	...	J0934.1+3933	09 35 06.5	+39 42 07	...	SSRQ
3C 264	...	...	J1145.1+1935	11 45 05.0	+19 36 23	0.0217	FR I
4C+04.40	...	...	J1205.4+0412	12 06 19.9	+04 06 11	0.6285	SSRQ
M87	J1230.8+1223	J1230.8+1224	J1230.9+1224	12 30 49.3	+12 23 21.5	0.0036	FR I
3C 275.1	...	...	J1244.1+1615	12 43 57.6	+16 22 54	0.5551	SSRQ
Cen A	J1325.6-4300	J1325.6-4300	J1325.4-4301	13 25 28.0	-43 01 10.4	0.0009	FR I
3C 286	...	...	J1330.5+3023	13 31 08.3	+30 30 33	0.8499	CSS
Cen B	...	J1346.6-6027	J1346.6-6027	13 46 49.0	-60 24 29.9	0.0013	FR I
3C 303	...	...	J1442.6+5156	14 43 02.8	+52 01 37	0.141	FR II
NGC 6251	J1635.4+8228	J1629.4+8236	J1630.6+8232	16 32 26.1	+82 32 20.1	0.025	FR I
3C 380	J1829.8+4845	J1829.7+4846	J1829.6+4844	18 29 47.5	+48 46 12.6	0.692	FR II

Table 1.1: Table summarizing the sample of all *Fermi*-detected MAGN in the 3LAC catalog, adapted from Acker-mann et al. 2015 [11].

Chapter 2

γ-ray telescopes

2.1 Brief history of γ-ray astronomy

γ-rays are strongly absorbed by the Earth's atmosphere, therefore such radiation coming from astrophysical sources was not detectable until it was possible to get detectors above all or most of the atmosphere, with balloons or spacecrafts.

The first γ-ray space telescope was *Explorer 11*, launched in 1961, which measured an isotropic signal of less than 100 photons, attributed to a uniform γ-ray background produced by the interaction of cosmic rays with the ISM [100].

After the first detections of solar and galactic γ-ray photons from the *OSO-3* (1967) and *OSO-7* (1971) experiments [101] [53], the *SAS-2* (1972) [66] and *COS-B* (1975-1982) [41] satellites confirmed the detection of a γ-ray background and produced the first sky map at these wavelengths, although the poor spatial resolution was insufficient to resolve all but a small (~ 25) number of point sources.

These missions were followed by *NASA*'s *Compton Gamma-Ray Observatory* (*CGRO*) (1991-2000) [165], which conducted the first all-sky survey above 100 MeV and, thanks mainly to its *Burst And Transient Source Experiment* (*BATSE*, 0.02-8 MeV) and *Energetic Gamma-Ray Experiment Telescope* (*EGRET*, 20 MeV-30 GeV) instruments, made breakthrough γ-ray observations of blazars, pulsars, GRBs, solar flares and diffuse radiation, in addition to increasing the number of detected sources by an order of magnitude.

2.2 The MeV-GeV range: the *Fermi Gamma-ray Space Telescope*

The *Fermi Gamma-ray Space Telescope* is a *NASA* mission, in collaboration with government agencies from France, Germany, Italy, Japan, and Sweden. Launched on June 11, 2008, *Fermi* includes two instruments: the *Large Area Telescope* (LAT), and the *Gamma-ray Burst Monitor* (GBM).

2.2.1 The *Gamma-ray Burst Monitor*

The main purpose of the GBM is the spectral and temporal analysis of GRBs, but it also serves as a burst trigger for ground based follow-up observations, and for the LAT itself, with improved sensitivity and timing capability with respect to the *BATSE* instrument.

The GBM consists of 12 NaI(Tl) and 2 BGO scintillation detectors, which cover the low-energy (8 keV - 1 MeV) and high-energy (200 keV - 40 MeV) portions of the energy range, respectively. The main GBM performance capabilities, as reported in the paper by Meegan et al. 2009 [117], are listed in Table 2.1.

Table 2.1: Main *GBM* on-board performance capabilities.

Energy range	8 keV to 40 MeV
Energy resolution (FWHM)	$\sim 15\%$ at 100 keV; $\sim 10\%$ at 1 MeV
Trigger threshold	0.74 photons $cm^{-2}\ s^{-1}$
Burst location error	$< 15°$
Dead time per event	2.6 μs

2.2.2 The *Large Area Telescope*

The *Large Area Telescope* is the primary scientific instrument on board of the Fermi spacecraft. Its main goals are to:

- determine the nature of the unidentified sources detected by *EGRET*;

- investigate the particle acceleration processes operating in astrophysical objects like AGN, pulsars and SNR;

- study the high-energy behavior of GRBs;

- use of γ-rays as a probe for dark matter;

- understand the cosmic evolution of γ-ray sources up to high redshift ($z \geq 6$).

These scientific goals can be achieved thanks to the LAT's good imaging capability for source localization and multi-wavelength studies, high sensitivity, and good energy resolution. The main instrumental parameters of the LAT, as reported in the paper by Atwood et al. 2009 [31], are listed in Table 2.2.

The most up to date _Fermi_-LAT source catalog, the 3FGL, includes 3033 sources (see Acero et al. 2015 [9]). This implies an order of magnitude improvement with respect to the number of sources detected by the previous _EGRET_ instrument.

Table 2.2: Main LAT on-board performance capabilities.

Energy range	20 MeV - 300 GeV
Effective area at normal incidence	9,500 cm^2
Energy resolution (on-axis, equivalent Gaussian 1σ):	
100 MeV - 1 GeV	9%-15%
1 GeV - 10 GeV	8%-9%
10 GeV - 300 GeV	8.5%-18%
Angular resolution (on-axis, 68% containment radius):	
> 10 GeV	$\leq 0.15°$
1 GeV	$0.6°$
100 MeV	$3.5°$
Field of View (FoV)	2.4 sr
Timing accuracy	$< 10 \ \mu s$
Point source sensitivity	$3 \cdot 10^{-9}$ photons $cm^{-2} \ s^{-1}$

Since high-energy γ-rays cannot be reflected, one of the best ways to detect this radiation in the MeV-GeV energy range is through the process of pair conversion. The original γ-ray photon interacts with a layer of high-Z material, or converter, and is converted into an e^+e^- pair (this of course is only possible if the photon has an energy $E_{ph} \geq 2m_ec^2 \sim 1.022 MeV$). These secondary particles then travel with a kinetic energy given by $E_{ph} - 2m_ec^2$, and interact with a position-sensitive detector, or tracker, which records their position. A pair production telescope is made of a series of converter/tracker layers, through which the path of the charged particles produced by the original γ-ray photon is followed, and of a precision calorimeter which measures their energy. These data

allow us to reconstruct the arrival direction and energy of the original high-energy photon. A schematic representation of these concepts is given in Fig. 2.1.
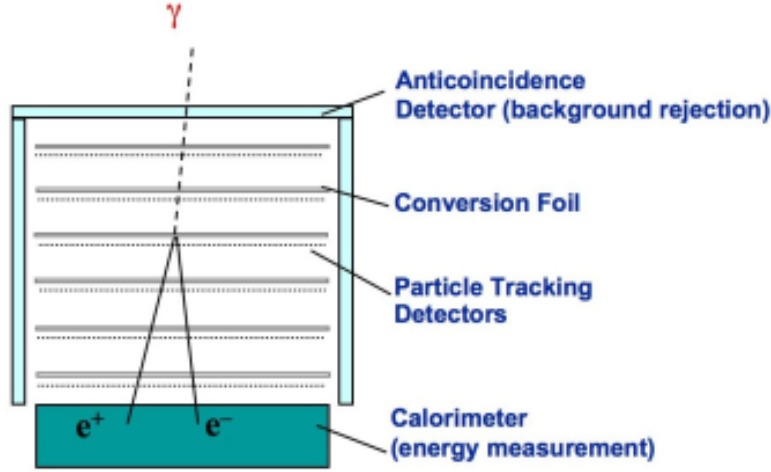

Figure 2.1: Schematic representation of the pair conversion, tracking, and energy measurement processes.

The LAT is a pair production telescope made of a 4x4 array of 16 converter/tracker modules. Each module is made of 16 tungsten converter planes, closely interleaved with trackers made of 2 (x, y) layers of position-sensitive silicon strip detectors, with two additional tracker layers at the bottom of each module (without converting material between them). At the bottom of each converter/tracker module there is a calorimeter made of 96 CsI(Tl) crystals, arranged horizontally in 8 layers of 12 crystals each. Each layer is aligned 90° with respect to its neighbor, forming a x, y array. This structure is surrounded by an anti-coincidence detector (ACD), that is a detector specifically designed to discriminate between photons of scientific interest and spurious events, e.g. cosmic ray particles. The ACD is made of 89 plastic scintillator tiles arranged in a 5x5 array on the top and 16 tiles on each of the 4 sides of the structure. A schematic representation of the LAT is illustrated in Fig. 2.2 [31].

2.3   The TeV range: *Imaging Atmospheric Cherenkov Technique*

Moving up into the TeV region of the electromagnetic spectrum, space telescopes such as *Fermi* become less effective in detecting radiation because their relatively
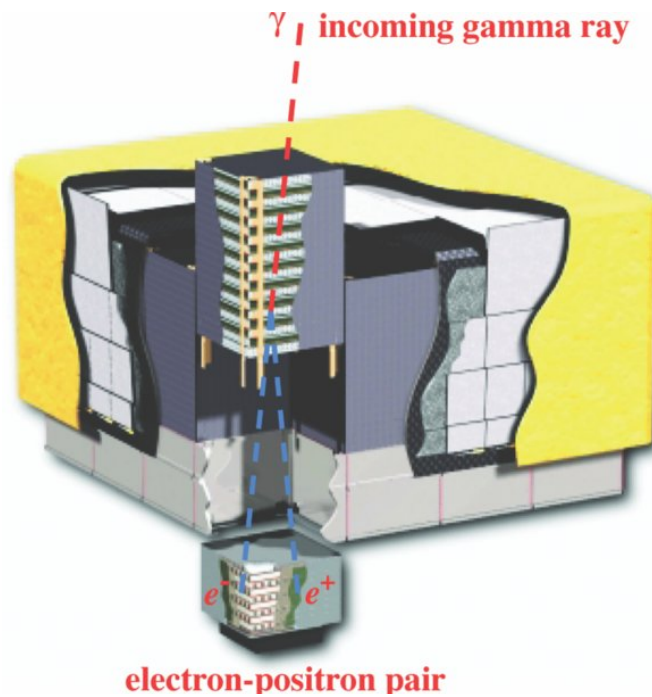
Figure 2.2: Schematic diagram of the *Large Area Telescope*, showing a single module of converter/tracker planes with the calorimeter at the bottom, the incident γ-ray photon and the path of the e^+e^- pair. Figure from Atwood et al. 2009 [31].

small collecting areas are insufficient to detect the few photons of such high energy which arrive to Earth. Therefore, to access the Very High-Energy (VHE, E>100 GeV) part of the spectrum, the *Imaging Atmospheric Cherenkov Technique* (*IACT*) was developed. The *IACT* consists in ground-based imaging of Cherenkov radiation produced when the VHE photons interact with the Earth's atmosphere.

2.3.1 The Cherenkov radiation mechanism and the *IACT*

When a charged particle moves through a dielectric medium with refraction index $n > 1$, this medium is polarized by the electric field of the particle. This disturbance relaxes back to equilibrium on a timescale given by the speed of light in that medium c/n. If, however, the charged particle travels with a velocity $v > c/n$, the disturbance in the dielectric medium remains in the wake of the trajectory of the particle, and the energy stored in it radiates away as the medium relaxes to equilibrium, in the form of a coherent shockwave. Such radiation, called Cherenkov radiation, is emitted in a cone of aperture $\cos\theta = 1/n\beta$ (where $\beta = v/c$), and falls primarily in the optical-UV part of the spectrum.

As a TeV photon strikes the Earth's atmosphere, it undergoes pair production. Since $E_{ph} \gg 2m_e c^2$, the e^+e^- pair produced carry a very high kinetic energy, and so emit high energy secondary photons by Brehmsstrahlung. These secondary photons undergo further pair production, and this process eventually leads to a cascade of charged relativistic particles, called *Extensive Air Shower* (EAS), at an altitude of 10-20 km. These charged relativistic particles generate very short pulsed (5-20 ns) Cherenkov radiation, which illuminates a total area on the ground (called "light pool") of the order of 10^4-10^5 m^2, and is detected by an array of mirrors, resulting in a total collecting area of hundreds of square meters, which is much larger with respect to any spacecraft and therefore allows for much better sensitivity. The concepts described above are illustrated in Fig. 2.3.

The typical Cherenkov telescope is a mirror segmented in small adjustable reflectors. The Cherenkov light is reflected by this mirror and focalized into a camera placed in the mirror's focus. This camera is made of an array of up to 1000 photo-multiplier tubes (PMTs), for a field of view (FoV) up to 5° in diameter.

The collected photons result in an image of the EAS, which typically has the shape of an elongated ellipse, with the long axis representing the vertical extension of the shower, and the short axis indicating the transverse one. However, the majority of the Cherenkov light collected is due to air showers produced by cosmic rays, which form a background that has to be subtracted if one wishes to study only the scientific VHE photons. This can be done by analyzing the shape and orientation of the image, because cosmic rays produce secondary particles with large transverse momenta, which themselves initiate various sub-showers, resulting in
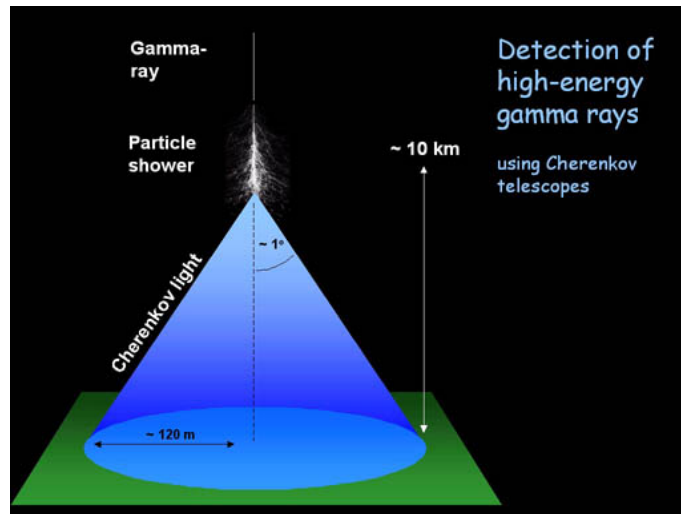
Figure 2.3: Schematic representation of the *Imaging Atmospheric Cherenkov Technique*. A Cherenkov cone with aperture $\theta = 1°$ produced at an altitude of 10 km results in a light pool of diameter $d \sim 175$ m.

a wider and less regular ellipse with respect to γ-ray primaries. Additionally, since cosmic ray particles are charged, they are deflected by the magnetic field of the ISM before they reach Earth, and so they originate showers whose Cherenkov elliptical images have no preferred orientation, whereas the showers produced by VHE photons from an astrophysical source do. These measurable differences in shape and orientation of the image provide a background discrimination system capable of rejecting up to 99,999% of the cosmic ray events, while retaining up to 50% of the scientific γ-ray photons [1].

Thanks to this image analysis and background rejection technique, it is possible to reconstruct the arrival direction of the primary photons and produce VHE γ-ray maps, with an angular resolution which depends on the photon energy, and is typically of the order of 0.1°.

Since the total Cherenkov photon yield is proportional to the energy of the primary particle, the image intensity, combined with the distance of the air shower's core from the telescopes, can be used to derive the energy of the original TeV photons. The energy resolution of this technique is also energy-dependent, and is typically of 15-20%.

There are three modern *IACT* based telescopes which are fully operational today: *H.E.S.S.* (2002), *MAGIC* (2004), and *VERITAS* (2007). The main per-

---

[1]This is only true for point-like sources like distant AGN, while the technique is less efficient in the case of spatially extended sources like SNR.

formance parameters of these telescopes are listed in Table 2.3. Additionally, construction of the *Cherenkov Telescope Array* is planned to begin in 2016.

2.3.2   The *H.E.S.S.* telescope

The *High Energy Stereoscopic System* is an array of Cherenkov telescopes located in Göllschau, Namibia, operated by a collaboration of researchers from various countries [2], the *H.E.S.S.* collaboration. Fig. 2.4 shows the *H.E.S.S.* array.

Figure 2.4: The *H.E.S.S. II* complete array.

In its initial design (*H.E.S.S. I*), the array was made of four 12 m mirrors arranged in form of a square with 120 m side length: this system went into operation in 2002. The mirrors are segmented in 382 round adjustable mirror facets of 60 cm size, with a total collecting area of 108 m^2 for each of the four mirrors. In 2012 a fifth 28 m mirror was added in the center of the array, made of 875 hexagonal adjustable facets of 90 cm size, for a total collecting area of 614 m^2. With the addition of the central mirror, the array was renamed *H.E.S.S. II*, having achieved increased energy coverage, sensitivity and angular resolution [3].

---

[2]Germany, France, United Kingdom, Namibia, South Africa, Ireland, Armenia, Poland, Australia, Austria, Sweden

[3]Data from the instrument's official website *www.mpi-hd.mpg.de/hfm/HESS/pages/about/telescopes/*

2.3.3 The *MAGIC* telescope

The *Major Atmospheric Gamma-ray Imaging Cherenkov Telescopes* is an array of two Cherenkov telescopes located in the Canary island of La Palma, Spain, operated by the *MAGIC* collaboration [4]. The *MAGIC* array is shown in Fig 2.5.

Figure 2.5: The *MAGIC* telescopes.

The first mirror, *MAGIC-I*, began operations in 2004. It is comprised of 50cm x 50cm Aluminum reflectors, for a total diameter of 17m and collecting area of 236 m^2. A second mirror with essentially the same characteristics (*MAGIC II*) was added in 2009 at a distance of 85 m from the first one, allowing a stereoscopic mode of observation with a factor of $\sim$3 increase in sensitivity [5] [55].

2.3.4 The *VERITAS* telescope

The *Very Energetic Radiation Imaging Telescope Array System* is an array of Cherenkov telescopes located at the *Fred Lawrence Whipple Observatory* in southern Arizona, USA, operated by a collaboration of several American universities, plus the universities of Leeds (UK) and Dublin (Ireland). A picture of the array is shown in Fig. 2.6.

The array consists of four 12m Cherenkov telescope based on the design of the *Whipple 10m Telescope*, and saw its first light in 2007. The mirrors are made of 350 identical hexagonal spherical mirrors of 0.322 m^2 area.

---

[4]The *MAGIC* collaboration includes universities and institutions from various countries, namely Germany, Spain, Italy, Switzerland, Croatia, Finland, Poland, Bulgaria and Armenia.

[5]Data from the instrument's official website *magic.mpp.mpg.de*

Figure 2.6: The *VERITAS* array.

Table 2.3: Main performance parameters for the *MAGIC*, *H.E.S.S.* and *VERITAS* Cherenkov telescopes. θ_R is the angular resolution, θ_{FoV} is the field of view, A_{eff} is the effective area (i.e. the geometrical surface of the telescope reduced by an efficiency factor, which depends on its physical parameters).

	MAGIC	*H.E.S.S.* (28 m)	*H.E.S.S.* (12 m)	*VERITAS*
θ_R	0.1°	0.067°	0.16°	0.1°
θ_{FoV}	3.6°	3.2°	5°	3.5°
A_{eff}	236 m^2	614 m^2	108 m^2	110 m^2
Energy range	50 GeV - 50 TeV	10 GeV - 10 TeV		100 GeV - 30 TeV

2.3.5 The *Cherenkov Telescope Array*

The *Cherenkov Telescope Array* (*CTA*) concept was first proposed in 2006, and includes today a consortium of over 160 institutions from 27 countries worldwide. The project is intended to build on the same *IACT* concepts proven by the facilities described above, with an order of magnitude increase in sensitivity and energy range, and significant improvements on angular and energetic resolutions. The *CTA* is meant to meet this ambitious goals through deployment of a large (50-100) number of different sized Cherenkov telescopes, located in two sites (southern and northern hemispheres), achieving full-sky coverage.

Specifically, the wide energy range performance goal, spanning four orders of magnitude, requires the development of different telescopes to cover three adjacent energy ranges:

- Low-energy range ($\leq$100 GeV): At this energies the main issue is the background rejection, which limits the achievable sensitivity even with a good coverage. Therefore this part of the array can cover a relatively small area ($\sim 10^4$ m^2), and this can be done with a small number (≤ 4) of large-sized telescopes (LSTs) with a mirror diameter of about 23m.

- Central energy range (0.1-10 TeV): In this range the optimal choice is an array of mid-sized telescopes (MSTs) with a mirror diameter of about 12m and a spacing of about 100m. Using a greater number of MSTs will improve the sampling across the Cherenkov light pool, both at small angles from the shower axis, where the light intensity is maximum, and at greater angles, to better reconstruct the arrival direction of the primary VHE photon.

- High-energy range (>10 TeV): The main issue here is the small number of VHE photons, so a large collection area is needed. This can be achieved using a large number of small-sized telescopes (SSTs) with a mirror diameter of a few meters and spacing matched to the size of the light pool (100-200 m).

The detailed design of these telescopes is based on the already proven technologies developed for the *H.E.S.S*, *MAGIC* and *VERITAS* telescopes. The *CTA* performance goals are listed in Table. 2.4 [10].

As for the timeline of the project, *CTA* is now in a preparatory phase, in which telescope prototypes are being built, with the goal of starting the five-year construction process in 2015, and being able to provide the first data (with a partial array) by 2016. One of the main steps that are yet to be made is the selection of the two *CTA* sites: current candidates include Argentina, Namibia and Chile for the southern site, and the Canary Islands, Arizona, Mexico, China and India for the northern site.

Table 2.4: Main *CTA* performance goals [10].

Energy range		$\sim$30 GeV to >100 TeV
Collection area (m^2)	at 1 TeV	$> 10^4$
	at 10 TeV	$> 10^6$ (S^a),$> 5 \cdot 10^5$ (N^b)
Energy resolution	at 50 GeV	$\leq 25\%$
	at >1 TeV	$\leq 10\%$
Angular resolution^c	at 0.1 TeV	$0.1°$
	at 1 TeV	$0.05°$
Field of View (FoV)	at 0.1 TeV	$5°$
	at 1 TeV	$8°$
	at >10 TeV	$10°$
Sensitivity (erg cm^{-2} s^{-1})	at 50 GeV	8×10^{-12}
	at 1 TeV	2×10^{-13}
	at 50 TeV	3×10^{-13} (S^a),10^{-12} (N^b)

^{a} Southern hemisphere site.
^{b} Northern hemisphere site.
^{c} 68% containment radius.

Chapter 3

The sample

Our sample contains the four known radio galaxies which have been detected both at MeV-GeV energies by *Fermi*-LAT and also at TeV energies by the current Cherenkov telescopes: NGC 1275, CenA, M 87 and IC 310.

3.1   NGC 1275

NGC 1275, also known as Perseus A, is the central dominant galaxy of the Perseus cluster. In addition to its central well-known AGN (fueled by the cluster cooling flow or by a recent merging event [54]), the main features of this system are the large-scale emission-line filaments projecting away from the galaxy al low velocity [119][110], and a high velocity emission-line component, which could be associated with a foreground late-type galaxy falling into the cluster, based on the presence of HI and X-ray absorption [48].

At radio wavelengths the source has been extensively monitored since the 1960, and is known as 3C 84. The radio source exhibits a core dominated morphology with asymmetrical jets [134], and has been classified as a FR I radio galaxy with a jet axis relatively close to the line of sight (the jet angle has been estimated in 30°-55° in the core region [30] [170]), and evidence of large scale jet bending [134]. The radio flux is variable: recent observation have reported an on-going rise in flux since 2005, and the ejection of a new subparsec scale component in 2007 which has continued to grow in flux as it travels away from the core. A radio image of 3C 84 is reported in Fig. 3.2.

In the IR, integral field spectroscopy and adaptive optics observations have allowed a detailed investigation of the circumnuclear material surrounding the SMBH. Scharwächter et al. 2013 [148] have found morphological and kinematical evidence for a 50 pc-scale molecular gas disc with a rotation axis coincident with the one of the radio jet, together with elonged perturbations with redshifted
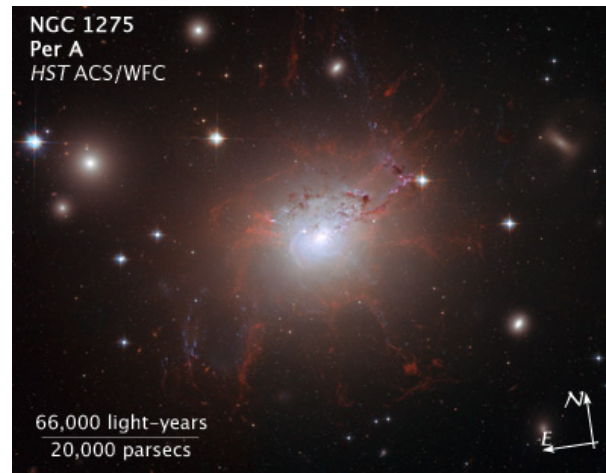
Figure 3.1: *Hubble Space Telescope* ACS/WFC view of NGC 1275. The scale bar reported in the bottom left corner corresponds to an angular size of 60". The image is about 4 arcminutes wide. The filters used are F435W (blue), F550M (green), F625W (red). Credit: NASA, ESA and the Hubble Heritage (STScI/AURA)-ESA/Hubble collaboration.
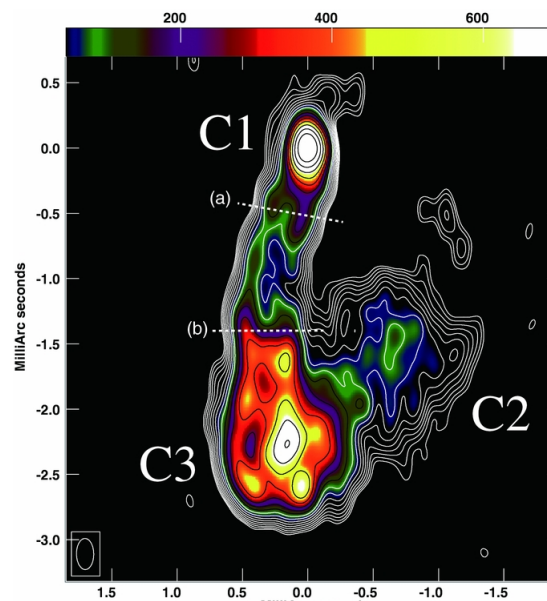

Figure 3.2: 43 GHz VLBA image of the nucleus of NGC 1275 from [121]. C1 is the core of the radio source, C3 is a bright jet knot, while the nature of the elongated structure C2 is unclear. The beam size is 0.24×0.13 milliarcsec.

velocities interpreted as gas streamers falling onto the central object. This could imply an unstable disc accretion mode for the central engine of NGC 1275.

In the X-rays, the emission of the cluster is dominated by the thermal contribution of the ICM cooling flow [63], but a non-thermal nuclear component with a hard power-law spectrum ($\Gamma = 1.6 \pm 0.1$) is also detected in the 0.5-10 keV range [34] and in hard X-rays above ~ 20 keV [16] with a spectrum consistent with the extrapolation of the AGN X-ray power-law.

At high-energy, a γ-ray excess in the direction of NGC 1275 was first detected with *COS B* [156], and interpreted as SSC emission from the center of the galaxy. This detection was not confirmed by *CGRO* [137], which provided a flux upper limit of $3.72 \cdot 10^{-8}$ photons cm^{-2} s^{-1}. NGC 1275 was then detected with high significance by *Fermi* after the first four months of all-sky survey [2], with a flux above 100 MeV seven times higher than the *CGRO* upper limit, suggesting strong variability. This variability has been confirmed by subsequent *Fermi* observations, with time scales as short as a week [97] [45].

In the VHE regime, NGC 1275 has recently been detected by *MAGIC* in stereoscopic mode [18]. The 70-500 GeV spectrum is much steeper than the *Fermi* MeV-GeV spectrum, strongly suggesting the presence of spectral curvature at a few tens of GeV. This was confirmed later by Aleksić et al. 2014 [19], who fitted the γ-ray Spectral Energy Distribution (SED) in the 0.1-650 GeV range using quasi-simultaneous *Fermi* and *MAGIC* data, and concluded that a power-law spectral shape is completely excluded. They also searched for multi-wavelength (MW) correlations between the optical, radio, GeV and TeV γ-ray bands in the period between October 2009 and February 2011, finding only a 4-5σ optical-GeV correlation, and a similar trend for the radio flux.

3.2   Centaurus A

Centaurus A (Cen A) is the nearest radio-loud AGN to Earth, and as such is one of the most studied objects of this class, with extensive monitoring throughout the electromagnetic spectrum.

Optically Cen A is one of the brightest known galaxies. It shows a distinctive prominent dust lane obscuring the galaxy's central region, which is thought to be the remnant of a previous merging event. This giant radio galaxy displays a variety of structures on scales ranging over a factor of 10^6. At large scale, its giant lobes extend on $\sim 10°$ in the sky, corresponding to a projected size of ~ 0.9 Mpc. Middle sized and inner lobes on the arcmin scales have been found, together with a highly collimated jet at arcsecond scale [46].

The X-ray emission from the central AGN is dominated by an arcsecond-scale core, whose spectrum can be fitted with a highly absorbed power-law, associated
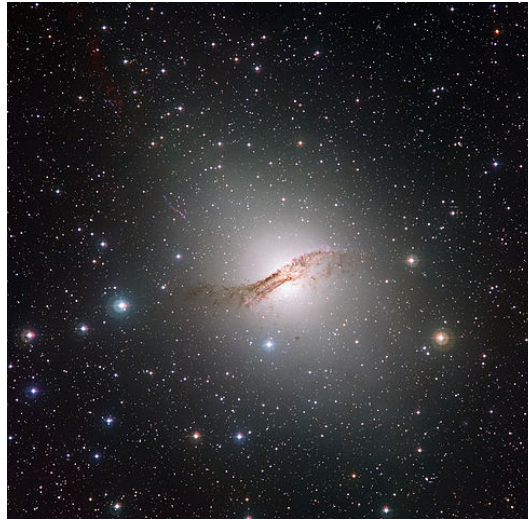
Figure 3.3: Optical image of Cen A taken with the Wide Field Imager of the MPG/ESO 2.2-metre telescope at the La Silla Observatory in Chile. The field of view is 33.87×33.12 arcminutes. The used filters are centered on B, V, R, and the Hα and [OIII] emission lines.
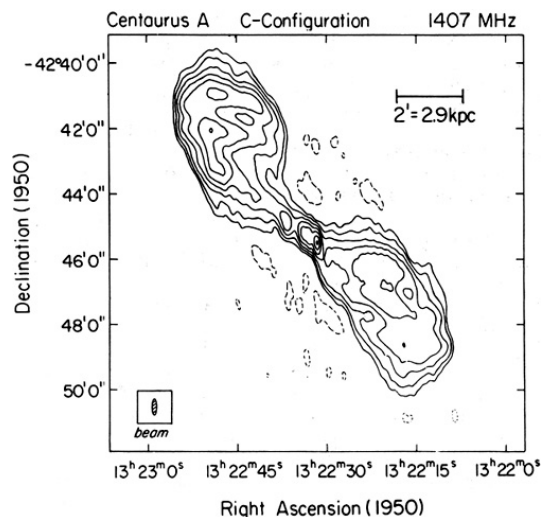

Figure 3.4: VLA image of the extended radio structure of Cen A at 1.4 GHz, from [46]. Beam size of $30.8'' \times 9.5''$.

with accretion onto the central black hole, and a second less absorbed power-law component associated with the subparsec VLBI jet [62].

In γ-rays, Cen A was first detected by *CGRO* [154]. High energy emission from the core of the galaxy was later confirmed by *Fermi* [4]. Quite interestingly, shortly after *Fermi* detected significant γ-ray emission from the diffuse radio lobes as well, challenging the current emission models insofar it implies the presence of high energy electrons at a large distance from the central engine. It is unclear whether such electrons are accelerated in situ or efficiently transported from the base of the jet, nor how common is this kind of diffuse γ-ray emission from radio-galaxies.

Cen A has also been detected at VHE by *H.E.S.S.* [14] with a very low flux. A simple power-law spectral fit yielded a photon index of $\Gamma = 2.7 \pm 0.5$, and no significant flux variability was detected (possibly due to the low flux).

3.3   M 87

Due to its vicinity, M 87 is one of the most extensively studied extragalactic objects. It is a giant radio galaxy at the center of the Virgo cluster, best known for its prominent kpc-scale jet, well imaged at radio through X-ray frequencies over the decades [153] [111].

Classified as a FR I at radio wavelengths, the source has a compact (hundreds of Schwarzschild radii) and variable core, while the inner jet is segmented into superluminal "knots". The jet is very well-collimated at 100pc-scale [42], but VLBI observations show that its opening angle continually increases approaching the core [95]: this may be a signature of the launching structure of the still uncollimated jet. The jet launching structure has been imaged at angular resolution down to tens of μarcsec with mm-VLBI, and the estimated core size is $5.5 \pm 0.4R_S$. If this component is identified with the central black hole site, then its size corresponds to a prograde ISCO (Innermost Stable Circular Orbit) for a spin parameter $a > 0.2$ [56].

In the X-rays, high-resolution imaging of the AGN shows an unresolved core and a knotted jet structure consistent with the optical one. The core has an X-ray spectrum with a steep photon index, suggesting a synchrotron jet origin for the emission, rather than an association with the accretion flow. This hypothesis is also supported by the observed core flux, which is larger than expected from an advective accretion flow [111].

In γ-rays, M 87 was detected by *Fermi* during the first ten months of the mission [3]. A simple power-law spectral fit yielded a flux of $F_{>100MeV} = (2.45 \pm 0.63)\cdot10^{-8}$ photons cm^{-2} s^{-1} and a photon index of $\Gamma = 2.26\pm0.13$. No significant evidence for temporal variability was found.
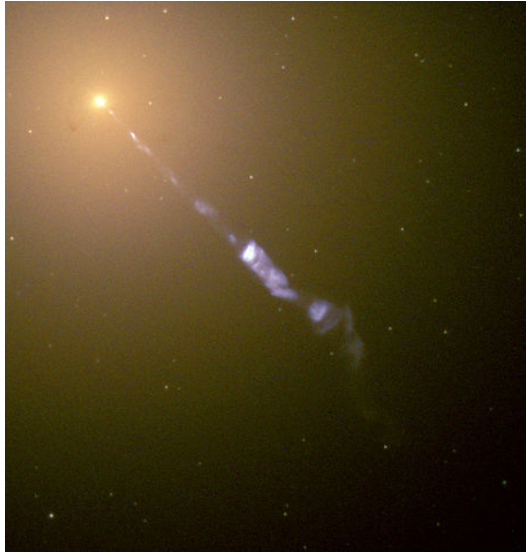
Figure 3.5: *Hubble Space Telescope* WFPC2 view of M 87 and its exceptionally bright jet. The image is 31 arcsec wide. The filters used are F814W (red), F606W (green), F450W (blue), F300W (violet). Credit: NASA and The Hubble Heritage Team (STScI/AURA).

Emission by M 87 at VHE was firmly established by the *H.E.S.S.* collaboration [13], which reported a hard TeV spectrum ($\Gamma = 2.2$), and evidence of flux doubling variability on time scales of days. This variability strongly constrains the size of the emitting region, and together with spectral modeling leads to favor the radio core as the most likely origin of VHE γ-rays.

3.4   IC 310

IC 310 is located at the outskirts of the Perseus galaxy cluster, at an angular distance of $\sim 0.6°$ from the central galaxy, NGC 1275 (see Section 3.1).

Based on its radio morphology, IC 310 was originally classified as a head-tail radio galaxy, that is a galaxy whose gas is stripped by the ram pressure as it moves in the ICM [142] [118] [151]. The tail is apparently single-armed, and it extends for $\sim 15'$ in the direction connecting the center of the cluster to the galaxy. Because of its lack of strong emission lines, its radio and X-ray spectral indices, and its point-like X-ray appearance (coincident with the radio core), it has been argued that IC 310 hosts a low-luminosity BL Lac, and represent a transition source between blazars and misaligned AGN [136] [143]. Recently the
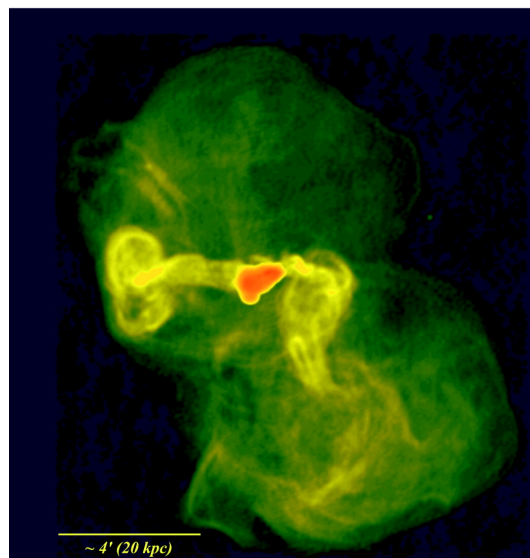
Figure 3.6: VLA 90cm image of the extended radio structure of M 87, from [130]. The beam size is 7.8" x 6.2". The scale bar in the bottom left of the image corresponds to 4 arcminutes.

head-tail classification has been challenged by Kadler et al. (2012) [96], with a detailed investigation of the source radio structure using VLBA observations. They reported the detection of a pc-scale core-jet structure inside the "head", which is aligned with the direction of the "tail", thus disproving the presence of jet bending (see Fig. 3.7). Moreover, the fact that no counter-jet is observed implies strong Doppler-boosting, and thus a blazar-like emission for IC 310. IC 310 has
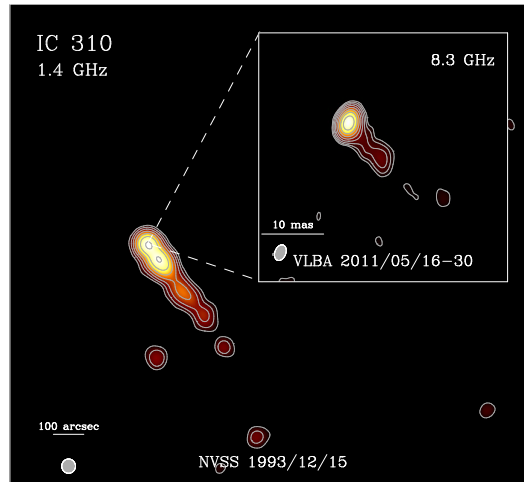

Figure 3.7: Fig. 2 from Kadler et al. 2012 [96]. The image shows the jet of IC 310 at large scale (large field, VLA 1.4 GHz) and small scale (inset field, VLBA 8.4 GHz). The one-sidedness of the jet is clear, suggesting a blazar-like structure for IC 310.

been detected by *Fermi* above 100 GeV with a 4.5σ significance. At energies 1-100 GeV the emission is dominated by NGC 1275, while IC 310 emerges clearly only in the highest energy range (see Fig.1 in Neronov et al. 2010 [123]).

In the TeV range IC 310 has been detected by *MAGIC* [20] with a significance of 8.6σ. The 150 GeV - 7 TeV spectral fit reveals a flat spectrum ($\Gamma = 2.00 \pm 0.14$) with no sign of curvature. Temporal variability is established with a 3-3.5σ significance: this strongly indicates the core of the galaxy as the source of the VHE photons, while the hypothesis that the emission is produced in the bow shock of the tail is disfavored, since in this case the flux would be stable on time scales of $\sim 10^3$ yr.

Very recently the *MAGIC* collaboration [21] has reported an extraordinary outburst at TeV energies from IC 310 on $12^{th}/13^{th}$ November 2012, during which the flux rose up to a factor of four higher with respect to the previous detection. Additionally, extreme variability with a flux doubling time scale as short as 4.8 minutes was detected. This is shorter than the SMBH event horizon crossing

time, and it poses a serious challenge to current emission models which try to reproduce these observed properties. According to the authors such fast variability may be explained in the framework of so-called "magnetospheric" models. These models are usually applied to pulsars, but could also operate in the magnetosphere of a SMBH. This theory suggests that particles are accelerated in vacuum gaps in a rotating magnetosphere, where the density of charge carriers is too low to balance the electric field, which can thus become non-zero and efficiently accelerate particles up to very high energies. Such a depletion of charges can occur when the accretion rate is very low, and the SMBH has been spun up to maximum rotation by the accretion process.

Chapter 4

Fermi data analysis and results

In this Chapter we report the methods used for the analysis of *Fermi*-LAT data on the four TeV detected radio galaxies described above (Section 4.1), and present the results of our spectral (Section 4.2.1) and temporal analysis (Section 4.2.2). Finally, we present and discuss the comprehensive MeV-TeV spectra for these sources (Section 4.2.3).

4.1 Data analysis

The astrophysical analysis of LAT data consists in fitting models to the data through the likelihood method: this is necessary because of the instrument's energy-dependent and geometry-dependent parameters, the complex nature of the γ-ray background, and the fact that *Fermi* operates in survey mode for $\sim 90\%$ of the time.

4.1.1 The *Region Of Interest* and the model

Given a field of view centered on the source under investigation, due to the large LAT PSF (see Table 2.2) counts from sources in a region around the center will fall in the PSF associated with the target source. One must therefore model the contribution from all sources inside a so called *Region Of Interest* (ROI), which must be several times the characteristic PSF size (e.g. 0.6° at 1 GeV), i.e. typically $\sim 10°$. Additionally, sources from a larger *Source Region* are included in the model, but are not fitted. This region is centered on the ROI with a radius larger by several PSF length scales.

As mentioned above, the statistical analysis consists in fitting a model to the data. This model must describe as accurately as possible the γ-ray emission from the ROI and the Source Region, which is given by the target source plus a number

of extragalactic point sources, an isotropic γ-ray background, and a Galactic diffuse component. The model contains coordinates and spectral informations for all components, which are usually taken from the *Fermi* catalogs. As for the target source, one must choose the spectral form of the model that will be fit to the data to derive the best fit parameters. Common choices are:

- Power Law

$$N(E) = N_0 \left(\frac{E}{E_0} \right)^{\gamma}$$

- Broken Power Law

$$N(E) = \begin{cases} N_0 \left(\frac{E}{E_b} \right)^{\gamma_1} & \text{for } E < E_b, \\ N_0 \left(\frac{E}{E_b} \right)^{\gamma_2} & \text{for } E > E_b. \end{cases}$$

- LogParabola

$$N(E) = N_0 \left(\frac{E}{E_0} \right)^{\left[\alpha + \beta ln(\frac{E}{E_0}) \right]}$$

- Power Law with exponential cutoff

$$N(E) = N_0 \left(\frac{E}{E_0} \right)^{\gamma} e^{-E/E_c}$$

The parameters above are the normalization N_0, calculated at the pivot energy E_0, the spectral index γ (or α for the Logparabola), the break energy E_b, the curvature parameter β, and the cutoff energy E_c.

4.1.2   The likelihood and the Test Statistic

The likelihood statistic L is the probability of obtaining the observed data, given an input model.

If the data counts are binned, the likelihood is defined as the product of the probabilities of observing the detected counts in each bin. These probabilities, due to the small number of counts per bin, are given by the Poisson distribution

$$p_i = e^{-m_i} \frac{m_i^{n_i}}{n_i!} \tag{4.1}$$

This is the probability of detecting n_i counts in the i-th bin, where m_i is the predicted number of counts, which depends on the model. The product of these probabilities is the likelihood

$$L = e^{-N_{exp}} \Pi_i \frac{m_i^{n_i}}{n_i!} \tag{4.2}$$

where $e^{-N_{exp}}$ is the product of e^{-m_i} for all i, and $N_{exp} = \Sigma_i m_i$ is the total expected number of counts predicted by the model. This definition is the basis of the binned likelihood analysis, and implies a certain tradeoff between a smaller bin size (to give a better representation of the source) and an acceptable number of counts per bin (to obtain a statistically reliable fit).

When the bin size becomes infinitesimally small, so that n_i can only be 1 or 0, the likelihood becomes

$$L = e^{-N_{exp}}\Pi_i m_i \tag{4.3}$$

where i is now the index over the counts. This definition is used in the unbinned likelihood analysis, which is more accurate since the counts are taken into account individually and not averaged over a bin, but is more computationally expensive, especially in the case of a large number of counts.

The detection significance for a source is given by the Test Statistic, defined as [115]

$$TS = 2ln\frac{L_{max,1}}{L_{max,0}} \tag{4.4}$$

where $L_{max,1}$ is the maximum likelihood value for a model with the source at its specific location, and $L_{max,0}$ is the maximum likelihood value for a model without the source. For an increasingly large number of counts, asymptotically the TS has the same distribution of the χ^2, and therefore, as a rule of thumb, the square root of the TS is taken as the detection significance for a given source. This implies that a source can be considered detected if $TS \geq 10$, otherwise a 90% confidence level upper limit is placed.

4.1.3   Data reduction steps

We will now give a brief overview of how the likelihood analysis is carried out in practice, through the science analysis tools provided by the *Fermi* collaboration.

The raw data are available for download at the online database of the *Fermi Science Support Center*, in the form of an FT1 file, or event file, which contains the actual counts, and an FT2 file, or spacecraft file, which contains information about the status and position of the *Fermi* spacecraft and the orientation of the LAT during the selected time interval.

After downloading these fits files, by providing the desired coordinates and time range, we need to apply some cuts based on the desired ROI and time range. This is done using the *gtselect* tool, by indicating the coordinates for the ROI, its radius, and the desired time range. Other standard cuts which are usually applied include a zenith angle cut to avoid emission from the Earth's limb, a

selection of the event class[1], a ROI based time cut to exclude times when the ROI falls outside the LAT's field of view, and a rocking angle cut.

Analysis of *Fermi* data usually implies that the likelihood is calculated many times. Some quantities needed for the likelihood computation can be however calculated only once before the actual likelihood fitting, thus greatly speeding up the repeated computation process. One of these pre-computed quantities is the exposure time, i.e. the time when the LAT is effectively acquiring data (also called "livetime"). This depends on the pointing history of the instrument and the source coordinates, because the instrumental response in turn depends on the off-axis angle, which varies during the observation. This means that the actual count number depends on how much time the instrument spends with a certain inclination angle during the selected time range. The livetime is calculated with the *gtltcube* tool, using the pointing history of the telescope, provided by the spacecraft file, and the GTIs [2]. The output of this operation is a so called *livetime cube*, which is a map of the exposure time on a 3D grid given by the two coordinates and the off-axis angle.

Another precomputed quantity is the exposure map, which represents the predicted number of counts in the ROI for a given model. This is obtained integrating the instrumental response over the ROI, assuming a spatial and energetic binning, and requires the livetime cube as an input. The exposure map is calculated with the *gtexpmap* tool for unbinned likelihood analysis and with the *gtexpcube2* tool for binned likelihood analysis.

The next step is to use the *gtdiffrsp* tool to calculate the contribution to the likelihood probability given by the diffuse sources included in the model. This operation is necessary to speed up the likelihood computation time, since the integral which gives the contribution of these diffuse sources to the likelihood is much more complicated than the one for point sources (which have a simple delta-function spatial component), and so it is useful to compute these integrals in advance.

For binned likelihood analysis, the spatial and energetic binning is done using the *gtbin* tool. The output of this operation is a 3D counts cube, where the three dimensions are given by the two coordinates plus energy.

Once all these quantities have been computed, it is possible to proceed with the actual likelihood fitting: this is done using the *gtlike* tool. This operation will provide the detection significance (TS) for each source in the model as well as the parameter values obtained in the fitting process.

---

[1]The most common event classes are SOURCE and CLEAN. The former is used for point sources, the latter for diffuse or high energy sources, as it provides a substantial reduction in the cosmic ray background above 10 GeV.

[2]The *Good Time Intervals*, or GTIs, are the time ranges when the data can be considered of good quality.

4.2 Results: MAGN detected in the TeV band

4.2.1 Average spectra

We now turn to describe the results of our analysis of six years of *Fermi*-LAT data for the four sources in our sample. Fig. 4.1 displays the count maps for NGC 1275, Cen A and M 87. The sources of interest are clearly visible at the center of the field of view. In the map of NGC 1275 (left panel) the diffuse structure represents emission from the Galactic plane. In the case of Cen A (central panel) it is possible to see the diffuse component which has been attributed to the lobe (see Section 3.2). In the map of M 87 (right panel) it is possible to identify two additional sources which are present in the 3FGL catalog, and which have been included in our model. Finally, IC 310 is located at 0.6° from NGC 1275, therefore it is included in the map in the left panel of Fig. 4.1 but it is not visible because of the brightness and proximity of NGC 1275 (especially at low energies). As mentioned in Section 3.4, IC 310 becomes the dominant source in the field only in the highest energy range. This can be seen in Fig. 4.2, which includes count maps of the central region of the Perseus cluster in the energy range 1-10 GeV (left panel), 10-100 GeV (central panel) and 100-300 GeV (right panel) respectively. As expected, IC 310 is clearly visible and dominant only in the last map.
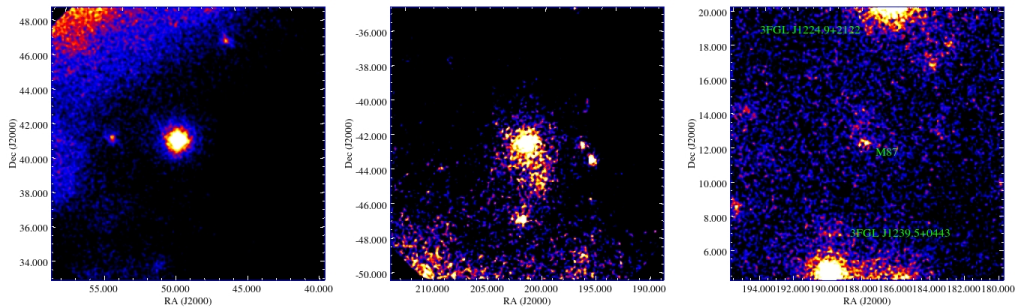

Figure 4.1: Count maps for (left to right) NGC 1275, Cen A and M 87. The image size is $16° \times 16°$, the resolution 0.04°/pixel.

As a first step of our analysis, we performed a likelihood analysis across the entire time range and energy range, in order to assess the average spectral properties of the sources. Then we repeated the analysis in different energy bins to produce a spectrum for our sources. The resulting spectra are shown in Fig. 4.3. Our results are in good agreement with those reported in the most recent *Fermi* AGN catalog, the 3LAC [11], except for IC 310. Since this is a peculiar source,
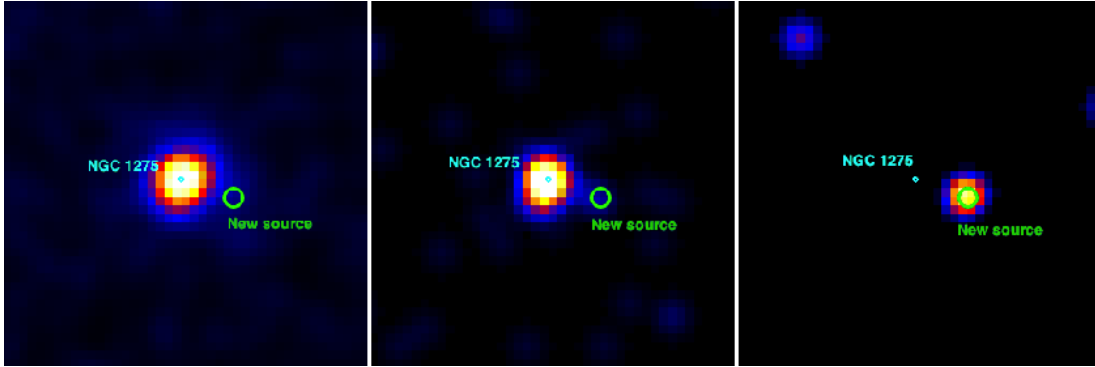
Figure 4.2: Fig. 1 from Neronov et al. 2010 [123]. Count maps centered of the central region of the Perseus cluster in the energy range 1-10 GeV (left panel), 10-100 GeV (central panel) and 100-300 GeV (right panel) respectively. The label "new source" refers to IC 310.

it requires a dedicated analysis (as explained below), and therefore a standard catalog analysis is unlikely to give reliable results.

The model adopted here includes all sources within a 10° ROI centered on the target source, plus a 5° source region. We applied standard cuts based on the zenith angle ($z < 100°$) and the rocking angle ($\theta < 52°$) in order to limit the contamination from γ-rays produced by cosmic-ray interactions in the upper atmosphere. The data files were obtained from the *Fermi Science Support Center*[3], and include all events between MET[4] 239557418 and 428859820 (2008-08-04 at 15:43:37 UTC and 2014-08-04 at 15:43:37 UTC, respectively) in the energy range 0.1-100 GeV. All reported errors are at the 1σ statistical level. The values of the spectral parameters reported below are the results of the likelihood analysis performed over the whole time range and energy range. The results of this analysis are summarized in Table 4.1.

NGC 1275

Our analysis results in the detection of NGC 1275 with a Test Statistics $TS = 38125$, corresponding to a significance of $\sigma \sim 195$. The spectrum is best fitted by a logparabola (see Section 4.1 for a definition of this analytical form) with parameters $N_0 = (2.88 \pm 0.04) \cdot 10^{-11}$ MeV^{-1} cm^{-2} s^{-1}, $\alpha = 2.02 \pm 0.02$, $\beta = 0.07 \pm 0.01$ and $E_B = 1$ GeV (fixed value). The integrated 0.1-100 GeV flux is $(2.64 \pm 0.05) \cdot 10^{-7}$ photons cm^{-2} s^{-1} or $(1.46 \pm 0.02) \cdot 10^{-4}$ MeV cm^{-2} s^{-1}. NGC 1275 is the only source among the LAT radio galaxies to have a spectrum

---

[3]URL: http://fermi.gsfc.nasa.gov/ssc/
[4]*Mission Elapsed Time*, seconds since 2001.0 UTC.

different than a power-law.

Centaurus A

Our analysis results in the detection of Cen A with a Test Statistics $TS = 4096$, corresponding to a significance of $\sigma \sim 64$. The spectrum can be fitted by a power-law with a normalization of $N_0 = (6.77 \pm 0.03) \cdot 10^{-11}$ MeV^{-1} cm^{-2} s^{-1} and a photon index $\Gamma = 2.737 \pm 0.006$, while the pivot energy was fixed to the 2FGL value of $E_0 = 402$ MeV. The integrated 0.1-100 GeV flux is $(1.76 \pm 0.05) \cdot 10^{-7}$ photons cm^{-2} s^{-1} or $(4.09 \pm 0.09) \cdot 10^{-5}$ MeV cm^{-2} s^{-1}. These values are in good agreement with those reported by the *Fermi* collaboration [4]. The peculiar spectral behavior at the highest energies is also confirmed [4], with a hardening of the spectrum in the last energy bins. This spectral feature is discussed in detail in Section 4.2.3, together with the VHE data.

M 87

Our analysis results in the detection of M 87 with a Test Statistics $TS = 685$, corresponding to a significance of $\sigma \sim 26$. The spectrum can be fitted by a power-law with a normalization of $N_0 = (1.7 \pm 0.1) \cdot 10^{-12}$ MeV^{-1} cm^{-2} s^{-1} and a photon index $\Gamma = 2.15 \pm 0.05$, while the pivot energy was fixed to the 2FGL value of $E_0 = 1$ GeV. The integrated 0.1-100 GeV flux is $(2.1 \pm 0.1) \cdot 10^{-8}$ photons cm^{-2} s^{-1} or $(1.15 \pm 0.07) \cdot 10^{-5}$ MeV cm^{-2} s^{-1}.

IC 310

The analysis of *Fermi*-LAT data from IC 310 is particularly challenging, due to the proximity and brightness of NGC 1275, and to the unusually hard spectral behavior of IC 310. A visual inspection of *Fermi* maps of these sources reveals that NGC 1275 dominates the γ-ray emission in the range 1-100 GeV, while emission from IC 310 emerges only in the highest LAT energy bins (see Fig. 4.2).

For this reason, the standard LAT data analysis described above fails to provide a good fit to the data from IC 310. Therefore, we have followed the data analysis used by the *Fermi* collaboration to produce the first *Fermi*-LAT catalog of sources above 10 GeV (1FHL, Ackermann et al. 2013 [12]). With respect to the standard analysis technique, we have restricted our analysis to the 10-300 GeV energy range and used the event class CLEAN. CLEAN class reduces the particle background substantially at the expense of a smaller effective area. It is appropriate for use in analyses which benefit from lower background contamination, as is the case at the highest energies within reach of the LAT. The model used in the likelihood analysis was derived from the 1FHL catalog, instead of the 2FGL catalog, given our higher energy range. Apart from these modifications, we have applied the same parameters and cuts (ROIs, rocking angle, zenith angle) used to analyze the other sources in the sample.

Table 4.1: Results of our analysis of six years of *Fermi* data. The table reports the Test Statistic, the integrated flux, the spectral index and curvature parameter (in the case of a Logparabola fit), and the variability time scale.

Source	TS	Flux[a]	Γ (α)	β	ΔT_{var}
NGC 1275	38125	26.4±0.5	2.02±0.02	0.07±0.01	1 week
Cen A	4096	17.6±0.5	2.737±0.006	*	*
M 87	685	2.1±0.1	2.15±0.05	*	*
IC 310[b]	41	0.004±0.002	1.2±0.5	*	*

[a] Flux between 0.1-100 GeV. Units of 10^{-8} photons cm^{-2} s^{-1}.
[b] In this case the flux is integrated between 10-300 Gev.

Our analysis results in the detection of IC 310 above 10 GeV, with a Test Statistics $TS = 41$, corresponding to a significance of $\sigma \sim 6.4$. The spectrum is best fitted by a power-law with a normalization of $N_0 = (1.8 \pm 0.8) \cdot 10^{-16}$ MeV^{-1} cm^{-2} s^{-1} and a photon index of $\Gamma = 1.2 \pm 0.5$, while the pivot energy was fixed at the 2FGL value $E_0 = 64$ GeV. The integrated 10-300 GeV flux is $(4 \pm 2) \cdot 10^{-11}$ photons cm^{-2} s^{-1} or $(3.2 \pm 1.5) \cdot 10^{-6}$ MeV cm^{-2} s^{-1}. The spectral parameters obtained are consistent with those reported in a recent multi-wavelength study by the Aleksić et al. 2014 [23].

4.2.2   Timing analysis

We have produced light curves for the sources in our sample by performing the same standard likelihood analysis described above in different temporal bins, keeping the spectral index fixed in order to better constrain the flux variations. We performed multiple analyses with different bin sizes, using the smallest size which allowed the fitting process to converge successfully. We found no statistically significant variability for Cen A, M 87 and IC 310. The light curves of Cen A and M 87 are presented in Fig. 4.4, while the low statistic of the data from IC 310 prevented a successful likelihood analysis in different temporal bins.

It is interesting to note that M 87 and IC 310 were observed to vary in the TeV band. M 87 underwent several flares in recent years [13] [8] [7] [86] [39], with variations of a factor ~ 5 in time scales of days. As shown in Fig. 4.4 (bottom panel), these TeV flares do not have a clear counterpart in the *Fermi* band.

As for IC 310, very recently the *MAGIC* telescope detected extremely fast variability on time scales down to 4.8 minutes, with flux variations of a factor of ~ 5 [21]. This is the shortest variability time scale ever observed in a non-blazar AGN, and is similar to the fastest flares observed in BL Lac blazars, which reach
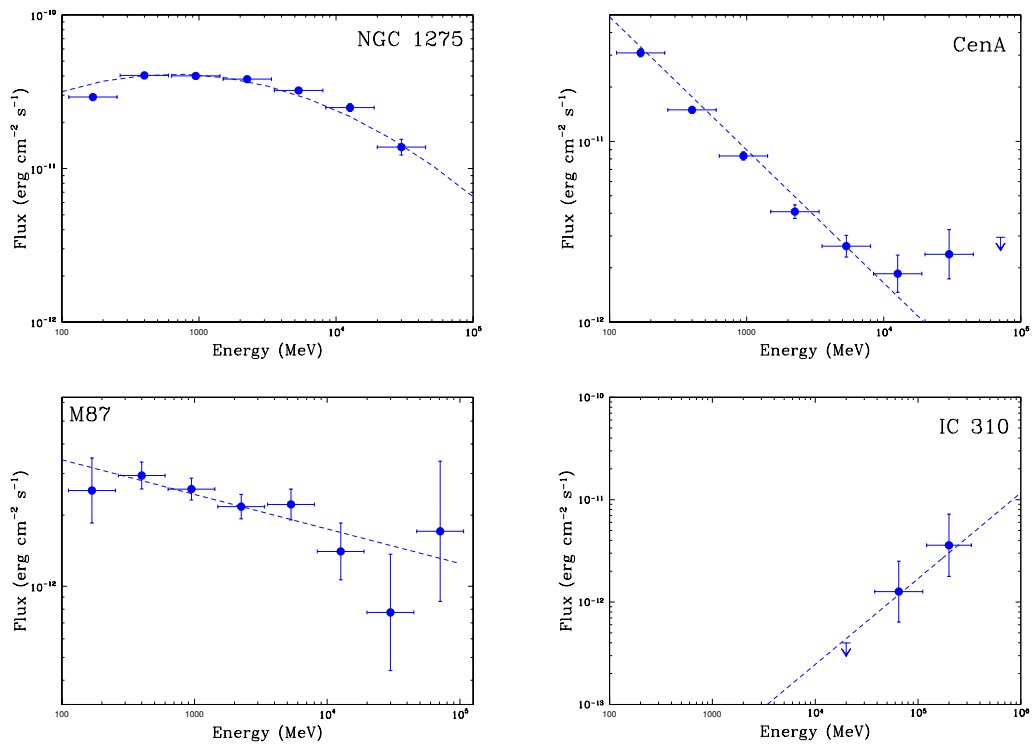
Figure 4.3: *Left to right, up to down*: average LAT spectra for NGC 1275, CenA, M 87 and IC 310. Blue points are LAT spectral points, while the blue dotted line represents the fit which result from the analysis over the whole energy range.

down to ∼2 minutes (e.g. Mrk 501 [17] and PKS 2155-304 [15]). This reinforces the hypothesis that IC 310 is a transitional object between the FR I and BL Lac classes.

Statistically significant flux variability is detected only in the case of NGC 1275, down to a bin size as small as $\Delta t =1$ week. Fitting a constant to the data results in a reduced chi-squared of $\chi^2_\nu = 5.6$, corresponding to a probability $P_{cons} \ll 10^{-3}$ for the source to have a constant flux. This variability can be used to estimate the size of the γ-ray emission region. We refer to Chapter 6 for a detailed discussion on this point.

By repeating the analysis on NGC 1275 with both the spectral index and normalization as a free parameters, we have also detected significant spectral variability on time scales $\Delta t = 3$ weeks. Fitting a constant to the flux light curve yields a reduced chi-squared of $\chi^2_\nu = 6.5$, corresponding to a probability $P_{cons} \ll 10^{-3}$ for the flux to be constant. The same fitting for the spectral index light curve results in a reduced chi-squared of $\chi^2_\nu = 2.4$, again corresponding to a probability $P_{cons} \ll 10^{-3}$ for the spectral index to be constant. We observe a significant anti-correlation between flux and spectral index, which is displayed in Fig 4.5. A linear fit results in a correlation coefficient $r = -0.55$, with the parameterization reported in the caption of the plot, corresponding to a chance probability for the correlation $p \ll 10^{-3}$. This harder-when-brighter behavior is common among blazars [6]. The most common interpretation is that when a source undergoes a flare, fresh energetic particles are injected. This causes a hardening of the particle energy distribution, which in turn leads to a flatter observed spectrum.

4.2.3   GeV-TeV spectra

The GeV-TeV connection in AGN is not trivial, because the data are usually not contemporaneous, and the two energy bands show different temporal behavior (see previous Section). By "contemporaneous" data we indicate TeV data obtained at a time when *Fermi*-LAT was operational. Larger spectral coverage and contemporaneity of GeV-TeV data (since the sources can be variable, see previous Section) is crucial for a complete understanding of the γ-ray behavior of AGN. In this respect the synergy between *Fermi* and the CTA will be the perfect tool, providing contemporaneous spectral coverage over six orders of magnitude in energy, from 100 MeV to 100 TeV. With the addition of a new instrument in the 0.1-100 MeV range, like for example the Astrogam mission [5], two additional orders of magnitude would be available, providing an exceptionally detailed view of the high-energy band.

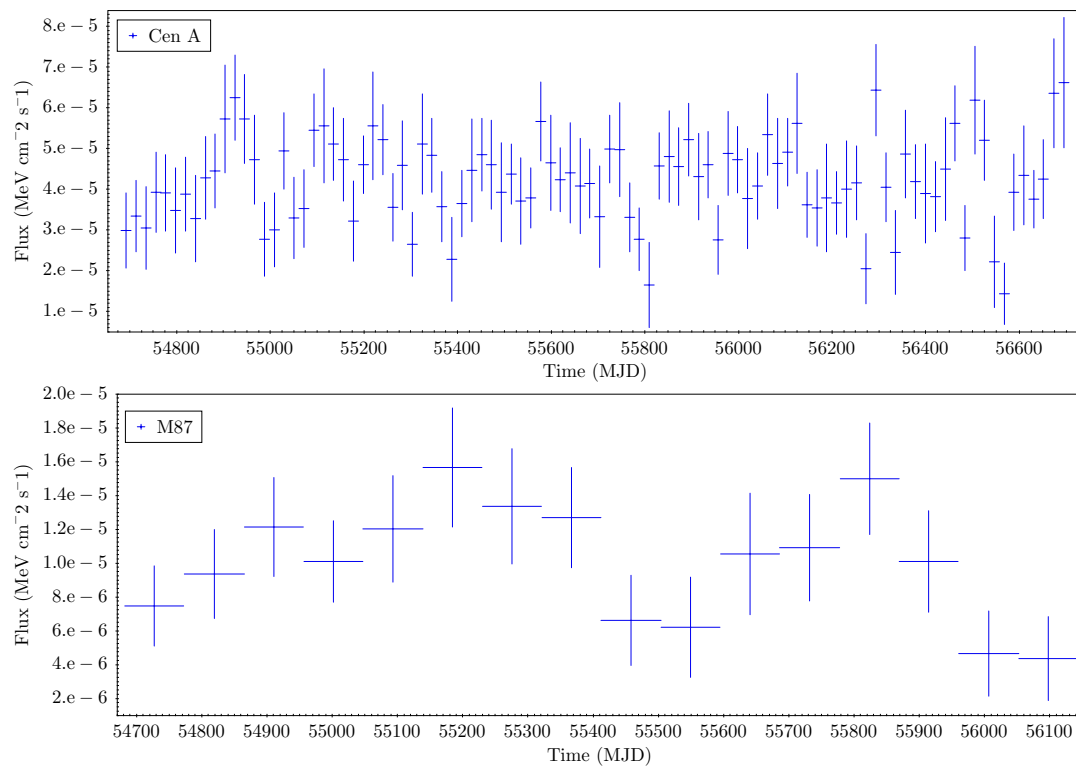[5]Web site astrogam.iaps.inaf.it.

Figure 4.4: *From the top down*: light curves of NGC 1275, CenA and M 87. Bin size of 1 week, 3 weeks and 3 months, respectively. Energy range 0.1-100 GeV.
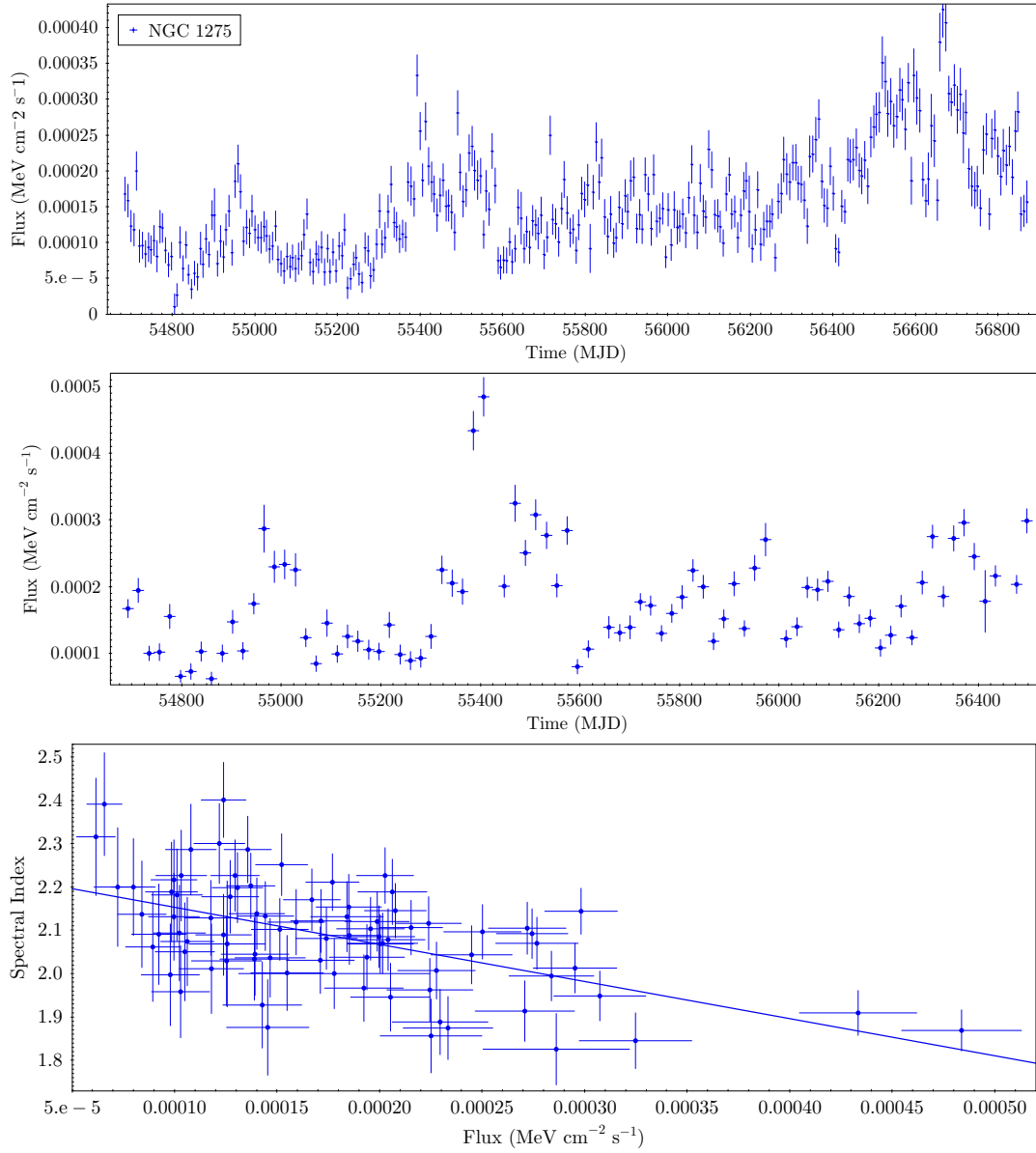
Figure 4.5: *Top panel*: Six-year light curve of NGC 1275 with time bins of 1 week. *Central panel*: Five-year light curve of NGC 1275 with time bins of 3 weeks (central panel) and *Bottom panel*: corresponding plot of the spectral index versus flux. The linear fit, indicated by the thick blue line, gives $\Gamma = 2.24 - 0.857(F)$, with a correlation coefficient $r = -0.49$. The correlation is highly significant, with a p-value $p < 10^{-4}$.

While dealing with currently available GeV-TeV data, however, one must be aware of the caveats mentioned above. In our case, we were able to collect contemporaneous data only for NGC 1275, whose spectrum is therefore the most reliable in our sample.

NGC 1275

As mentioned in section 3.1, NGC 1275 has been observed at TeV energies by *MAGIC* during two observational campaigns, from October 2009 to February 2010 and from August 2010 to February 2011, respectively. Since *Fermi* was already operational at that time, it has been possible to construct a comprehensive and contemporaneous γ-ray spectrum of NGC 1275 from 100 MeV up to about 500 GeV. This spectrum is shown for the first *MAGIC* campaign [6] in Fig.4.6. The best fit ($\chi^2 = 1.787, \nu = 7$) of the combined data set is a power-law with index $\Gamma = 2.05^{+0.08}_{-0.08}$ and exponential cutoff at $E_{cut} = 110^{+70}_{-40}$ GeV. Since NGC 1275 is the only source for which we have contemporaneous GeV and TeV data, this object is the one with the most reliable comprehensive γ-ray spectrum.

Centaurus A

As mentioned in Section 3.2, Cen A has been detected in the VHE energy range by the *H.E.S.S.* telescope [13]. The data were taken between 2004 April and 2008 July, with a total live time of 115 hours. A comprehensive γ-ray spectrum including both LAT and *H.E.S.S.* data points is shown in Fig. 4.7. It should be noted that the LAT and the VHE data are not contemporaneous, so care should be taken in drawing conclusions from this combined spectrum. Nevertheless, it can be seen that the γ-ray spectrum of Centaurus A has a complex shape, with a second component that emerges clearly between the last energy bins of the *Fermi* spectrum and the TeV data. This component may be interpreted in the light of hadronic or lepto-hadronic models [68] (see Section 1.3.3), or models based on magnetic reconnection [38]. The fact that Cen A has been proposed as a possible candidate source for the Ultra-High-Energy Cosmic Rays (UHECR) observed by the Pierre Auger Observatory [135] lends support to the models which include an hadronic component, since it would imply the presence of highly energetic protons in the jet of this source. If confirmed, this hypothesis would also identify Cen A as a candidate source for the high-energy neutrinos observed by the IceCube detector [1], since neutrinos are a necessary byproduct of hadronic processes.

M 87

M 87 has been observed at VHE by all the major Cherenkov telescopes. The

---

[6]The data from the second *MAGIC* campaign are consistent with those from the first campaign, so it would be redundant to show them.

comprehensive γ-ray spectrum including both LAT and VHE data points is shown in Fig. 4.8. The HE-VHE connection is quite complex in this case, since it is clear from the TeV data that the source is variable at these energies, as mentioned in the previous section.

IC 310

As mentioned in Section 3.4, IC 310 has been detected in the VHE energy range by the *MAGIC* telescope [20]. The data were taken between 2009 October and 2010 February, with a total live time of 20.6 hours. A comprehensive γ-ray spectrum including both LAT and *MAGIC* data points is shown in Fig. 4.9. The VHE spectrum is unusually hard. Our *Fermi* data points form an even flatter spectrum (albeit with large errors), which confirm this trend, indicating a high-energy SED peak at energies beyond 10 TeV. It should be noted that the data are not contemporaneous, since our LAT data are averaged over 6 year, including the 2012 flare discussed in the previous section [21].
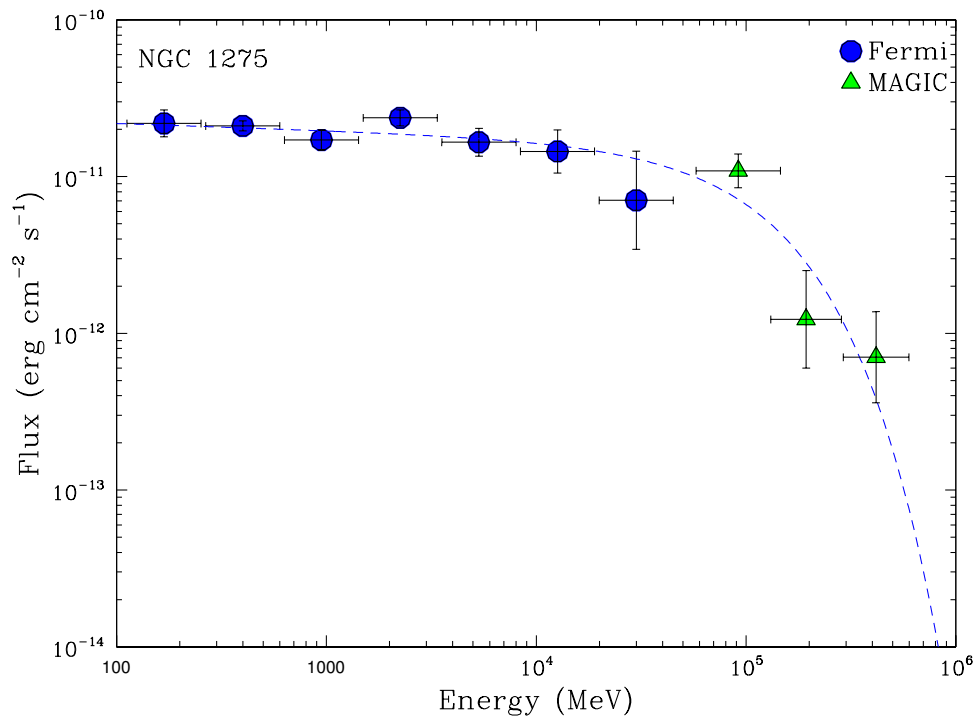
Figure 4.6: Comprehensive and contemporaneous γ-ray spectrum of NGC 1275. Blue filled circles are LAT data points (this work), green filled triangles are *MAGIC* data points [19]. The dashed blue line is the best-fit of the combined data set.
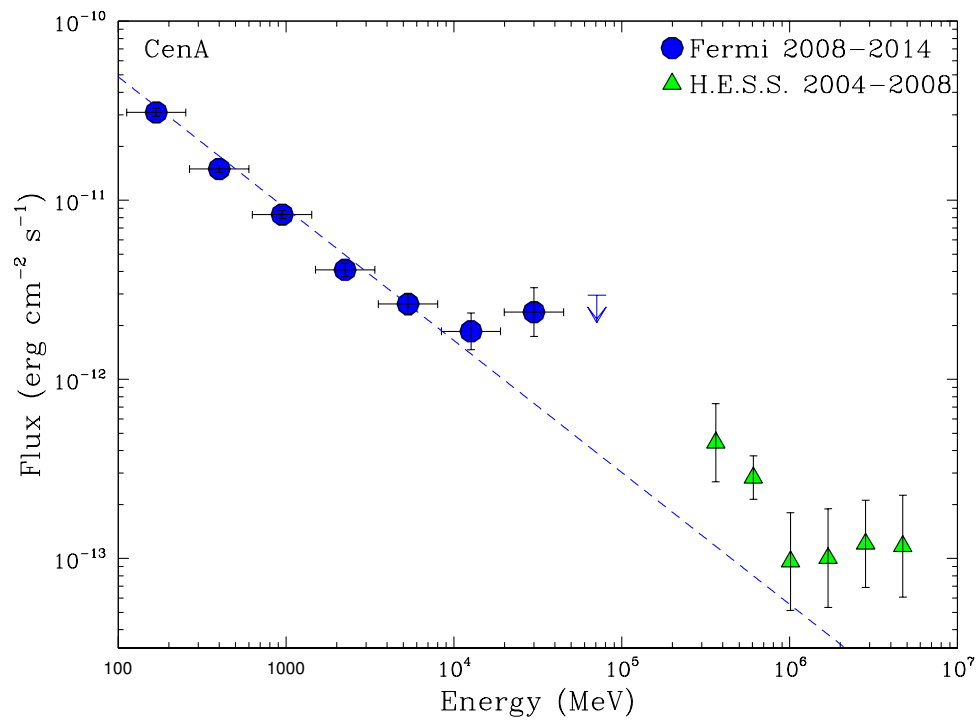
Figure 4.7: Comprehensive γ-ray spectrum of Cen A. Blue filled circles are LAT data points (this work), green filled triangles are *H.E.S.S.* data points [14]. The dashed blue line is the best fit LAT power-law.
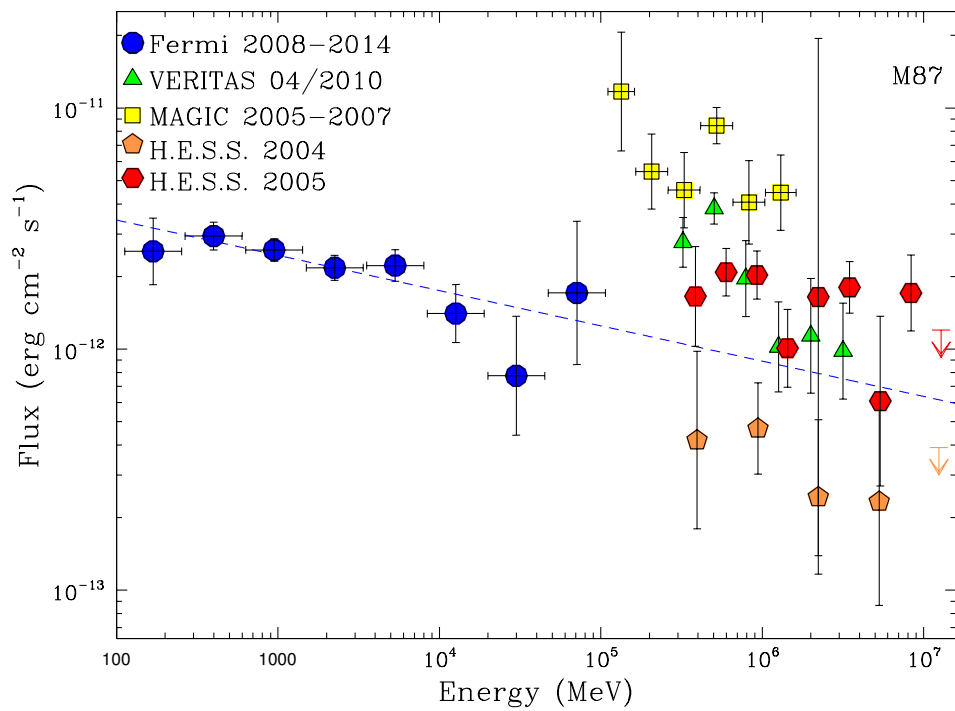
Figure 4.8: Comprehensive γ-ray spectrum of M 87. Blue filled circles are LAT data points (this work), green filled triangles are *VERITAS* data points [24], yellow filled squares are *MAGIC* data points [22], orange filled pentagons and red filled hexagons are *H.E.S.S.* data points [13]. The dashed blue line is the average LAT power-law.
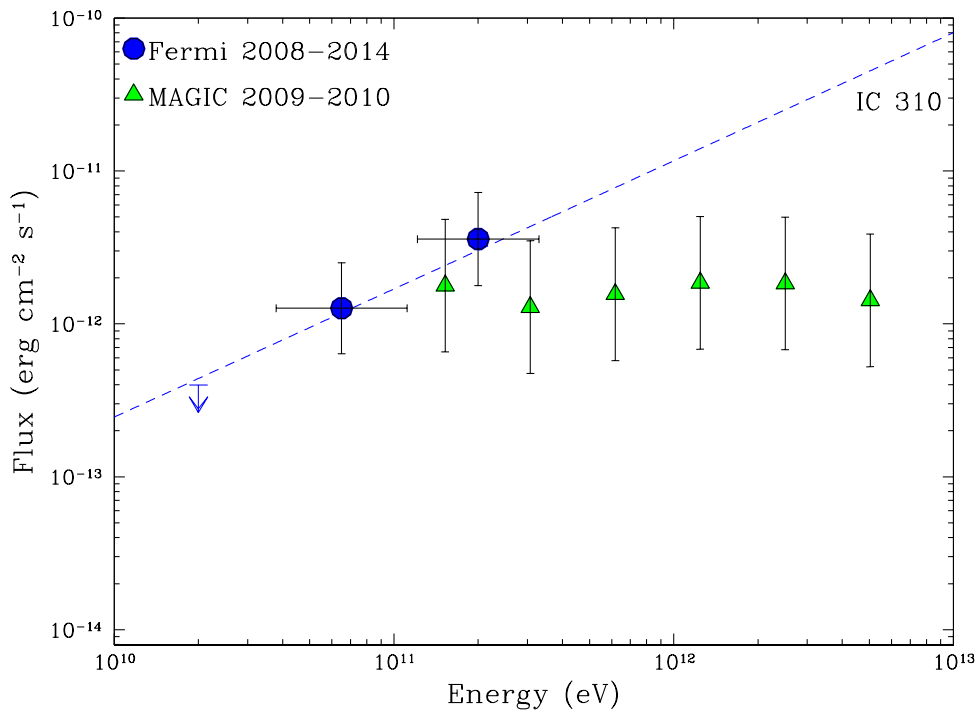
Figure 4.9: Comprehensive γ-ray spectrum of IC 310. Blue filled circles are LAT data points (this work), green filled triangles are *MAGIC* data points [20]. The dashed blue line is the best fit LAT power-law.

Chapter 5

CTA predictions

In this chapter we give an overview of the 3LAC MAGN sample, its composition and the observational properties of its sources. Moreover, we investigate whether the low energy properties of these objects can be used to predict their detectability in the TeV range (Section 5.1). Then we report the methods and results of our predictive analysis for the CTA for our candidate sources (Section 5.2.1) and for the current TeV radio galaxies (Section 5.2.2), in terms of integrated flux detections and spectral analysis (Section 5.3).

5.1 The 3LAC MAGN sample

The most up-to-date *Fermi* AGN catalog is the 3LAC (Ackermann et al. 2015 [11]). There are 23 MAGN included in the clean 3LAC catalog, more than double with respect to the previous sample, compiled by Abdo et al. 2010 [5], corresponding to the first 15 months of *Fermi* data. Our sample is presented in Table 5.2, where the main γ-ray spectral properties are listed. The sample includes radio galaxies, SSRQs, and CSS sources [1]. In addition to the 23 3LAC MAGN we have included 3C 120, which has never been included in the LAT catalogs, but has been firmly established as a γ-ray source [5] [160].

Table 5.1 reports the mean properties of the sample, divided by class. These values confirm the well known dichotomy between FR I and FR II sources. The FR I radio galaxies in our sample, on average, have a flatter spectrum and a lower redshift with respect to FR IIs. Additionally, FR I sources are by far the most populous class in the sample, while there are very few FR II radio galaxies. As

---

[1]Compact Steep Spectrum (CSS) sources are symmetrical, compact (1-20 kpc), steep spectrum radio sources which have been proposed to constitute the progenitors of classic radio galaxies (together with Gigahertz Peaked-Spectrum (GPS) sources). See the review by O'Dea 1998 [126] for more information on these sources.

discussed in Section 1.4.2, the nature of this dichotomy (which was noted already in the first systematic analysis of *Fermi* MAGN [5]) is still unclear. It could be due to the different mean redshift, or to different emission mechanisms.

Table 5.1: Properties of the *Fermi*-detected MAGN in the 3LAC catalog [11], divided by class. The values between brackets are medians, while σ indicates the corresponding standard deviation. The median flux is in units of 10^{-8} photons cm^{-2} s^{-1}.

Subset	N(%)	$< F >$	σ_F	$< \Gamma >$	σ_Γ	$< z >$	σ_z
FR I[a]	13 (54%)	0.13	7.7	2.16	0.37	0.021	0.016
FR II	3 (13%)	0.032	0.023	2.49	0.36	0.049	0.047
SSRQ	5 (21%)	0.034	0.009	2.43	0.12	0.63	0.36
SSRQ/CSS	2 (8%)	0.15	0.062	2.6	0.12	0.85	0.08
CSS[b]	1 (4%)	0.047	*	2.44	*	1.21	*
Total	24 (100%)	0.047	5.9	2.32	0.34	0.035	0.38

[a] We note that the average flux, $< F >= 3.3$, is significantly different from the median reported in the table for this class.
[b] There is no standard deviation for this class because we only have one source.

The aim of this work is to predict whether the CTA will be able to increase the number of TeV detected MAGN. We investigated whether the low-energy properties of the 3LAC TeV blazars could be used as a proxy to identify good TeV candidates in our MAGN sample. As mentioned in Chapter 1, the SED of blazars is completely dominated by two non-thermal peaks, one at low energy (radio to X-ray), and one at high-energy (X-ray to TeV). The low-energy peak is generally attributed to synchrotron radiation by a population of relativistic electrons. It is noticeable that the frequency at which this peak can occur (ν^s_{peak}) spans a very broad range, approximately from $\sim 10^{12.5}$ Hz up to over 10^{18} Hz. Blazars with $\nu^s_{peak} < 10^{14}$ Hz are called *Low-synchrotron peaked* sources (LSP), those with 10^{14} Hz $< \nu^s_{peak} < 10^{15}$ Hz are called *Intermediate-synchrotron peaked* sources (ISP), while those with $\nu^s_{peak} > 10^{15}$ Hz are called *High-synchrotron peaked* sources (HSP). In this respect, the distribution of ν^s_{peak} in the two main blazar classes is very different. FSRQs have $< \nu^s_{peak} >= 10^{13.1\pm0.1}$ Hz, with a dispersion of only 0.5 dex, and therefore are always LSPs. BL Lacs, on the other hand, span a much wider range of ν^s_{peak}, extending up to $\nu^s_{peak} 10^{18}$ Hz (the mean value

Table 5.2: Table summarizing the sample of all *Fermi*-detected MAGN in the 3LAC catalog [11]. Sources in bold are also detected in the TeV band, and the spectral parameters reported for these sources are the result of our analysis (see Section 4.2).

Object	3LAC Name	Γ^a	*Fermi* flux^b	z	Class
3C 78	J0308.6+0408	2.07±0.11	0.06±0.01	0.029	FRI
IC 310	J0316.6+4119	1.2±0.5	0.015±0.006	0.018	FRI
NGC 1275^c	J0319.8+4130	2.08±0.01	24.9±0.3	0.018	FRI
Fornax A	J0322.5-3721	2.20±0.11	0.047±0.008	0.005	FRI
TXS 0331+391	J0334.2+3915	2.11±0.17	0.037±0.009	0.0206	FRI
TXS 0348+013	J0351.1+0128	2.43±0.18	0.034±0.009	1.12	SSRQ
3C 111	J0418.5+3813c	2.79±0.08	0.07±0.01	0.049	FRII
3C 120^d		2.71±0.35	2.9±1.7	0.033	FRI
Pictor A	J0519.2-4542	2.49±0.18	0.032±0.007	0.035	FRII
PKS 0625-35	J0627.0-3529	1.87±0.06	0.14±0.01	0.055	FRI
3C 189	J0758.7+3747	2.16±0.16	0.025±0.007	0.0428	FRI
4C+39.23B^e	J0824.9+3916	2.4±0.1	0.047±0.007	1.21	CSS
3C 207	J0840.8+1315	2.47±0.09	0.052±0.008	0.681	SSRQ
4C+39.26	J0934.1+3933	2.28±0.12	0.037±0.007	-	SSRQ
3C 264	J1145.1+1935	2.0±0.2	0.027±0.007	0.0217	FRI
4C+04.40^e	J1205.4+0412	2.64±0.16	0.024±0.007	0.6285	SSRQ
M 87	J1230.9+1224	2.15±0.05	2.1±0.1	0.0036	FRI
3C 275.1	J1244.1+1615	2.43±0.17	0.030±0.007	0.5551	SSRQ
Cen A	J1325.4-4301	2.737±0.006	17.6±0.5	0.0009	FRI
3C 286	J1330.5+3023	2.60±0.16	0.025±0.006	0.8499	SSRQ/CSS
Cen B	J1346.6-6027	2.32±0.01	0.20±0.02	0.0013	FRI
3C 303	J1442.6+5156	1.92±0.18	0.019±0.005	0.141	FRII
NGC 6251	J1630.6+8232	2.22±0.08	0.13±0.01	0.025	FRI
3C 380	J1829.6+4844	2.37±0.04	0.15±0.01	0.692	SSRQ/CSS

^{a} *Fermi* spectral index.

^{b} Flux above 1 GeV in units of 10^{-8} photons cm^{-2} s^{-1}.

^{c} NGC 1275 is best fitted by a logparabola with parameters $\alpha = (2.02 \pm 0.02)$ and $\beta = (0.07 \pm 0.01)$. The spectral index reported in the table is referred to a power-law fit.

^{d} Spectral information from Abdo et al. 2010 [5].

^{e} These sources are part of a double association with FSRQs (4C+39.23 and MG1 120448+0408, respectively), so their detection is not robust (see Section 4.2 in Ackermann et al. 2015 [11]).

strongly depends on the selection band), and therefore can be LSP, ISP, or HSP sources [78]. In these cases they are called LBL, IBL and HBL, respectively.

The difference in the distribution of ν^s_{peak} between FSRQs and BL Lacs can be seen in the 3LAC catalog. Fig. 5.1 shows the counts distribution of the logarithm of ν^s_{peak} for all FSRQs, BL Lacs and radio galaxies in the 3LAC catalog. It can be easily seen that BL Lac span a much wider range in ν^s_{peak} with respect to FSRQs. Interestingly, the same appears to be true for *Fermi* radio galaxies, which include mostly FR I sources.

Blazars make up all but few of the extragalactic sources observed at TeV energies. For example within the TeVcat catalog [2], the extragalactic sources include 58 blazars, 4 radio galaxies and 3 starbursts. As one would naturally expect, HBLs are in turn the great majority of TeV detected blazars, with a total of 44 sources. The rest are LBLs (1), IBLs (7), FSRQ (5) and of unknown type (1). Therefore, one would be tempted to adopt a high synchrotron peak frequency as a parameter for TeV candidate selection. The plots in Fig. 5.2 represents the VHE flux (upper panel) and spectral index (lower panel) as a function of ν^s_{peak}, for BL Lacs, FSRQs and radio galaxies, corrected for EBL absorption. The low statistics and the fact that the TeV catalogs are not statistically complete prevent us from drawing a robust conclusion from these data, and so we are not able to claim a correlation of the VHE spectral properties with the peak synchrotron frequency, nor to rule it out completely. Therefore, we must adopt other criteria in order to identify good TeV candidates and predict their VHE properties.

The most natural candidates for TeV detection would be the sources already detected by *Fermi*, since a source visible in TeV band would likely be observed also in the GeV range (with some exceptions and borderline sources, see for example IC 310 in the previous chapter). As an example we have gathered multi-wavelength data and produced a complete SED for NGC 1275, which is shown in Fig. 5.3. Since we are interested in the γ-ray emission, we tried to select the data so as to include only non-thermal emission from our sources, in order to compare the SED with the classical double-peaked shape of blazars. This selection is not trivial, since the SED of radio galaxies is not strongly dominated by the two non-thermal peaks, and so the observed emission may be contaminated, e.g. by light from the host galaxy. In this case, there is probably some contamination from cluster cooling flow emission in the X-rays (see Section 3.1).
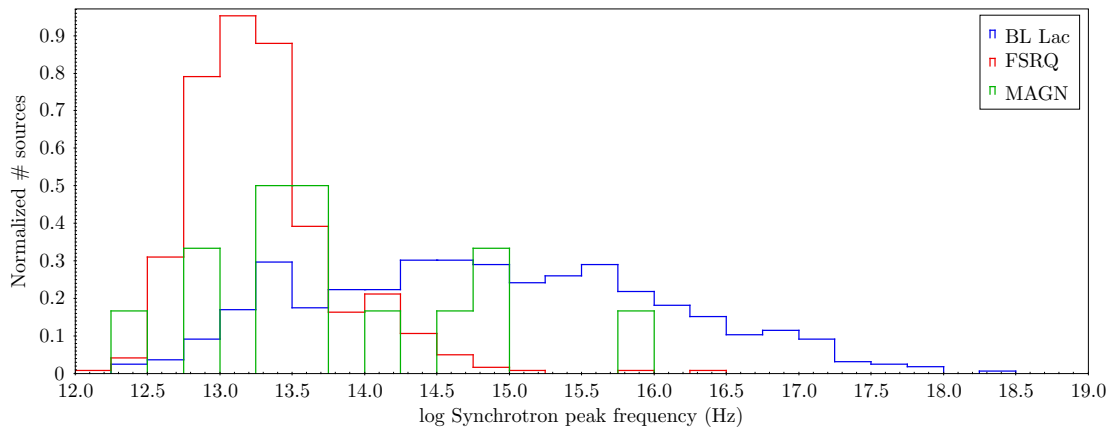
---

[2]URL: http://tevcat.uchicago.edu/

Figure 5.1: Normalized counts distribution of the logarithm of ν_{peak}^s for identified sources in the 3LAC catalog. Blue lines represent BL Lacs, red lines represent FSRQs, green lines represent MAGN.
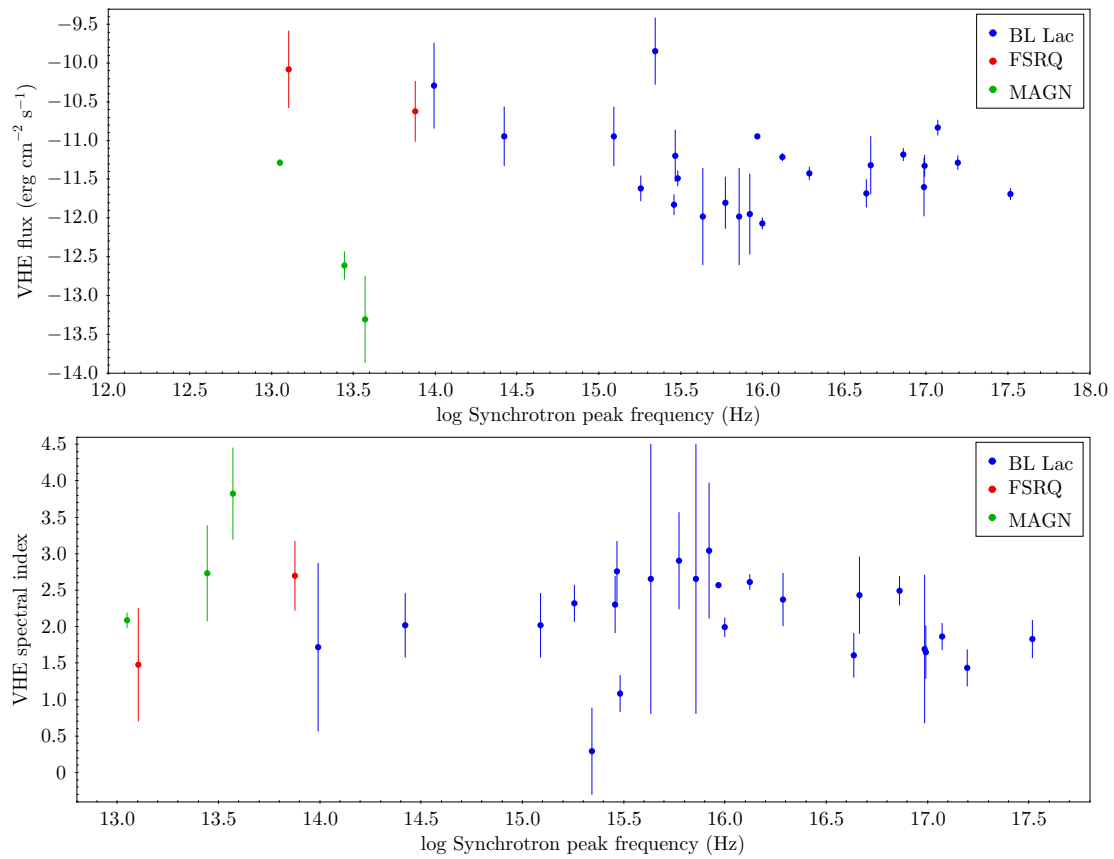
Figure 5.2: Log-Log plot of the VHE flux (top panel) and photon index (bottom panel) versus synchrotron peak frequency for TeV detected AGN. Blue circles represent BL Lacs, red circles represent FSRQs, green circles represent MAGN.
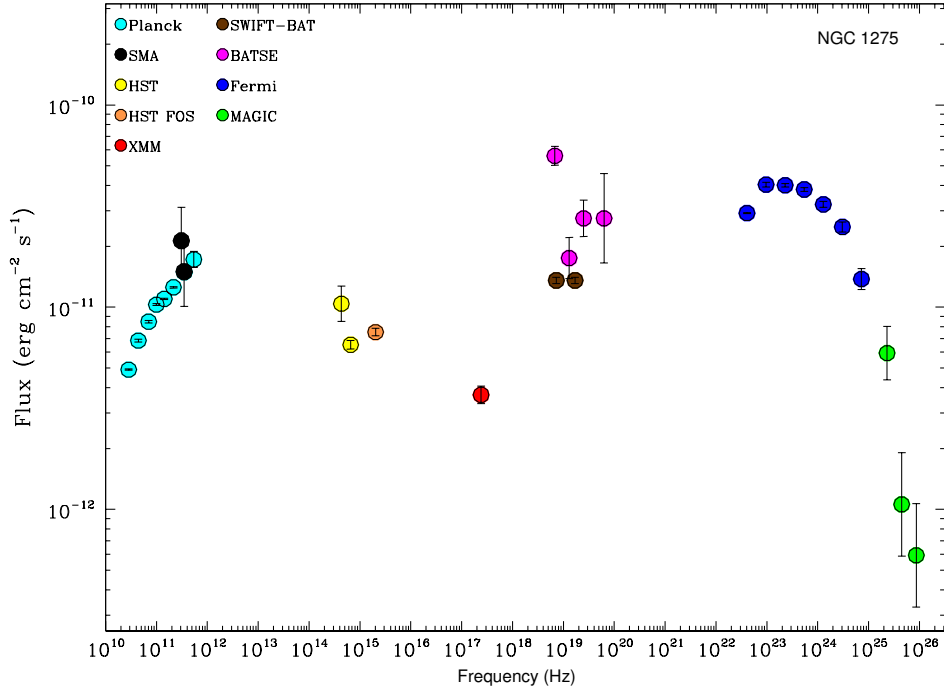
Figure 5.3: Spectral Energy Distribution of NGC 1275. Light blue points are data from the Planck point source catalog, black points are SMA catalog data, yellow points are HST data (Chiaberge et al. 1999 [52]), orange points are HST FOS data (Johnstone & Fabian 1995 [94]), red points are XMM data (Torresi 2011 [167]), brown points are SWIFT-BAT data from the 70-month catalog (Baumgartner et al. 2013 [36]), magenta points are BATSE data (Harmon et al. 2004 [88]), blue points are *Fermi*-LAT data (this work), and green points are *MAGIC* data (Aleksić et al. 2014 [19]).

5.2   Integrated flux predictions

5.2.1   Detection of new TeV MAGN

Adopting our 3LAC MAGN sample described in Section 5.1 as a possible TeV candidate sample, we first attempted to predict the integrated flux for our sources that would be measured by the CTA. To do this, we employed the software package *ctools* [3]. *ctools* is a software package which is used for the scientific analysis of CTA and IACT data in general. We used the *ctobssim* tool to simulate 50 hours of CTA observations for our candidate sources, providing as input a model file for our sources, the CTA sensitivity curve and background spectrum. As input model for each source, we assumed a simple extrapolation of their 3FGL power-law spectrum. We then performed a standard likelihood analysis on the resulting event file, using the *ctlike* tool. This provided the Test Statistic (TS, see Section 4.1.2), and a second model file with the resulting spectral parameters (normalization and spectral index) and errors.

Based on these spectral parameters, we integrated the resulting analytical spectral shape for each source in the CTA energy range, i.e. 0.02-100 TeV. The error on the resulting integrated flux was obtained through a standard propagation of the errors on the normalization and spectral index.

We also took into account the effect of absorption by the EBL (see Section 1.3.5). We assumed the EBL model by Dominguez et al. 2011 [57], which gives the optical depth values for a grid of energies and redshifts. Then, for each candidate source we interpolated these values at a grid of 10^3 energy points in the range of the CTA and at the source redshift, obtaining the correct values of $\tau(E,z)$. We then multiplied the absorption factor $e^{-\tau}$ to the source analytical spectral shape, before integrating it over the CTA energy range. The resulting correction between the observed (i.e. EBL absorbed) flux and the intrinsic one (i.e. the ratio of the intrinsic flux and the EBL absorbed flux) ranges from 1 to around 3, with mean value 1.73±0.70.

Our results indicate that this correction factor depends not only on redshift, but has also a mild dependence on the spectral index, i.e. sources with a harder spectrum suffer from stronger EBL absorption at a given redshift. This dependence, although less obvious than the dependence on redshift, is to be expected since, as mentioned in Section 1.3.5, the cross-section for the EBL absorption process is a strong positive function of the γ-ray photon energy, therefore a source with a harder spectrum, i.e. a larger number of highly energetic photons, will suffer a stronger suppression of its integrated flux with respect to a soft-spectrum source (for the same flux).

---

[3]Web page URL: http://cta.irap.omp.eu/ctools/

Usually the detection significance for a γ-ray source is is given by $\sigma \sim \sqrt{TS}$. In the *Fermi* catalogs, for example, a source is considered detected if $TS > 25$. In our case, this estimate is not reliable for objects with $z > 0.1$, since the *ctools* simulations and analysis tools do not take into account EBL absorption. Excluding these sources, we have a total of 9 objects with $TS > 25$. The results of our analysis are displayed in Fig 5.4, 5.5, 5.6 and Table 5.3. The plots show the TS of our simulated observations versus the signal-to-noise ratio, the *Fermi* spectral index and the *Fermi* flux, respectively, for our $TS > 25$ candidates. We can see that there is a clear correlation between these quantities, with a correlation coefficient of $r = 0.82$, $r = -0.75$ and $r = 0.56$ respectively. The chance probability (*p*-value) for these correlations is $p \sim 0.0034$, $p \sim 0.010$ and $p \sim 0.054$, therefore the first two correlations are highly significant, while the last is marginally significant.

According to our results, the best TeV MAGN candidates are either very nearby sources, like Centaurus B, or have a hard *Fermi* spectrum, like PKS 0625-35 or 3C 78 (see Table 5.2). This is made clear by the correlation displayed in Fig. 5.5. These two properties appear to be the best requirements for a good TeV candidate. The detection significance also shows a less significant correlation with *Fermi* flux, as can be seen in Fig. 5.6.

It must be noted that the assumption of a smooth extrapolation of the *Fermi* spectrum up to energies of the order of 100 TeV is very optimistic. It is likely that the SED of these sources will cut off in the CTA band. To test a more realistic scenario, we assumed a steep exponential cutoff at 100 GeV, similar to the observed spectrum of NGC 1275. The results are shown in Table 5.4. In this scenario, we still have at least one new detection with $TS > 25$, i.e. PKS 0625-35, and two other sources with borderline values ($TS \sim 11$ for Cen B and $TS \sim 9$ for NGC 6251) [4] [5]. Therefore, we expect the detection of at least 2-3 new MAGN with the CTA in our most realistic scenario.

For a comparison of our results with current plans for extragalactic observations with the CTA, we refer to the discussion in Chapter 6.

---

[4]Note that $TS > 9$ still corresponds to a significance of about 3σ, which is considered reliable in γ-ray studies.

[5]In this case we use the TS to estimate the detection significance because these candidates are all local ($z < 0.1$).

Table 5.3: Results of the simulated CTA observations and data analysis, in the hypothesis of a straight extrapolation of the *Fermi*-LAT spectrum. For sources with $TS < 25$ a 1σ flux upper limit is placed.

Source	Γ^a	Flux^b	SNR	TS	z
3C 78	2.05±0.03	3.7±0.4	10.0	2565	0.029
Fornax A	2.05±0.06	1.3±0.3	5.0	479	0.005
TXS 0331+391	2.03±0.04	1.8±0.3	6.1	918	0.0206
TXS 0348+013^c	2.4±0.2	< 0.2	0.9	21.9	1.12
3C 111	*	*	*	< 0	0.049
3C 120	*	*	*	< 0	0.033
PictorA	2.5±0.5	< 0.2	0.9	3.3	0.035
PKS 0625-35	1.865±0.007	21±1	19.5	56522	0.055
3C 189	2.13±0.07	0.9±0.2	3.9	265	0.0428
4C+39.23B^c	2.2±0.3	< 2	0.6	16.5	1.21
3C 207^c	2.3±0.2	< 0.2	1.1	38.6	0.681
4C+39.26	2.3±0.1	0.8±0.2	3.9	83	*
3C 264	1.94±0.03	2.8±0.4	6.8	2247	0.0217
4C+04.40^c	*	*	*	< 0	0.6285
3C 275.1^c	2.2±0.5	< 0.2	0.4	5.7	0.5551
3C 286^c	*	*	*	< 0	0.8499
Cen B	2.33±0.03	5.2±0.3	16.8	1353	0.0013
3C 303^c	1.91±0.03	1.5±0.4	3.6	2347	0.141
NGC 6251	2.16±0.03	4.0±0.3	12.4	2020	0.025
3C 380^c	2.40±0.05	1.5±0.3	5.3	409	0.692

^{a} Simulated spectral index.
^{b} Simulated integrated flux between 20 GeV and 100 TeV. Units of 10^{-12} erg cm^{-2} s^{-1}.
^{c} Distant ($z > 0.1$) sources. The TS for these objects is not reliable since EBL absorption is not taken into account.

Table 5.4: Results of the simulated CTA observations and data analysis, in the hypothesis of a power-law with exponential cutoff at 100 GeV. The resulting data are fitted with a power-law. For sources with $TS < 25$ a 1σ flux upper limit is placed.

Source	Γ^a	Flux^b	SNR	TS	z
3C 78	3.3±1.5	< 80	0.01	1.4	0.029
Fornax A	*	*	*	< 0	0.005
TXS 0331+391	*	*	*	0.9	0.0206
TXS 0348+013^c	*	*	*	< 0	1.12
3C 111	*	*	*	< 0	0.049
3C 120	*	*	*	< 0	0.033
PictorA	*	*	*	< 0	0.035
PKS 0625-35	2.0±0.2	4.5±2.2	2.1	85.2	0.055
3C 189	*	*	*	< 0	0.0428
4C+39.23B^c	*	*	*	< 0	1.21
3C 207	*	*	*	< 0	0.681
4C+39.26	*	*	*	< 0	*
3C 264	*	*	*	< 0	0.0217
4C+04.40^c	*	*	*	< 0	0.6285
3C 275.1^c	*	*	*	< 0	0.5551
3C 286^c	*	*	*	< 0	0.8499
Cen B	2.5±0.5	< 4.6	0.5	11.1	0.0013
3C 303^c	*	*	*	< 0	0.141
NGC 6251	2.4±0.5	< 4.6	0.4	8.7	0.025
3C 380^c	3.4±1.2	< 40	0.04	2.6	0.692

^{a} Simulated spectral index.

^{b} Simulated integrated flux between 20 GeV and 100 TeV. Units of 10^{-12} erg cm^{-2} s^{-1}.

^{c} Distant ($z > 0.1$) sources. The TS for these objects is not reliable since EBL absorption is not taken into account.
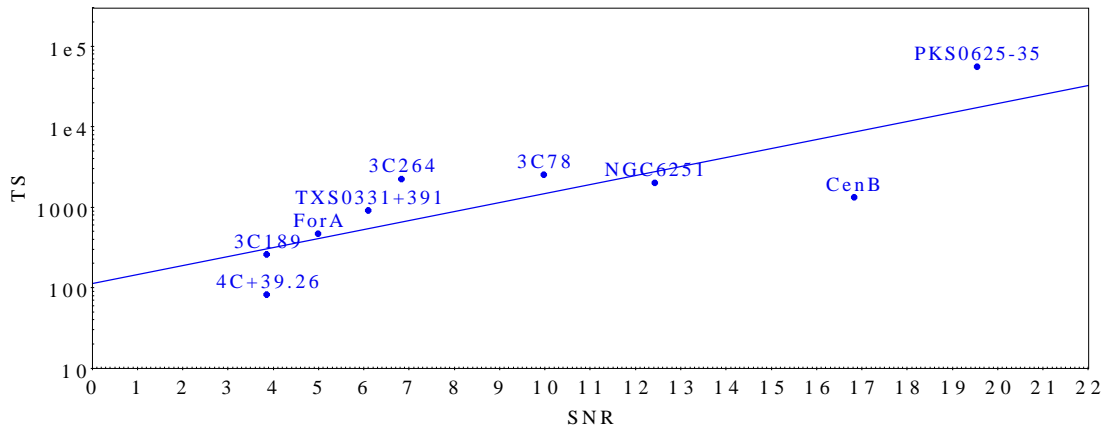
Figure 5.4: TS versus signal-to-noise ratio for our $TS > 25$ candidates. A linear fit with the expression $\log(TS) = 0.112 \times \text{SNR} + 2.055$ gives a correlation coefficient $r \sim 0.82$.
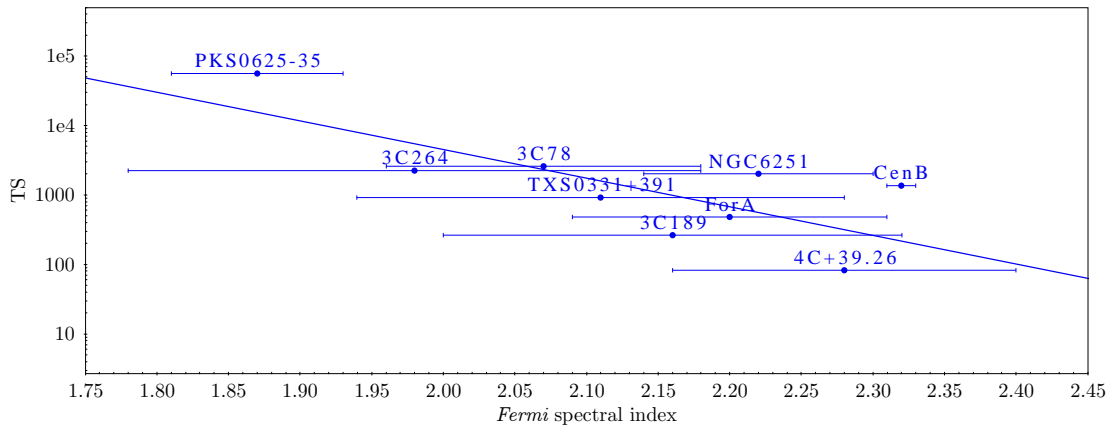

Figure 5.5: TS versus *Fermi* spectral index for our $TS > 25$ candidates. A linear fit with the expression $\log(TS) = -4.12 \times \Gamma + 11.9$ gives a correlation coefficient $r \sim -0.75$.
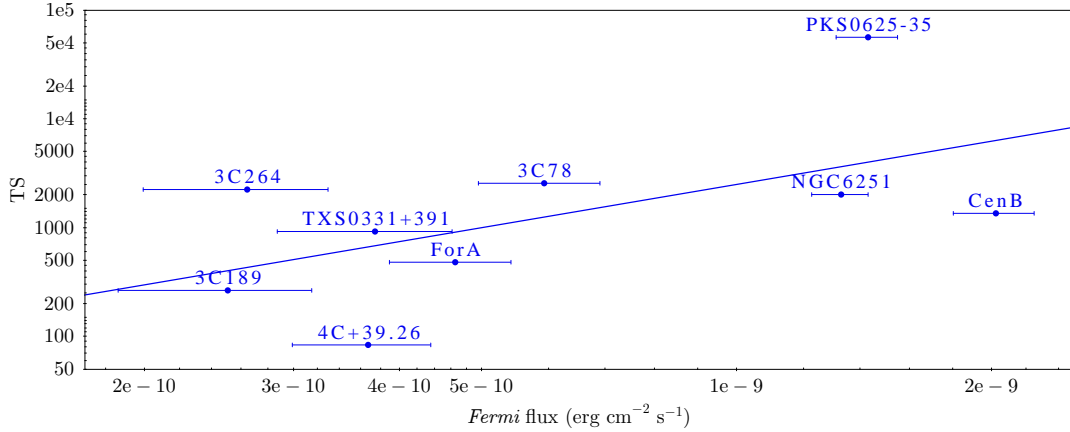
Figure 5.6: TS versus *Fermi* flux for our $TS > 25$ candidates. A linear fit with the expression $\log(TS) = 1.32 \times \log(F) + 15.3$ gives a correlation coefficient $r \sim 0.57$.

5.2.2 CTA performance on the current TeV MAGN

In addition to the possible detection of new TeV MAGN, the CTA will, in any case, provide much better data for the ones already detected (NGC 1275, Cen A, M 87, IC 310), which suffer from poor statistics and therefore low SNR spectra. This implies that their spectral shape cannot be investigated in detail. TeV spectra with higher SNR would, for example, allow us to discriminate between leptonic and hadronic models (see Section 1.3), since these models predict significantly different shapes particularly in this energy range [44], which can only be constrained if the spectrum has good statistics. Additionally, better quality spectra may allow to constrain different emission components (e.g. diffuse lobes), the existence of which has been proposed to explain the γ-ray spectrum of Centaurus A.

To test the extent to which the CTA will improve the SNR in these sources, we simulated CTA observations using the *ctools* package in the same way described above for the 3LAC MAGN. As an input model, since in this case we already have actual TeV data, we used the observed TeV spectral parameters of our four sources instead of extrapolating the LAT spectrum. As for the MAGN candidates, we performed a likelihood analysis on the resulting simulated data, and integrated the resulting spectral parameters (correcting for EBL absorption) over the same range as the real data, in order to be able to compare the two in a consistent way. The result is displayed in Fig. 5.7 and Table 5.5. The plot shows the simulated CTA spectral index versus the simulated integrated flux for our sources, together

with the same quantities derived from real TeV spectral data. We can see that the SNR of the CTA data is greatly improved with respect to the data from the current IACTs, by a factor ranging from ~ 4 to ~ 14. The improvement in the TS is even greater, from ~ 11 up to ~ 240.

We have also investigated the performance of the CTA for spectral analysis, by simulating observations of NGC 1275 in different energy bins, with the same model described above. The corresponding spectrum is shown in Fig 5.8. The improvement obtained with the CTA, with respect to *MAGIC*, is remarkable. We will be able to obtain a spectrum with excellent signal-to-noise ratio up to 400 GeV with a 50-hour observation. With longer exposure times (i.e. 500-1000 hours), the source would be detected up to $\sim$1 TeV.
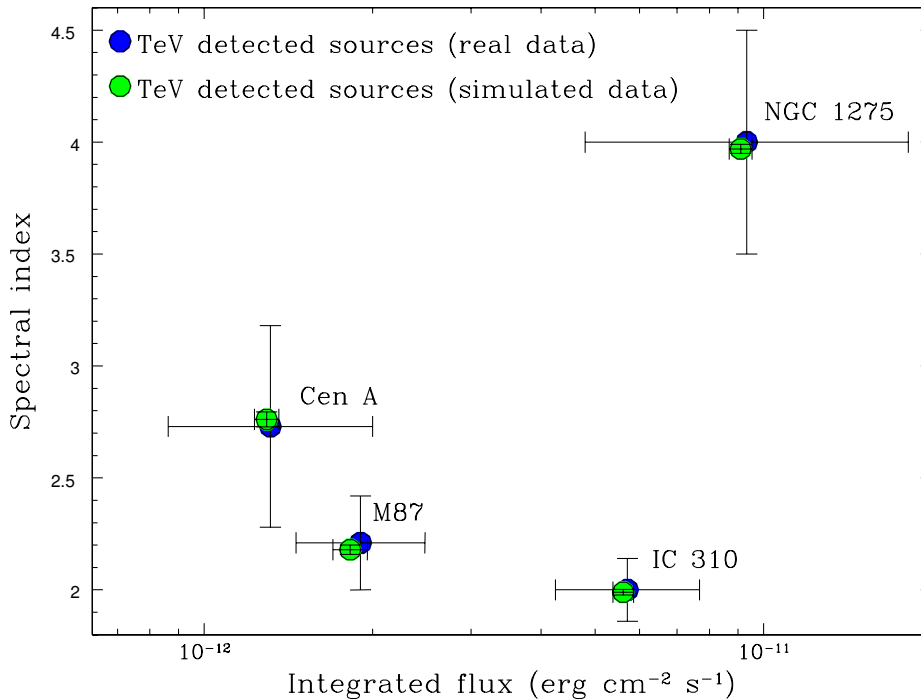

Figure 5.7: Simulated CTA spectral index versus integrated flux for the four TeV detected MAGN. Green points represent the simulated CTA data, blue points represent the real data from the current IACTs. Spectral data from [19],[14],[22], and [20] for NGC 1275, Cen A, M 87 and IC 310, respectively.
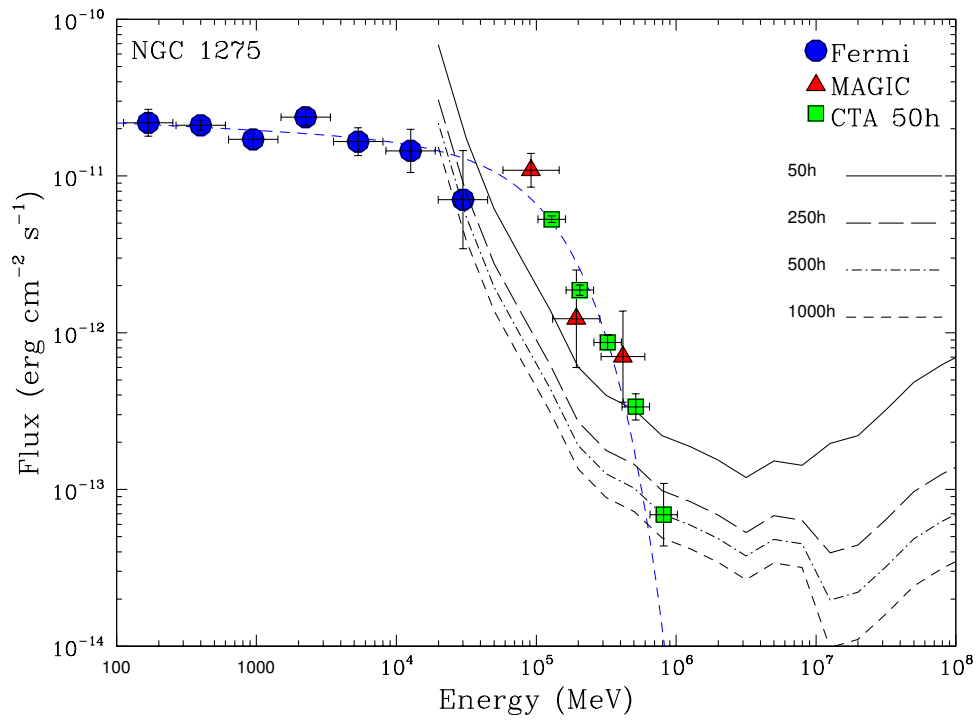
Figure 5.8: Simulated CTA spectrum of NGC 1275 (green points), together with *Fermi* data (blue points), real MAGIC data (red points), and preliminary CTA differential sensitivity curves for different observing times (black lines).

Table 5.5: Comparison between the spectral properties of the current TeV detected MAGN with current data, and with our simulated CTA data. The simulated fluxes are integrated over the same energy range in which these sources have been observed. The flux is in units of 10^{-12} erg cm^{-2} s^{-1}.

Source	Γ	Flux	SNR	TS	z
IC 310	2.0±0.1	12±2	5.50	1024	0.018
IC 310 (CTA)	1.99±0.01	11.0±0.6	19.10	11553	0.018
NGC 1275[a]	4.0±0.5	< 1000	*	37.21	0.018
NGC 1275 (CTA)	3.97±0.02	370±30	13.96	8865	0.018
M 87	2.21±0.21	5.9±1.6	3.67	169	0.0036
M 87 (CTA)	2.18±0.02	5.4±0.4	13.53	3411	0.0036
Cen A[a]	2.73±0.45	< 24	*	25	0.0009
Cen A (CTA)	2.76±0.03	9.5±1.4	6.89	1032	0.0009

[a] Because of the large errors on the integrated flux, a 1σ upper limit is placed.

5.3 Spectral analysis predictions

In addition to the integrated flux predictions, we have also investigated the spectral performance of the CTA for our TeV MAGN candidates. In order to do this, we extrapolated their 3FGL *Fermi* spectra into the VHE range. We assumed as template for the MAGN emission in the HE-VHE range a power-law with exponential cutoff, as suggested by the only source for which we have a reliable contemporaneous MeV-TeV spectrum (i.e. NGC 1275). Different cutoff energies between 10 GeV and 10 TeV were considered. We then compared the resulting extrapolated spectra with preliminary CTA differential sensitivity curves, for different observing times, from the standard 50 hours up to 1000 hours. We have also accounted for EBL absorption in the same way described in the previous section. The resulting spectra are shown in Fig. 5.9, 5.10 and 5.11. A quantitative summary of this analysis is presented in Table 5.6. The table reports the CTA observing times which would be necessary to obtain a spectrum for our candidate sources, for the different cutoff energies considered, together with the *Fermi* spectral parameters used for the extrapolation and the source's redshift.

We can see that steep spectra ($\Gamma > 2.1$) and low *Fermi* fluxes ($F < 2 \cdot 10^{-8}$ photons cm^{-2} s^{-1}) make the spectral analysis of most of the MAGN in our sample quite challenging. Additionally, EBL absorption is critical above 1 TeV, and significantly contributes to suppress the highest-energy emission for our most distant sources ($z > 0.1$). The most promising sources are identified by the same criteria described in the previous section, i.e. a flat spectrum ($\Gamma < 2.1$) and low

redshift ($z < 0.1$), therefore they are all local FR I sources (e.g. PKS 0625-35, 3C 78, NGC 6251, Cen B). These objects could be detected with long effective observing times, i.e. $t_{eff} \sim 250 - 500$ h, if their spectrum cuts off at energies greater than about 100 GeV. Since most of these sources would be detected in the low-medium energy range of the CTA, and in this range the sensitivity declines as $S \propto (t_{eff})^{-1/2}$, further increasing the effective observing time would not lead to a significant increase in the SNR of the data.

Table 5.6: Results of the spectral analysis predictions for the CTA. The table reports the approximate observing times which would be necessary to obtain a spectrum, for the different cutoff energies considered, together with the Fermi spectral properties used for the extrapolation, and the source redshift. The cases with a cutoff at 10 GeV and 50 GeV are not reported since no source is above the sensitivity curves. Flux in units of 10^{-8} photons cm^{-2} s^{-1}.

Source	Γ	Flux	z	100 GeV	500 GeV	1 TeV	10 TeV
3C 78	2.07±0.11	0.06±0.01	0.029	*	250 h	250 h	50 h
Fornax A	2.20±0.11	0.047±0.008	0.005	*	1000 h	500 h	250 h
TXS 0331+391	2.11±0.17	0.037±0.009	0.0206	*	500 h	250 h	250 h
TXS 0348+013	2.43±0.18	0.034±0.009	1.12	*	*	*	*
3C 111	2.79±0.08	0.07±0.01	0.049	*	*	*	*
3C 120	2.71±0.35	2.9±1.7	0.033	*	*	*	*
Pictor A	2.49±0.18	0.032±0.007	0.035	*	*	*	*
PKS 0625-35	1.87±0.06	0.14±0.01	0.055	250 h	50 h	50 h	50 h
3C 189	2.16±0.16	0.025±0.007	0.0428	*	*	1000 h	500 h
4C+39.23B	2.4±0.1	0.047±0.007	1.21	*	*	*	*
3C 207	2.47±0.09	0.052±0.008	0.681	*	*	*	*
4C+39.26	2.28±0.12	0.037±0.007	*	*	*	1000 h	500 h
3C 264	2.0±0.2	0.027±0.007	0.0217	*	250 h	250 h	50 h
4C+04.40	2.64±0.16	0.024±0.007	0.6285	*	*	*	*
3C 275.1	2.43±0.17	0.030±0.007	0.5551	*	*	*	*
3C 286	2.60±0.16	0.025±0.006	0.8499	*	*	*	*
Cen B	2.32±0.01	0.20±0.02	0.0013	*	250 h	250 h	50 h
3C 303	1.92±0.18	0.019±0.005	0.141	*	500 h	500 h	250 h
NGC 6251	2.22±0.08	0.13±0.01	0.025	*	250 h	50 h	50 h
3C 380	2.37±0.04	0.15±0.01	0.692	*	*	*	*

Figure 5.9: Extrapolated spectra for the MAGN in the 3LAC sample. The colors indicate the cutoff energy: blue 10 GeV, red 50 GeV, yellow 100 GeV, green 500 GeV, light blue 1 TeV, magenta 10 TeV. The lines represent the differential sensitivity curve of the CTA, for different observing times, from 50 hours to 1000 hours. The source redshift and *Fermi* spectra index are reported in the top right corner of the figure.
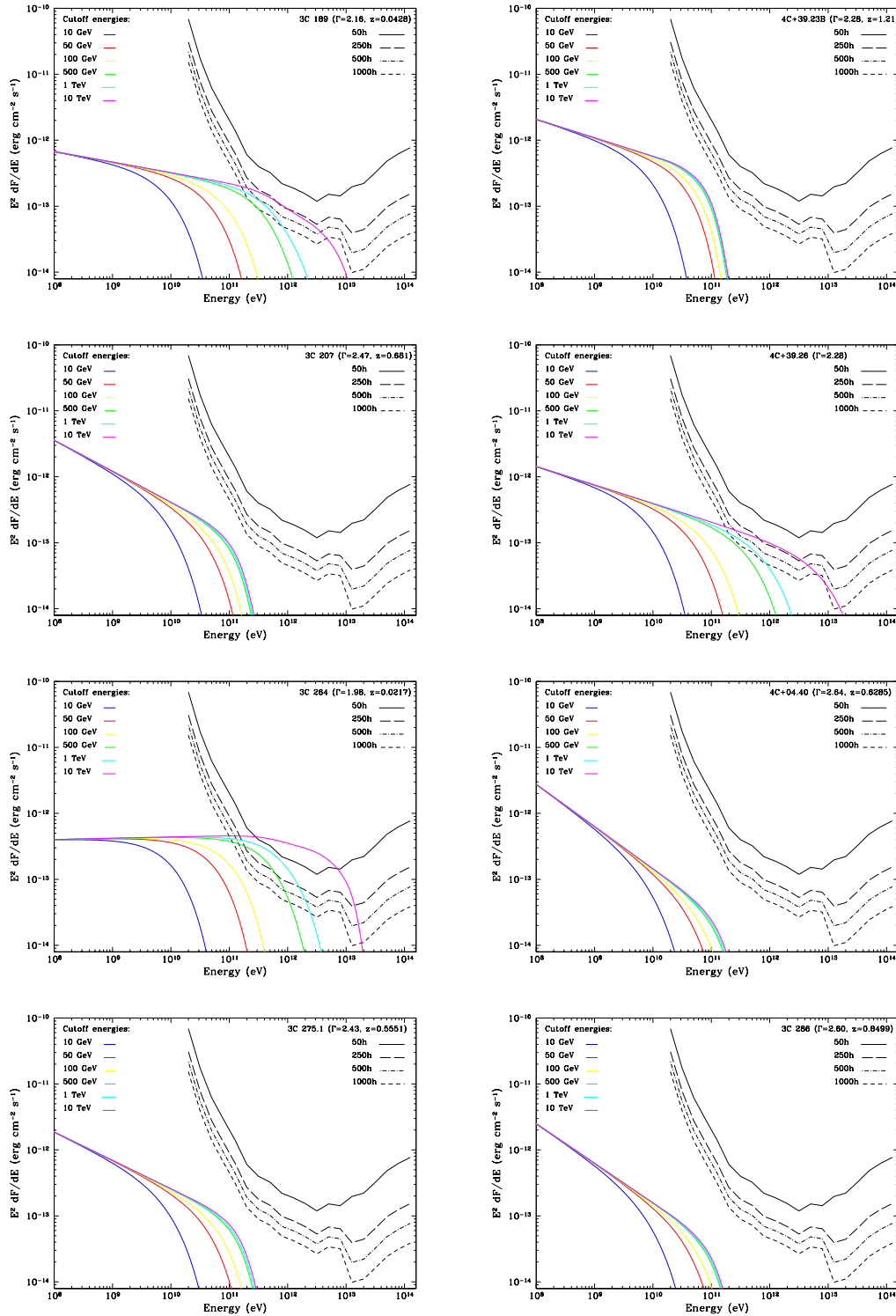
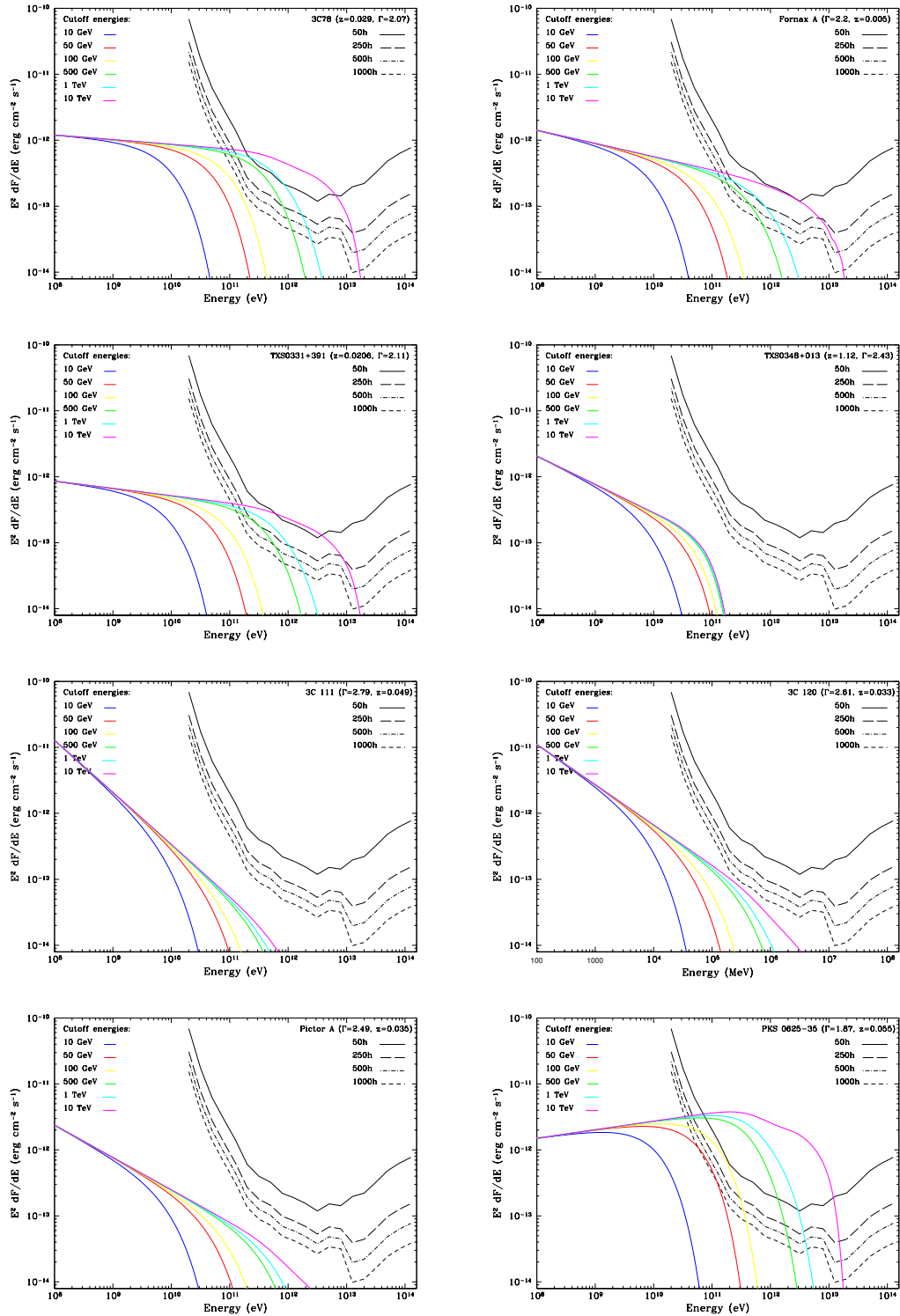Figure 5.10: *Continued*: Extrapolated spectra for the MAGN in the 3LAC sample. The colors indicate the cutoff energy: blue 10 GeV, red 50 GeV, yellow 100 GeV, green 500 GeV, light blue 1 TeV, magenta 10 TeV. The lines represent the differential sensitivity curve of the CTA, for different observing times, from 50 hours to 1000 hours. The source redshift and *Fermi* spectra index are reported in the top right corner of the figure.

Figure 5.11: *Continued*: Extrapolated spectra for the MAGN in the 3LAC sample. The colors indicate the cutoff energy: blue 10 GeV, red 50 GeV, yellow 100 GeV, green 500 GeV, light blue 1 TeV, magenta 10 TeV. The lines represent the differential sensitivity curve of the CTA, for different observing times, from 50 hours to 1000 hours. The source redshift and *Fermi* spectra index are reported in the top right corner of the figure.
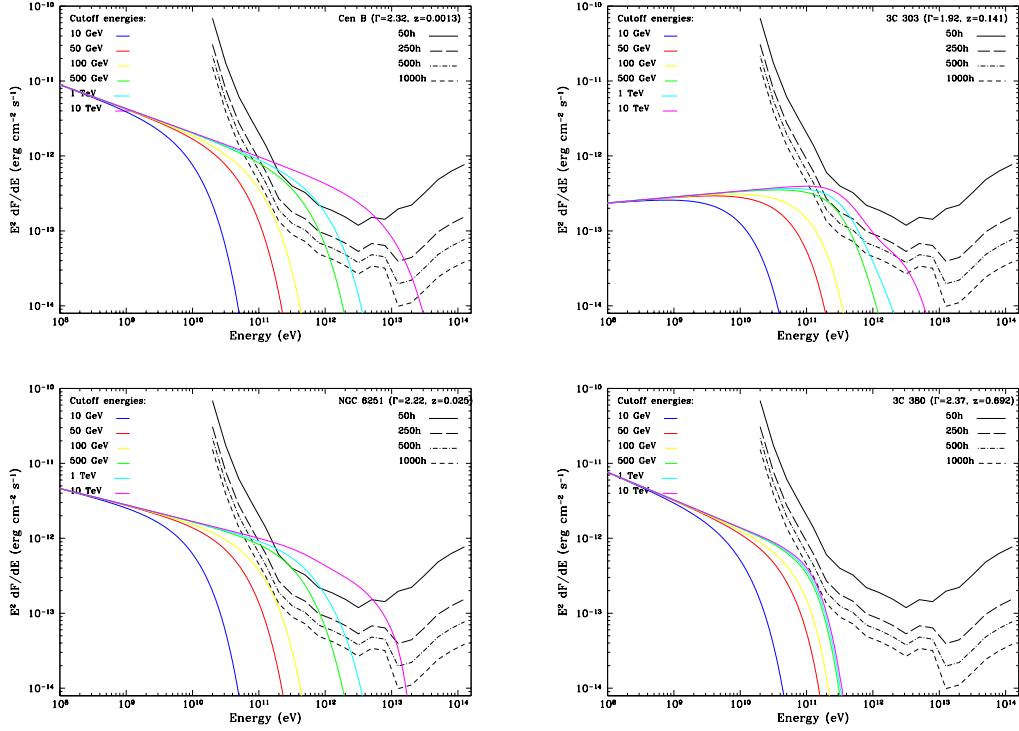
Chapter 6

Discussion

The aim of this thesis work is to evaluate the impact of the CTA on TeV studies of Misaligned AGN (MAGN), a class which includes mostly FR I and FR II radio galaxies and Steep Spectrum Radio Quasars (SSRQs).

VHE studies of these objects are critical in order to achieve a complete understanding of the radio-loud AGN population, the physical processes which produce the observed emission, and the particle composition of their relativistic jets. Moreover, since they are misaligned, MAGN allow us to observe both the accretion process and the relativistic jet, and so establish a connection between the two, with the goal of understanding the origin of radio-loudness in AGN.

As of today, only four MAGN are observed at TeV energies (NGC 1275, Cen A, M 87 and IC 310). The CTA, with its order-of-magnitude improvement in sensitivity and broad energy range, will be the ideal facility to improve our knowledge of this class of sources at VHE.

6.1 *Fermi* results

As a first step, we performed a detailed high-energy study of the four MAGN currently detected at VHE. We performed a spectral and temporal analysis of six years of *Fermi*-LAT data from these sources.

Our LAT data analysis benefits from improved integration time with respect to e.g. the 3LAC catalog (6 years vs 4 years), and a dedicated study for each source. The LAT spectra obtained and consistent with those published in the literature. Our data show better signal-to-noise ratio, because of the longer integration time. All sources are fitted with a power-law shape, except for NGC 1275, which is best fitted by a logparabola (see Section 4.2.1).

No significant variability was detected for Cen A, M 87 and IC 310. Since M 87 and IC 310 are variable in the TeV range, it is unclear whether the lack of

variability in the *Fermi* data is physical or is due to low statistics.

We have detected statistically significant variability for NGC 1275 on weekly time scales. Through simple causality arguments, we can use this variability to constrain the γ-ray emission region to have a size $R \leq c\Delta t\delta/(1 + z)$. Using $\Delta t = 1$ week, z=0.018, and assuming a Doppler factor $\delta = 2$ [19], we obtain the constrain $R < 0.012$pc $\sim 800 \, R_g$ where $R_g = GM_{BH}/c^2$ is the gravitational radius, assuming $M_{BH} \sim 3 \cdot 10^8 M_\odot$ [171] (see Section 4.2.2).

We compared it with the size of the torus and of the BLR. Technically, being an FR I radio galaxy, NGC 1275 may not have a BLR and/or a torus (see Section 1.4), therefore this comparison is made simply to have an idea of the order of magnitude of the size of the emission region with respect to the common "picture" of the AGN morphology. The distance of the BLR and the torus from the central engine is assumed to be a function of the accretion disk luminosity. The disk luminosity is roughly assumed to be $L_d \sim 3500 \, L_{\text{[OIII]}}$ [89]. For NGC 1275, assuming $L_{\text{[OIII]}} = 3.98 \cdot 10^{41}$ erg s^{-1} [47] we obtain $L_d = 1.39 \cdot 10^{45}$ erg s^{-1}. The resulting BLR size is [74] $R_{BLR} = 10^{17}L_{d,45}^{0.5}$ cm ~ 0.05 pc and the torus size is [74] $R_{torus} = 2 \cdot 10^{18}L_{d,45}^{0.5}$ cm ~ 0.9 pc, where $L_{d,45}$ is the disk luminosity in units of 10^{45} erg s^{-1}. Therefore, assuming that the size of the γ-ray emission region indicates its distance from the AGN central engine, in the case of NGC 1275 this region is located inside the BLR. This seems to suggest the radio core as the main dissipation region of the high-energy photons.

We have also detected statistically significant spectral variability for NGC 1275, using a bin size of 3 weeks. We also found a significant (chance probability $p \ll 10^{-3}$) negative correlation between flux and spectral index, with a correlation coefficient $r = -0.55$. This behavior is common among blazars, and is explained as due to the injection of fresh energetic particles in the jet during a flare, which causes a hardening of the particle energy distribution and, therefore, a flatter observed spectrum.

We then collected TeV data from the literature and constructed a comprehensive MeV-TeV spectrum for these MAGN (see Section 4.2.3). The HE-VHE connections is not trivial, mainly because the data are generally not contemporaneous, which is relevant since these sources are variable. Additionally, it is possible that the emission mechanisms that produce the observed radiation in these two bands are not the same (e.g. leptonic or hadronic processes), or there might be multiple emission regions with different spectra, as suggested by the MeV-TeV spectrum of the core of Cen A.

The most reliable HE-VHE spectrum we obtained is the one of NGC 1275, since we have contemporaneous *Fermi* and *MAGIC* data, with a total energy coverage spanning from 100 MeV up to ~ 1 TeV. The combined spectrum is best fitted by a power-law with spectral index $\Gamma = 2.05^{+0.08}_{-0.08}$ and an exponential cutoff

at $E_{cut} = 110^{+70}_{-40}$ GeV, with the high-energy peak of the SED occurring at ~ 30 MeV (see Fig. 5.3).

6.2 CTA predictions

In order to identify the best MAGN candidates for TeV detection with the CTA, we considered all the MAGN in the latest *Fermi*-LAT AGN catalog (3LAC). These 23 objects, plus the well-established γ-ray radio galaxy 3C 120, form our sample of candidate sources (see Table 5.2). It contains more than twice the sources of the previous catalog, based on the first 15 months of LAT data [5].

In order to estimate their detectability, we predicted the integrated flux that would be measured by the CTA for our candidate TeV MAGN, using the software package *ctools*. We simulated 50 hours of CTA observations for our sources, assuming a power-law shape as an input model. The spectral parameters were taken from the 3LAC catalog. This approach implicitly assumes that the *Fermi* spectrum of each MAGN does not suffer further steepening in the CTA band.

We performed a standard likelihood analysis on the resulting event file, and computed the integrated flux in the CTA energy range (taking into account the absorption of TeV photons by the EBL) using the resulting spectral parameters and errors. Our analysis predicts the detection with $TS > 25$ of all local ($z < 0.1$) FR I sources in the sample, including 9 new detections. The best candidates are flat-spectrum and/or very nearby sources, like PKS 0625-35 (see Table 5.3). Our study clearly indicates that these two parameters (Γ and z) are the most important ones in order to identify a promising TeV MAGN candidate.

Since the assumption of a smooth extrapolation of the LAT spectrum up to the highest CTA energy range is quite optimistic, we tested a more realistic scenario by assuming an exponential cutoff at 100 GeV, such as the one observed for NGC 1275 (see Section 4.2.3). In this case, we have one new detection with $TS > 25$, namely PKS 0625-35, and two borderline candidates with $TS \sim 11$ (Cen B) and $TS \sim 9$ (NGC 6251) (see Table 5.4).

However, it should be noted that that TeV variability has been observed in MAGN, namely M 87 and IC 310, with current Cherenkov telescopes, with flux variation of a factor up to 5-10 (see Section 4.2.2). If our candidate TeV MAGN are variable at these energies, the number of detectable sources would increase. Indeed sources that we predict to be close to the detection threshold (e.g. 3C 78, NGC 6251, Cen B) should be observable in flaring state. This is even more favored by the hardening of the jet emission spectrum which is generally observed in radio-loud AGN during high-flux states (e.g. NGC 1275, discussed above, or IC 310 [23]) since a hard spectrum is one of the vital requirements for a good TeV candidate.

In addition to possibly discovering new TeV MAGN, the CTA will certainly provide much better data for the ones already detected. To quantify this, we performed the same predictive analysis described above on the four TeV MAGN, using the observed TeV spectral parameters as an input instead of the LAT ones.

The TS for these objects is greatly improved with respect to the data from the current IACTs, of a factor ranging from ~ 11 to ~ 240 (see Section 5.2.2 and Fig. 5.7).

So far, we have only discussed the prospects for integrated flux detections with the CTA. As a further step, we have attempted to predict whether it will also be possible to obtain VHE spectra of our candidate MAGN with the CTA, considering integration times larger than the standard 50 hours (250, 500 and 1000 hours). To do this, we assumed as template of MAGN emission in the MeV-TeV range a power-law with exponential cutoff, considering different cutoff energies. We then compared the resulting extrapolated spectra with preliminary CTA differential sensitivity curves, for different observing times (see Figg. 5.9 5.10 and 5.9 in Section 5.3).

Our results indicate that spectral analysis with the CTA is difficult for most of our MAGN candidates, being generally faint, steep-spectrum sources. Additionally, EBL absorption is critical above 1 TeV for our most distant sources ($z > 0.1$). The most promising objects are those identified by our previous analysis, i.e. flat-spectrum and/or very nearby sources. With the exception of the brightest ones, 50 hours are not enough to acquire good quality spectra. However 250 hours of exposure should be sufficient to obtain a good signal-to-noise ratio spectrum of PKS 0625-35 even if the power law cuts off at 100 GeV. If the power law extends up to 500 GeV, a spectral study could be carried out for other 4 sources.

It is useful to compare our results with the current plans for extragalactic observations with the CTA. Prospects for a blazar survey with the CTA have been discussed by Inoue et al. 2010 [91] and Dubus et al. 2013 [58]. Current plans involve a CTA extragalactic blind-eye (i.e. not targeted) survey covering a quarter of the sky ($\sim 10^4$ square degrees) in about 1000 hours. Such a survey would be a great advance in extragalactic VHE astronomy, since it would provide an unbiased population of sources such as to allow the determination of an AGN γ-ray luminosity function (which is still lacking), it would open the possibility of discovering extreme sources peaking beyond 100 GeV, which would therefore be missed by *Fermi*-LAT, and it would allow serendipitous discoveries of flaring sources. The first point in particular is very important, since the current TeV catalogs are biased, because TeV observations are usually target-of-opportunity (ToO) observations triggered by flux changes at other wavelengths, and therefore are not ideal for complete population studies. According to Padovani & Giommi

2015 [133], a survey as the one described above will be able to detect 100-180 blazars. Dubus et al. 2013 discussed a survey of 250 hours with the same coverage, predicting a total of 20 blazar detections.

In light of this, we asked ourselves what would be the best observing strategy with the CTA in order to maximize the possibility of detecting new TeV MAGN, and the quality of the corresponding data.

The recent study by Padovani & Giommi 2015 presented predictions on blazar detections with the CTA, as the final part of a study aimed at reproducing the multi-wavelength properties of the whole jetted AGN population within a simplified framework (see Giommi et al. 2012 [79] and Giommi et al. 2013 [80] for the details of this model). Although this study was mainly focused on blazars, through the radio-loud unified models it provided as a byproduct some detection predictions for radio galaxies with the CTA. These sources would be misclassified radio galaxies, i.e. real blazars, with jets oriented close to our line-of-sight, whose non-thermal emission is not strong enough to swamp the light from the host galaxy.

As a spectral shape in the TeV range, the authors, starting from the GeV γ-ray spectral shape, considered the cases of a break in the spectrum of $\Delta\Gamma = 0.5$ at 200 GeV (hard spectrum), or a break of $\Delta\Gamma = 1$ at 100 GeV (soft spectrum). The spectral shape is therefore assumed qualitatively, as has been done in our own work. The detection predictions were made assuming a large area shallow survey (sensitivity $S(> 100 \text{ GeV}) = 2 \cdot 10^{-12}$ photons cm^{-2} s^{-1}, coverage of 10^4 square degrees) and a smaller area, deeper survey (sensitivity $S(> 100 \text{ GeV}) = 1.25 \cdot 10^{-12}$ photons cm^{-2} s^{-1}, coverage of 2500 square degrees). The predicted number of radio galaxies that will be detected, corrected for EBL absorption, is given in Table 6.1, and it ranges from 2.3 to 6.2. Since we already have 4 TeV detected radio galaxies, this model then predicts at best $\sim$2 new detections, in the case of a lower-energy spectral break and a large area survey. The fact that the larger area survey gives the best results is to be expected since, with respect to the alternative survey, it has 4 times the coverage with just 1.6 times lower sensitivity.

Compared to ours, these results are more in accordance (as order of magnitude) with the cutoff power-law model. It must be noted that the two analyses are significantly different, both in scope and in methods. Padovani & Giommi 2015 use the term "radio galaxy" to indicate sources with aligned or moderately aligned jets, which represent only a fraction of all MAGN (i.e. IC 310). Moreover, besides the differences in the assumptions regarding the spectral shape, our study is based on simulated CTA data with a standard effective observing time per source, rather than on a simulated survey.

In order to properly compare our results with these studies, we need to calcu-

Table 6.1: Predicted number of radio galaxies detected with the CTA for two different spectra and two different surveys, from Padovani & Giommi 2015 [133].

Survey	*Spectrum*	
	Soft spectrum	**Hard spectrum**
Large area	3.2	6.2
Deep	2.3	4.4

late the effective observing time for each source observed in the simulated survey, considering that our analysis involves at least 50 hours of observing time.

The time spent observing a single FoV during a survey is given by [91] $t_{FoV} = t_{survey}(A_{FoV}/A_{survey})$. Assuming $t_{survey} = 1000$ h, and considering the CTA FoV at 1 TeV $\theta_{FoV} = 8°$ (see Table 2.4), we have (as an order of magnitude) $A_{FoV} \sim \theta_{FoV}^2$ and so we obtain 6.4 h per FoV. We can see that these observing times are significantly smaller than the ones adopted in our study. In order to reach 50 h per FoV, considering a blind sky (e.g. not a targeted) survey one would need $t_{survey} \sim 8000$ h for a coverage of 10000 square degrees.

Since MAGN are generally weak sources, the relatively short exposure time per source implied by a blind-sky survey is not ideal for the detection of new sources of this class, except for extreme sources (e.g. IC 310). As shown by our results, in order to detect a significant number of new MAGN it is necessary to have at least 50 hours of exposure for each source (as an order of magnitude). Therefore, a targeted survey would be more suited to this kind of studies. Dubus et al. 2013 [58] discussed a targeted survey of *Fermi*-LAT sources with the CTA. With exposure times per pointing of ~ 50 hours, they predict the detection of ≥ 170 extragalactic sources. In this case the area covered would be much smaller (0.5-1% of the sky), but with much better sensitivity. Of course this observing strategy would imply a smaller probability of detecting extreme sources missed by *Fermi*, although serendipitous discoveries of these sources in the FoV of the targeted sources would still be possible (i.e. IC 310 in the FoV of NGC 1275).

The requirement for long targeted observations is even more pressing if one wishes to obtain a TeV spectrum of new MAGN with the CTA, since this would imply an observing time per source larger than 250 hours.

Conclusions

The aim of this thesis work is to evaluate the impact of the next generation *Cherenkov Telescope Array* (CTA) on TeV studies of Misaligned Active Galactic Nuclei (MAGN), a new elusive but fascinating class of extragalactic high-energy (HE) and very high-energy (VHE) emitters. Today, this class includes only 24 sources detected at GeV energies by *Fermi* (out of more than 3000 objects detected in total) and 4 sources detected in the TeV band by Cherenkov telescopes (out of about 60 objects in the TevCat online catalog).

In this study, we first performed a detailed analysis of six years of *Fermi* data on these last four sources, namely NGC 1275, Centaurus A, M 87 and IC 310. We then collected VHE data from the literature for these objects, and constructed a high-energy SED from 100 MeV up to the TeV range. Based on the observed properties of these sources, we investigated the CTA detection prospects for all the MAGN detected by *Fermi*, both for integrated flux analysis and spectral analysis.

The main results of our work can be summarized as follows:

- Our *Fermi* data analysis resulted in the detection of **flux variability** for NGC 1275 on time scales of 1 week, and of **spectral variability** of time scales of 3 weeks. In the latter case, there is a significant **anti-correlation between flux and spectral index**, a feature commonly observed in blazars, but established here for the first time for a γ-ray MAGN.

- **The HE-VHE connection in MAGN is complex**, with only NGC 1275 which benefits from contemporaneous *Fermi* and TeV data. The high-energy spectrum for this source is best fitted by a power-law with a steep exponential cutoff, in agreement with the fact that the high-energy peak of the SED lies in the *Fermi* band at ~ 30 MeV. The high-energy spectra of Cen A and M 87 also suggest a SED peak in the *Fermi* band or at smaller energies, while the peculiar source IC 310 shows an unusually flat high-energy spectrum, with no hints of a falling trend up to $\sim$10 TeV.

- We predict the integrated flux detection, with 50 hours of CTA observations, of **9 new MAGN** at the 5σ significance level, under the assumption of a

straight extrapolation of the *Fermi* power-law in the CTA energy range. Assuming an exponential cutoff at 100 GeV as a more realistic shape, we still predict one 5σ and two $\sim 3\sigma$ detections. Overall, our results indicate that **the CTA will be able to detect at least 2-3 new MAGN**.

- We predict that it will be possible to obtain a **TeV spectrum with the CTA for 5 new MAGN**, with at least 250 hours of observation, if their spectrum cuts off at energies $E \leq 500$ GeV.

- Based on our results, the current plans for a blind-sky extragalactic survey with the CTA imply significant less observing time per source than what would be needed to detect new MAGN or obtain spectra for these sources. The **best observing strategy** to achieve this goal would be to schedule **long targeted observations** of the most promising TeV MAGN candidates (e.g. PKS 0625-35, Centaurus B, NGC 6251, 3C 78), with observing times of at least 50 hours for an integrated flux detection, and 250 hours for spectral analysis.

This was the first systematic study investigating TeV MAGN as a class. With these results, we now have a better understanding of what are the prospects for CTA studies of MAGN, and which observing strategy would be best suited to achieve them.

As for the future prospects of this line of work, there is a scientific paper in preparation which reports the results of our predictive study for MAGN with the CTA. We plan to better quantify our predictions and produce a table through which the scientific community can estimate the prospects for CTA studies of a candidate source, based on its observed properties.

Additionally, we plan a second paper, more oriented towards physical interpretation, reporting the detailed *Fermi* variability study of NGC 1275, the brightest MAGN in the GeV band.

Bibliography

[1] M.G. Aartsen et al. (IceCube collaboration) 2013, PhRvL, 111, 1103

[2] A.A. Abdo et al. (*FERMI* collaboration) 2009, ApJ, 699, 31

[3] A.A. Abdo et al. (*FERMI* collaboration) 2009, A&A, 544, A96

[4] A.A. Abdo et al. (*FERMI* collaboration) 2010, ApJ, 719, 1433

[5] A.A. Abdo et al. (*FERMI* collaboration) 2010, ApJ, 720, 912

[6] A.A. Abdo et al. (*FERMI* collaboration) 2010, ApJ, 710, 1271

[7] A. Abramowski et al. 2012, ApJ, 746, 151

[8] V.A. Acciari et al. 2009, *Science*, 325, 444

[9] F. Acero et al. (*FERMI* collaboration) 2015, arXiv:1501.02003

[10] B.S. Acharya et al. (*CTA* consortium) 2013, Astroparticle Physics, 43, 3

[11] M. Ackermann et al. (*FERMI* collaboration) 2015, arXiv:1501.06054

[12] M. Ackermann et al. (*FERMI* collaboration) 2013, ApJ, 209, 34

[13] F. Aharonian et al. (*H.E.S.S.* collaboration) 2006, *Science*, 314, 1424A

[14] F. Aharonian et al. (*H.E.S.S.* collaboration) 2009, ApJ, 695, 40L

[15] F. Aharonian et al. (*H.E.S.S.* collaboration) 2007, ApJ, 664, 71

[16] M. Ajello et al. 2009, ApJ, 690, 367

[17] J. Albert et al. 2007, ApJ, 669, 862

[18] J. Aleksić et al. (*MAGIC* collaboration) 2012, A&A, 539, A2

[19] J. Aleksić et al. (*MAGIC* collaboration) 2014, A&A, 564, A5

[20] J. Aleksić et al. (*MAGIC* collaboration) 2010, ApJ, 723L, 207A

[21] J. Aleksić et al. (*MAGIC* collaboration) 2014, *Science*, 346, 1080A

[22] J. Aleksić et al. (*MAGIC* collaboration) 2012, A&A, 544, 96

[23] J. Aleksić et al. (*MAGIC* collaboration) 2014, A&A, 563, 91

[24] E. Aliu et al. (*VERITAS* collaboration) 2012, ApJ, 746, 141

[25] R.R.J. Antonucci 1993, ARA&A, 31, 473

[26] R.R.J. Antonucci 2011, arXiv:1101.0837

[27] R.R.J. Antonucci 1984, ApJ, 278, 299

[28] R.R.J. Antonucci & J.S. Miller 1985, ApJ, 297, 621

[29] R.R.J. Antonucci & J.S. Ulvestad 1985, ApJ,294,158A

[30] K. Asada et al. 2006, Publ. Astron. Soc. Japan 58, 261

[31] W.B. Atwood et al. 2009, ApJ, 697, 1071A

[32] J.M. Bai & M.G. Lee 2001, ApJ, 549L, 173B

[33] J.M. Bai & M.G. Lee 2001, ApJ, 548, 244B

[34] B. Balmaverde et al. 2006, A&A, 451, 35

[35] R.D. Baldi et al. 2013, A&A, 560A, 81B

[36] W.H. Baumgartner et al. 2013, ApJS, 207, 19

[37] V. Beckmann & C.R. Shrader 2012, *Active Galactic Nuclei*, 380 pages, Wiley-VCH

[38] K. Behrouz et al. 2015, arXiv:1504.07592

[39] M. Beilicke et al. 2012, AIPC, 1505, 586

[40] P.D. Best et al. 2012, MNRAS, 421, 1569B

[41] G.F. Bignami et al. 1975, Space Sci. Instr., 1, 245

[42] J.A. Biretta et al. 1995, ApJ, 447, 582B

[43] R.D. Blandford & M.J. Rees 1978, PhyS, 17, 265B

[44] M. Böttcher et al. 2013, ApJ, 768, 54

[45] A.M. Brown & J. Adams 2011, MNRAS, 413, 2785

[46] J.O. Burns et al. 1983, ApJ, 273, 128

[47] S. Buttiglione et al. 2010, A&A, 509, A6

[48] A. Caulet et al. 1992, ApJ, 388, 301

[49] M. Cerruti et al. 2015, MNRAS, 448, 910

[50] M. Chiaberge et al. 2002, A&A, 394, 791C

[51] M. Chiaberge et al. 2000, A&A, 358, 104

[52] M. Chiaberge et al. 1999, A&A, 349, 77

[53] E.L. Chupp et al. 1972, Nature, 241, 333-335

[54] C.J. Conselice, J.S. Gallagher R.F.G. Wyse 2001, AJ, 122, 2281

[55] J. Cortina et al. 2009, Proceedings of the 31st ICRC, Łódź

[56] S.S. Doeleman et al. 2012, *Science*, 338, 355

[57] A. Dominguez et al. 2011, MNRAS, 410, 2556

[58] G. Dubus et al. 2013, Astroparticle Physics, 43, 317

[59] J.S. Dunlop et al. 1993, MNRAS, 264, 455D

[60] J.S. Dunlop & J.A. Peacock 1990, MNRAS, 247, 19D

[61] M. Elitzur & I. Shlosman 2006, ApJ, 648L, 101E

[62] D.A. Evans et al. 2004, ApJ, 612, 786

[63] A.C. Fabian et al. 2011, MNRAS, 418, 2154

[64] B.L Fanaroff & J.M. Riley 1974, MNRAS, 167, 31P

[65] L. Ferrarese & D. Merrit 2000, ApJ, 539L, 9F

[66] C.E. Fichtel, R.C. Hartman, D.A. Kniffen, D.J. Thompson G.F. Bignami 1975, ApJ, 198, 163F

[67] D.J.E. Floyd et al. 2004, MNRAS, 355, 196F

[68] N. Fraija 2014, MNRAS, 441, 1209

[69] S.T. Garrington et al. 1988, *Nature*, 331, 147G

[70] M. Georganopoulos & D. Kazanas 2003, ApJ, 589, L5

[71] G. Ghisellini & A. Celotti 2001, A&A, 379L, 1G

[72] G. Ghisellini et al. 2005, A&A, 432, 401

[73] G. Ghisellini 2013, LNP, 873, G

[74] G. Ghisellini & F. Tavecchio 2015, MNRAS, 448, 1060

[75] G. Ghisellini et al. 2014, *Nature*, 515, 376

[76] D. Giannios et al. 2010, MNRAS, 402, 1649G

[77] M. Gierlinski & C. Done 2004, MNRAS, 349L, 7G

[78] P. Giommi et al. 2012, A&A, 541, A160

[79] P. Giommi et al. 2012, MNRAS, 420, 2899

[80] P. Giommi et al. 2013, MNRAS, 431, 1914

[81] P. Grandi & E. Torresi 2011, Proceedings of *Fermi & Jansky: Our Evolving Understanding of AGN*, St. Michaels, MD, Nov. 10-12, 2011, edited by R. Ojha, D. Thompson and C. Dermer, eConf C1111101

[82] P. Grandi et al. 2013, EPJWC, 61, 04007

[83] P. Grandi et al. 2012, ApJ, 751, L3

[84] P. Grandi & G. Palumbo 2007, ApJ, 659, 235G

[85] F. Haardt & L. Maraschi 1993, ApJ, 413, 507H

[86] K. Hada et al. 2012, ApJ, 760, 52

[87] M.J. Hardcastle & D.M. Worrall 1999, MNRAS, 309, 969

[88] B.A. Harmon et al. 2004, ApJS, 154, 585

[89] T.M. Heckman et al. 2004, ApJ, 613, 109

[90] R. Hes et al. 1993, *Nature*, 362, 326H

[91] Y. Inoue et al. 2010, PASJ, 62, 1005

[92] C.A. Jackson & J.V. Wall 1999, MNRAS, 304,160J

[93] N. Jackson & S. Rawlings 1997, MNRAS, 186, 241J

[94] R.M. Johnstone & A.C. Fabian 1995, MNRAS, 273, 625

[95] W. Junor et al. 1999, *Nature*, 401, 891

[96] M. Kadler et al. 2012, A&A, 538L, 1K

[97] J. Kataoka et al. 2010, ApJ, 715, 554

[98] K.I. Kellerman et al. 1989, AJ, 98, 1195

[99] K. Kotera & A.V. Olinto 2011, ARA&A, 49, 119

[100] W. Kraushaar et al. 1965, ApJ, 141, 845K

[101] W. Kraushaar et al. 1972, Apj, 177, 341K

[102] M.J. Kukula et al. 2002, NewAR, 46, 171K

[103] R.A. Laing 1988, *Nature*, 331, 149L

[104] R.A. Laing et al. 1994, ASPC, 54, 201L

[105] A. Lawrence & M. Elvis 1982, ApJ, 256, 410

[106] J.-P. Lenain et al. 2008, A&A, 478, 111L

[107] A. Levinson & F. Rieger 2011, ApJ, 730, 123L

[108] H. Lietzen et al. 2011, A&A, 535A, 21L

[109] M.L. Lister & D.C. Homan 2005, AJ, 130, 1389

[110] C.R. Lynds 1970, ApJ, 159, L151

[111] H.L. Marshall et al. 2002, ApJ, 564, 683M

[112] A.P. Marscher 1988, ApJ, 334, 552

[113] J. Magorrian et al. 1998, AJ, 115, 2285M

[114] F. Massaro et al. 2013, ApJS, 208, 15M

[115] J.R. Mattox et al. 1996, ApJ, 461, 396M

[116] N.J. McConnell et al. 2011, *Nature*, 480, 215M

[117] C. Meegan et al. 2009, ApJ, 702,791M

[118] G.K. Miley 1973, A&A, 26, 413M

[119] R. Minkowski 1957, IAU symp.4, Radio Astronomy, ed. H.C. van de Hulst (Cambridge: Cambridge Univ. Press), 107

[120] B. Mingo et al. 2014, MNRAS, 440, 269M

[121] H. Nagai et al. 2014, ApJ, 785, 53N

[122] R. Narayan et al. 1995, ApJ, 452, 710N

[123] A. Neronov 2010, A&A, 519, L6

[124] A. Neronov & F.A. Aharonian 2007, ApJ, 671, 85N

[125] P.L. Nolan et al. (*Fermi* collaboration) 2021, ApJS, 199, 31N

[126] C.P. O'Dea 1998, PASP, 110, 493

[127] M.J.L. Orr & I.W.A. Browne 1982, MNRAS, 200, 1067O

[128] F.N. Owen 1993, in *Jets in Extragalactic Radio Sources*, Springer-Verlag, 1993, 273

[129] F.N. Owen & M.J. Ledlow 1994, ASPC, 54, 319O

[130] F.N. Owen et al. 2000, ApJ, 543, 611O

[131] P. Padovani 1992, A&A, 256, 399P

[132] P. Padovani & E. Resconi 2014, MNRAS, 443, 474

[133] P. Padovani & P. Giommi 2015, MNRAS, 446, 41

[134] A. Pedlar et al. 1990, MNRAS, 246, 477

[135] Pierre Auger Collaboration 2008, *Science*, 318, 938

[136] T.A. Rector et al. 1999, ApJ, 516, 145R

[137] O. Reimer et al. 2003, ApJ, 588, 155

[138] F.M. Rieger & F.A. Aharonian 2008, A&A, 479L, 5R

[139] E.E. Rigby et al. 2011, MNRAS, 416, 1900R

[140] M. Rowan-Robinson 1977, ApJ, 213, 635R

[141] G.B. Rybicki & A.P. Lightman 1986, *Radiative processes in astrophysics*, Wiley-VCH Verlag GmbH, Weinheim, ISBN 0-471-82759-2

[142] C.L. Sarazin 1988, *X-ray emission from clusters of galaxies* (C.U.P)

[143] K. Sato et al. 2005, PASJ, 57, 743S

[144] R.D. Saxton et al. 1993, MNRAS, 262, 63S

[145] M. Schmidt 1963, *Nature*, 197, 1040S

[146] J.L. Schmitt 1968, *Nature*, 218, 663S

[147] M. Schmidt & R.F. Green, ApJ, 269, 352

[148] J. Scharwächter et al. 2013, MNRAS, 429, 2315S

[149] C.K. Seyfert 1943, ApJ, 97, 28

[150] N.I Shakura & R.A. Sunyaev 1973, A&A, 24, 337

[151] D. Sijbring & A.G. de Bruyn 1998, A&A, 331, 901S

[152] H. Sol et al. 2013, Astroparticle Physics, 43, 215

[153] W.B. Sparks et al. 1996, ApJ, 473, 254S

[154] P. Sreekumar et al. 1999, APh, 11, 221S

[155] W.A. Stein et al. 1976, ARA&A, 14, 173S

[156] A.W. Strong & G.F. Bignami 1983, ApJ, 274, 549S

[157] P.A. Strittmatter et al. 1972, ApJ, 175L, 7S

[158] C. Tadhunter 2008, NewAR, 52, 227T

[159] C. Tadhunter & Z. Tsvetanov 1989, *Nature*, 341, 422T

[160] Y.T. Tanaka et al. 2015, ApJ, 799, 18

[161] F. Tavecchio & G. Ghisellini 2014, MNRAS, 443, 1224

[162] F. Tavecchio & G. Ghisellini 2008, MNRAS, 385L, 98T

[163] A. Tchekhovskoy et al. 2011, MNRAS, 418, 79

[164] Y. Terashima & A.S. Wilson 2003, ApJ, 583, 145T

[165] D.J. Thompson et al. 1993, ApJS, 86, 629

[166] F. Tombesi et al. 2013, MNRAS, 430, 1102T

[167] E. Torresi 2011, Proceedings of *Fermi & Jansky: Our Evolving Under-standing of AGN*, St. Michaels, MD, Nov. 10-12, 2011, edited by R. Ojha, D. Thompson and C. Dermer, eConf C1111101

[168] C.M. Urry, P. Padovani, 1995, PASP, 107, 803

[169] R.V. Vasudevan et al. 2014, ApJ, 785, 30V

[170] R.C. Walker, J.D. Romney & J.M. Benson 1994, ApJ, 430, L45

[171] J.H. Woo & C.M. Urry 2002, ApJ, 579, 530

[172] M. Zamaninasab et al. 2014, *Nature*, 510, 126

Ringraziamenti

É arrivata finalmente, dopo un lungo anno di tesi, la conclusione di un altra tappa! E anche questa volta ci sono tante persone da ringraziare, senza le quali non sarei arrivato a questo punto, né con queste prospettive future.

Prima di tutto voglio ringraziare i miei relatori di tesi. Il Prof. Cristian Vignali, per essersi sempre interessato tanto al mio lavoro, per il tempo che vi ha dedicato e per l'importantissimo aiuto nel programmare le mie scelte future. La Dott.ssa Eleonora Torresi, per avermi aiutato soprattutto nella prima parte del lavoro di tesi.

E soprattutto la Dott.ssa Paola Grandi, per il tantissimo tempo speso in spiegazioni, aiuti e discussioni, per avermi lasciato risolvere i problemi da solo quando era solo questione di pigrizia (e quella di certo non è mancata!), ma senza mai lasciarmi bloccato su un problema, per avermi sempre incoraggiato nonostante il mio carattere schivo, per aver corretto la tesi in modo meticoloso e approfondito, insieme al Prof. Vignali e alla Dott.ssa Torresi, e infine anche in questo caso per l'indispensabile sostegno e consiglio nel decidere il mio futuro.

Sono certo che le mie prospettive in questo momento non sarebbero le stesse se non avessi scelto questi relatori. Non avrei davvero potuto chiedere di meglio!

Un grazie va anche a tutto l'ambiente dell'IASF, con cui ho condiviso un anno di lavoro. Un ambiente alla mano fatto di brave persone, in cui ho imparato tante cose su cosa significa fare questo lavoro. Vorrei inoltre ringraziare la Dott.ssa Valentina Fioretti per l'aiuto nell'installazione di componenti *software* molto importanti per il mio lavoro.

Vorrei ringraziare anche gli amici con cui ho condiviso questi anni di magistrale. È stata una fortuna trovare, in un contesto completamente nuovo, un gruppo di persone con cui mi sono sempre divertito, e ho condiviso bei momenti, dalle lezioni ai giorni a Loiano, oltre a tante altre occasioni.

Un pensiero e un abbraccio particolare vanno ai miei compagni di laboratorio, Lella e Davide, con cui tramite la condivisione di quella traumatica esperienza (e

tante altre più belle, per fortuna!) ho legato tanto.

Grazie infine alla mia famiglia, ai miei genitori che per altri tre anni mi hanno sostenuto nelle mie scelte e negli studi che mi hanno portato a questo traguardo, dandomi la possibilità di puntare ai prossimi. Grazie a mia sorella, e a tutti gli zii/e, cugini/e e ai nonni, che danno un senso più ampio e profondo all'idea di "casa".

Infine, grazie a Claudia, per essere sempre il mio sostegno più grande in tutte le circostanze e le scelte, dalle più quotidiane alle più importanti.

Grazie a tutti!